CRITICAL CURRENTS AND DISSIPATION OF GRAIN BOUNDARY NETWORKS IN COATED CONDUCTORS

PROGRAMA DE DOCTORAT EN CIÈNCIA DE MATERIALS
Departament de Física de la Universitat Autònoma de Barcelona

PER:
ANNA PALAU MASOLIVER

Departament de Materials Magnètics i Superconductors
ICMAB-CSIC

DIRECTORA: **Dra. Teresa Puig**

TUTOR: **Prof. Jordi Pascual**

Bellaterra, 24 Gener 2005

ACKNOWLEDGMENTS

First of all a very special acknowledgment to Dra. Teresa Puig, supervisor of this Thesis, thanks for all the opportunities you have given to me, for your confidence, your helpful advises, your support in the most difficult moments and of course for all the time you have dedicated to this work.

To Prof. X. Obradors, thanks for bring me the opportunity to work in your group, for your help, your advices and for showing so much interest in the topic I was working in.

To Dr. R. Feenstra and Dr. J Thompson, for the nice time I spent in Oak Ridge National Laboratory, for their help and the exceptional welcome they gave us. I also want to thank Dr. R. Feenstra for the great amount of samples he provided me.

To Prof. H. Freyhard, Dr. C. Jooss, and C. Guth, for all the facilities and advices they gave me during my stay in the "Zentrum für FunktionWekstoffe" and for the samples they provided me.

To Dr. B. Holzapfel, and L. Fernández, for all the time they dedicated me when I was in the "IFW of Dresden" and also for the samples they provided me.

To Dr. A. Sánchez, Dr. E. Pardo, Dr. C. Navau and Dr. D.X. Chen, for the fruitful discussions we have maintained during the development of this Thesis

To Prof. Franciso De la Cruz for the useful and clear ideas proposed in order to understand the most difficult issues.

To Dr. M. Feldmann, Dr. D. Larbarestier, Dr. A. Gurevich for the nice meeting we had in Wisconsin.

To “Ministerio de Educación y Ciencia” for financial support

To all the colleagues and friends of my group, which have helped me in many cases during all this time. Especially to M. Coll, J. Gutierez and J. Gázquez for the data they have provided me and to M. Gibert for her help in the most difficult moments.

Al Josep Massana, per fer possible la impressió d’aquesta Tesi.

A l’Andrea, al Joffre, al Jordi, a la Judit i a la Mariona, per les profitoses discussions mantingudes al barri de les Corts.

No pot faltar un agraïment molt especial a la meva família. Als meus pares, perquè sempre m’heu fet costat i m’heu ajudat. Al Josep, a la Montse, a la Judit i al Dani per tot el suport que m’heu donat i perquè sempre m’heu animat a seguir endavant. I molt especialment a la Laura, perquè amb la seva alegria m’ha donat forces per seguir treballant en els moments més difícils.

A l’Aleix, que ha hagut de patir el mal humor dels moments més crítics, perquè la teva ajuda ha estat molt important.

A tots, MOLTES GRÀCIES !!

MOTIVATION

High-temperature superconducting (HTS) tapes have emerged as promising materials for superconducting power applications since they make possible electric power equipment that is half the size of conventional alternatives, with half energy losses, increasing the efficiency in the generation, transmission and distribution of the electric energy, and thus reducing the impact of power delivery on the environment. However, unlike typical conductors, oxide based superconductor materials are brittle and easily damaged and thus they are difficult to process and handle, specially forming large and flexible wires.

Up to now it has been possible to produce kilometre lengths of the first generation of HTS wires, based on bismuth material, for use in electrical transmission cables. However, due to poor performance in strong magnetic fields, use of this type of HTS wire for motors, transformers, and generator coils is limited to relatively low temperatures. The second generation of HTS-coated conductors, based on YBCO, is much less affected by strong magnetic fields, thus are being intensely developed by government, industry and university research laboratories around the world.

YBCO coated conductors can support critical current densities, J_c, exceeding 2.10^{10} A/m^2 (77 K, self field) on biaxially aligned substrates with an appropriate lattice match. Two methods to provide such templates for the epitaxial growth of the superconductor have dominated research in the field of second generation HTS wires. The first method uses a polycrystalline metal substrate along with a technique to induce texture in a buffer layer such as ion-beam assisted deposition (IBAD) has to be implemented. The second method begins with a textured metal substrate which is buffered with an epitaxial film for diffusion resistance and chemical compatibility with the superconductor. The rolling method used to achieve a biaxially textured substrate is called RABiTS. Numerous methods are available for epitaxial deposition of YBCO, including vacuum techniques and cheaper non vacuum processes.

Although coated conductors with a high biaxially texture can be fabricated, this materials are granular on a microscopic scale. Hence, due to its granular microstructure and the strong dependence of critical current density, J_c, on grain misorientations, the transport current in these conductors flows in a percolative way through the network of grain boundaries. The physical mechanisms governing the carrying current capability and possible ways to improve the current transfer are under intense investigation. In this contribution, we have analyzed the inductive response of coated conductors by means of dc-magnetometry and ac-susceptibility and we have focused on the understanding of the granular behaviour of these materials. The peculiar features of the hysteresis loops and ac-susceptibility response associated to the presence of grain boundaries manifest the richness of these two inductive methodologies for the analysis of YBCO coated conductors.

A number of IBAD and RABiTS coated conductors from different laboratories have been analyzed and the grain and grain boundary critical current densities have been determined in the framework of the critical state model. The analysis presented enable to study the interaction between both critical current densities and thus establish the principal limitations for the percolative critical current through the material. Additionally, we have studied the different vortex motion regimes appearing in a H-T diagram for a coated conductor by analyzing the dependence of the critical current density and the activation energy with the applied magnetic field. This has allowed us to infer the different pinning mechanisms that govern vortex motion in coated conductors and establish experimental evidence for Abrikosov vortex interaction with Abrikosov-Josephson vortices associated to the grain boundaries

.

CHAPTER 1

INTRODUCTION

1.1 THE PHENOMENON OF SUPERCONDUCTIVITY

The principal property of superconductors is that, these materials lose their electric resistance on cooling then below a transition temperature, T_c, called the critical temperature. The first successful description of superconductors was proposed by Gorter and Casimir in the 1930s who considered a two fluid model for describing the transition between the normal and the superconducting state. According to this model, a superconductor behaves a thought it contains electrons of two different types, normal electrons, which behaves at least approximately like electrons in normal metals, and the superelectrons, which have striking and unusual properties. Both types of electron can carry current, the normal electrons with resistance and the superelectrons without resistance. As we pass below the critical temperature, T_c, the density of superfluid is supposed to rise from zero, while the density of normal fluid falls [1].

The simple two fluid description survives to some extent in the modern microscopic theory proposed by J.Barden, L. Cooper, and J.R. Schrieffer in 1957 [1,2]. This theory is based on the idea that, below the critical temperature, the electrical carriers in the material bound together forming Copper pairs, in the presence of a weak attractive interaction mediated by the lattice (electron-phonon-electron interaction). The Copper pairs are energetically coupled together, so that each pair is in exactly the same state. This is possible because in each pair, two fermions constitutes a boson, and all the pairs undergone a Bose condensation. It is the formation of the pairs which gives the system its superfluid properties since their movement is coherent and does not dissipates energy. The wavefunction that describes all the Copper pairs, ..(r), changes in a distance given by the coherence length, •(T) (see Fig. 1-1).

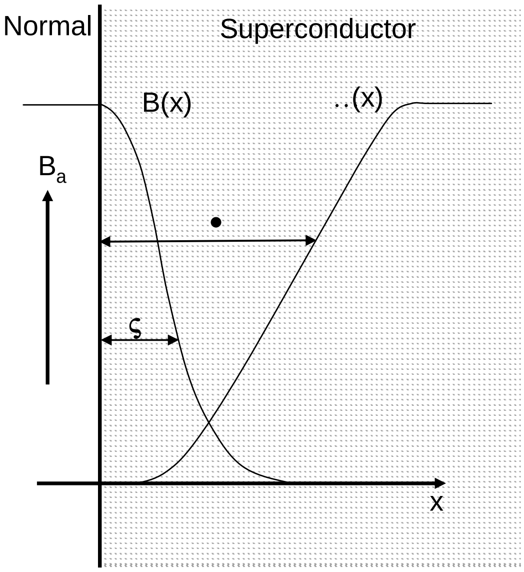

Fig. 1-1. Schematic representation of the coherence length, •, and penetration depth, ς, in the boundary between a normal region and a superconducting region.

The other characteristic property in a superconductor is the expulsion of the applied magnetic field from the material, for temperatures below the critical temperature. This is the so called Meissner effect [1]. The magnetic field is excluded from the superconductor by shielding currents flowing in a thin superficial layer at the sample edges, characterized by the penetration depth, ς(T), where the magnetic field drops exponentially from its applied value on the outside to zero inside (see Fig. 1-1).

The two lengths ς(T) and •(T) have the same dependence on the temperature, both diverges as $(T_c\text{-}T)^{-1/2}$ as we approach to T_c. Their ratio ρ=ς/• is the so called Ginzburg Landau Parameter, which distinguishes between two different families of superconductors, type I (ρ<1/· 2) and type II (ρ>1/· 2) superconductors.

In Type I superconductors magnetic flux is totally excluded from the material (Meissner effect) for applied fields below the critical field, H_c, and become normal at higher applied fields. Fig. 1-2a shows the magnetic phase diagram of a type I superconductor.

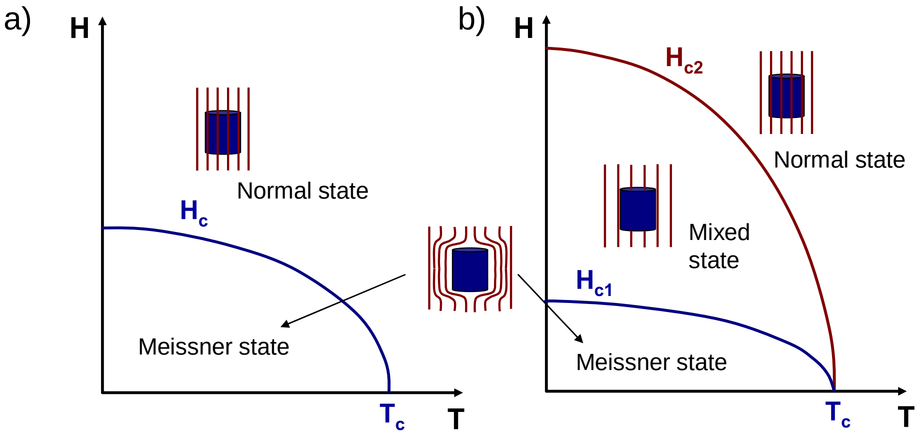

Fig. 1-2. Magnetic phase diagram for a type I (a) and type II (b) superconductors

In Type II superconductors the Meissner effect occurs when the applied magnetic field stays below the lower critical field, H_{c1}, but for applied fields above H_{c1}, magnetic flux starts penetrating into the material and the superconductor enters in the mixed state. When the applied magnetic field reaches a value called upper critical field, H_{c2}, the material becomes normal (Fig. 1-2b).

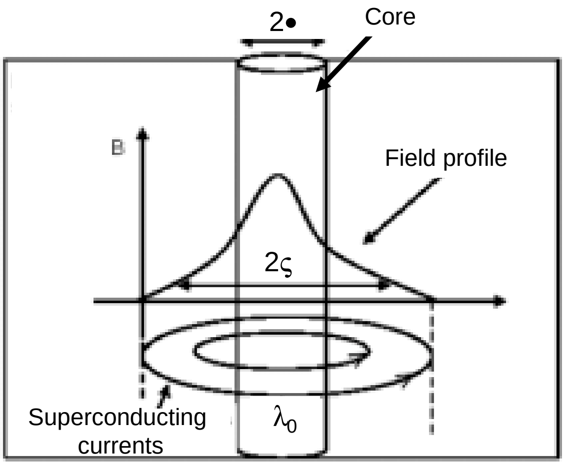

Fig. 1-3. Schematic representation of a vortex, formed by a normal core and surrounding supercurrents.

The magnetic field penetrating the superconductor in the mixed state, enters forming quantized cylindrical flux lines called vortices. The vortices have a normal core of radius •, where the density of cooper pairs is null. The core is surrounded by a region of larger radius, ς, within which superconducting currents are flowing, as it is illustrated in Fig. 1-3 . These currents generate a flux quantum in each vortex. In order to minimize the system total energy, vortex arrange in a regular array forming a triangular lattice, known as the Abrikosov lattice (Fig. 1-4) [1].

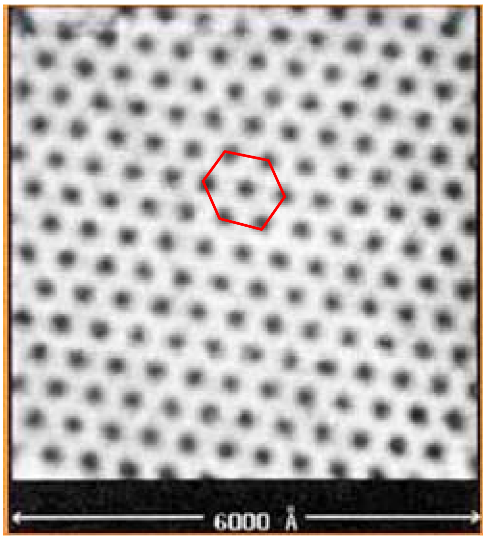

Fig. 1-4. STM image of vortices in a type-II superconductor. Flux lines are disposed in a regular array forming a triangular lattice (Abrikosov lattice).

In the mixed state, as soon as the flux lines start to move across the superconductor, energy dissipation appears in the material and it shows a resistance different from zero. However, in a real superconductor, the normal cores of vortices may be pinned by the impurities or imperfections present in the material retarding the appearance of dissipation.

1.2 HIGH TEMPERATURE SUPERCONDUCTORS (HTSC)

The discovery of high temperature superconductors by Bednorz and Müller in 1986 [3] opened a new area in the field of solid state physics in general and in superconductivity in particular since cooling is a critical factor for the utilization of superconductors. BCS theory has been very successful in describing conventional low temperature superconductivity (LTSC) assuming that electrons are coupled via electron-phonon interaction to form Cooper pairs. However, in HTSC it is not possible to explain the formation of Cooper pairs by considering only electron-phonon interaction due to the high T_c values. Different theories have been proposed for the origin of charge attraction in HTSC but this is still an open issue until now.

HTSC are mostly ceramic cuprate compounds with transition temperatures close to 100K. One of the most studied cuprate compounds is the $YBa_2Cu_3O_{7-\iota}$ (YBCO) which presents a critical temperature of 92K. This temperature is high enough to use liquid nitrogen as a refrigerant, making easy its technological application. As all the other cuprate superconductors, YBCO have anisotropic properties, in both normal and superconducting states due to its layered structure. In this thesis we have studied YBCO thin films and coated conductors and thus we will describe its particular structure.

Fig. 1-5 shows a schematic representation of the crystallographic structure of YBCO. It is formed by an array of Cu-O planes with the formula CuO_2 lying normal to the c direction. These plains contain mobile charge carriers and there is where superconducting current flows. The Cu-O planes are separated by charge-reservoir interleaved layers which allow a change in the carrier density available in the Cu-O planes. For YBCO, these interleaved layers contain CuO chains running in the b direction which contain free carriers and contribute to the normal conductivity. The current that can flow parallel to CuO_2 plains (a-b planes) is much higher than the current flowing through the c axis, i.e. $J_c^{ab}>>J_c^{c}$. So that, current has to flow through the a-b plane direction in order to get the maximum critical current density.

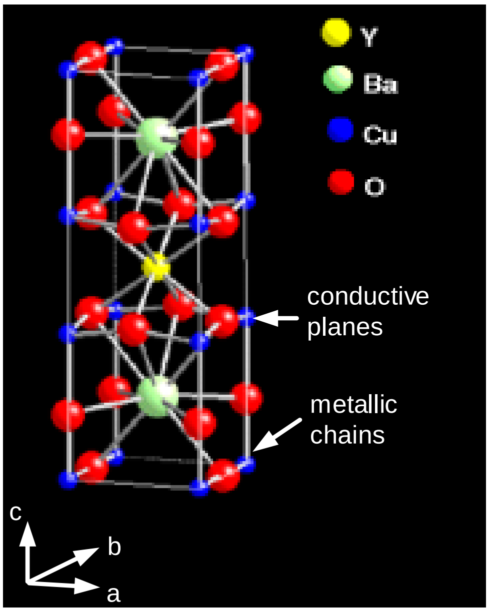

Fig. 1-5. Crystallographic structure of $YBa_2Cu_3O_{7-\iota}$ composed of two CuO_2 planes of strong superconductivity separated by charge-reservoir layers.

In particular, for superconducting films the c axis has to be oriented perpendicular to the substrate, so that current can be applied along the a-b planes. Fig. 1-6 shows a schematic representation of current flowing in a YBCO film with the c axis grown forming an angle ζ with the normal to the substrate (Fig. 1-6a) and a YBCO film oriented epitaxially, with the c axis perpendicular to the substrate (Fig. 1-6b). In the last case, when the current is applied parallel to the substrate surface, all the current can flow through the a-b planes, an thus the critical current density is much higher than in the first case where there is a component of the current which has to flow through the c axis.

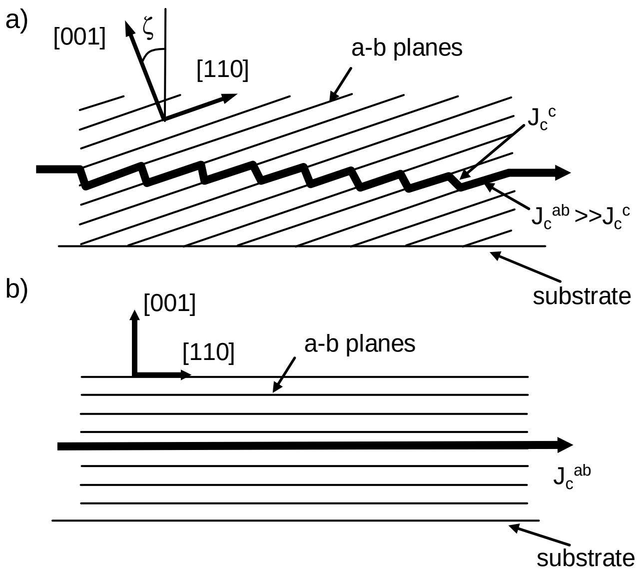

Fig. 1-6. Schematic representation of current flowing in a YBCO layer with the c axis tilted an angle ζ respect to the substrate normal (a) and with the c axis grown perpendicular to the substrate (b).

1.3 VORTICES IN HIGH TEMPERATURE SUPERCONDUCTORS

High temperature superconductors are strongly type II superconductors and, as such, their phenomenology is dominated by the presence of vortices over most of the phase diagram. The mixed state of high temperature superconductors contains a rich variety of vortex solid and liquid phases whose properties depend on magnetic field, temperature and disorder in the material.

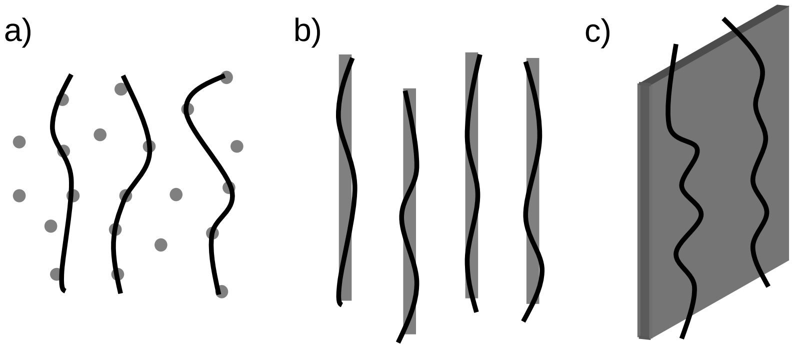

Fig. 1-7. Varieties of glassy states. Vortex glass state in presence of point defects (a) and Bose glass state in presence of columnar defects (b) or planar defects (c).

In clean, nearly defect free crystals at low temperature, an Abrikosov vortex lattice is expected. In the presence of weak random point defects like impurities, oxygen vacancies or electron irradiation, a vortex glass state has been proposed where long range translational and orientational symmetry is broken [4-6]. For correlated disorder, such as one dimensional columnar defects like dislocations or the amorphous tracks induced by heavy ion irradiation or two dimensional planar defects as twin boundaries, a Bose glass state has been predicted [7]. These various solid phases are shown in Fig. 1-7.

The nature of the solid phase is determined by the competition between the vortex-vortex interaction energy favouring a lattice and the vortex-pinning site interaction favouring a glass. At higher temperatures both of these energies are overwhelmed by the thermal energy, which melts by the solid to form a liquid describing a melting line in the H-T diagram [5,8,9]. At lower temperatures and fields vortices freeze into one of several possible solid phases, including a variety of "glasses" [5,7,10] (Fig. 1-8). In contrast to conventional superconductors, vortex dynamics in HTSC is strongly influenced by thermal fluctuations [5,8,9]. This is due to the combination of several factors, namely the higher transition temperatures, the very small coherence length and the large anisotropy resulting from their laminar structure. The main consequence of large fluctuation effects is that the vortex liquid may occupy a significant portion of the phase diagram (Fig. 1-8).

While HTSC single crystals with a very low density of weak defects exhibit a first order phase transition at the melting line [11,12], the dynamic response of less clean samples shows a second order phase transition [13], which is called irreversibility line (IL).

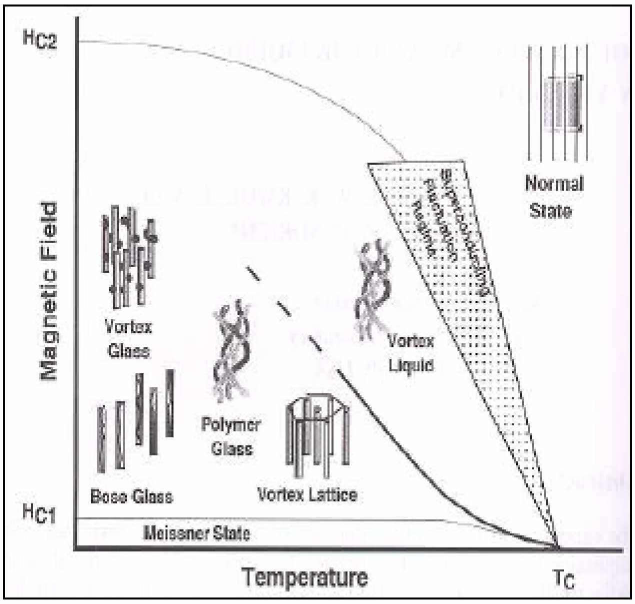

Fig. 1-8. Schematic representation of a magnetic phase diagram for a HTSC, showing the different vortex phases that may appear.

1.3.1 THE IRREVERSIBILITY LINE

In the region of the H-T plane above the IL, the material though being in the superconductor state in the sense that it has a finite order parameter, presents a substantial electrical resistance, corresponding to very easy flux motion (reversible system). Below the IL the resistance is zero, corresponding to effective flux pinning. The IL defines then the transition from an irreversible system to an reversible system (vortex liquid).

Fig. 1-9 presents the magnetic field-temperature phase diagram for five different type II superconductors where the upper critical field, H_{c2}, and the irreversibility line, IL, are indicated. Their different phase diagrams result from their distinctly different physical parameters and crystal structures. For the isotropic cubic LTSC, Nb-Ti and Nb_3Sn, the IL is about $0.85H_{c2}(T)$ [14]. All the other three higher T_c compounds have anisotropic layered structures, which result in significant anisotropy, vℑ2-3 for MgB_2, 5-7 for YBCO and 50-200 for Bi-2223. In all cases, due to this anisotropy, the irreversibility line is systematically much lower than $H_{c2}(T)$. The strongly anisotropic Bi-2223 exhibits an enormous suppression of the IL at 77K to the very low value of ℑ0.2T, well below H_{c2}(77K), which is of order 50T.

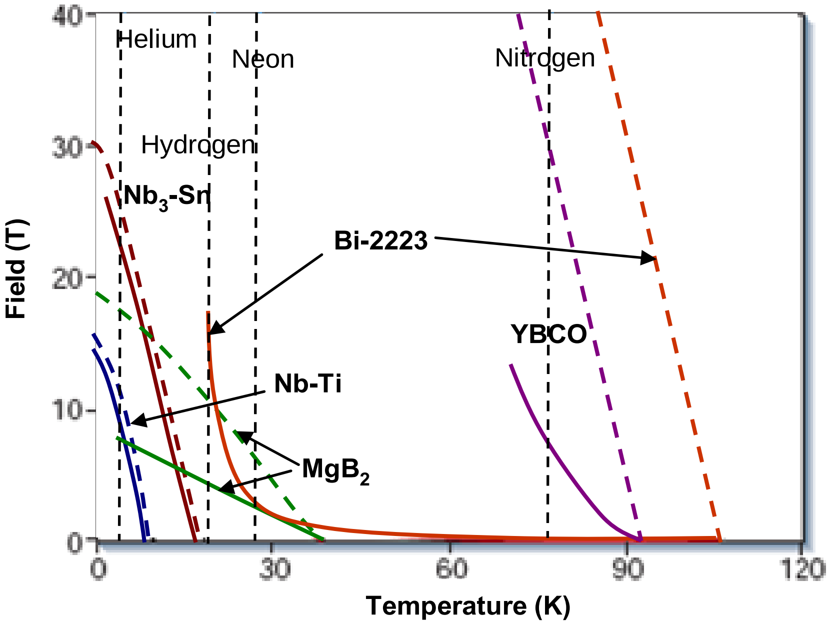

Fig. 1-9. Magnetic field-temperature diagram for several type II superconductors. The upper critical field, H_{c2}, is indicated as a dashed line, while the irreversibility line, IL, is indicated as a solid line.

1.3.2 THERMALLY ACTIVATED FLUX MOTION

Vortex motion is known to be potentially thermally activated. A simple theory of thermally activated flux motion was developed by Anderson [15], and applied to conventional type II superconductors. However, this effect is much more important in high temperature superconductors due to the large thermal energies involved.

Anderson considered a pinning potential for flux lines idealized in the form represented in Fig. 1-10. In Fig. 1-10a) no force has been applied (J=0) and the flux lines are held in wells of depth U_e. For thermal activated processes, the rate of hopping over a barrier may be written as $P\nabla\exp(U_e/kT)$. Consequently the probability of jumping is the same for all the directions and the average velocity is zero. In Fig. 1-10b) the flux is being driven in the right direction (J∏0), reducing the potential well on the right to U_e-W and increasing it on the left to U_e+W, where $W=U_eJ/J_c$. Then the net rate of jumping to the right is [15,16]

$$P \nabla e^{4U_e/kT}(e^{W/kT}\ 4\,e^{4W/kT}) \qquad 1\text{-}1$$

and the general expression of the electric field, E(B,T,J) generated by thermally activated flux jumps out of the pinning centres can be expressed as [15,16]

$$E(J) \,|\, 2\,\psi_c J_c \exp(4U_e/kT)\sinh(W/kT) \qquad 1\text{-}2$$

where $J_c(B)$ is the critical current density at T=0, $\psi_c(B,T)$ is the resistivity at $J=J_c$, $U_e(B,T)$ is the activation energy for flux jumps , W is the energy gain during a jump and k is the Boltzman constant.

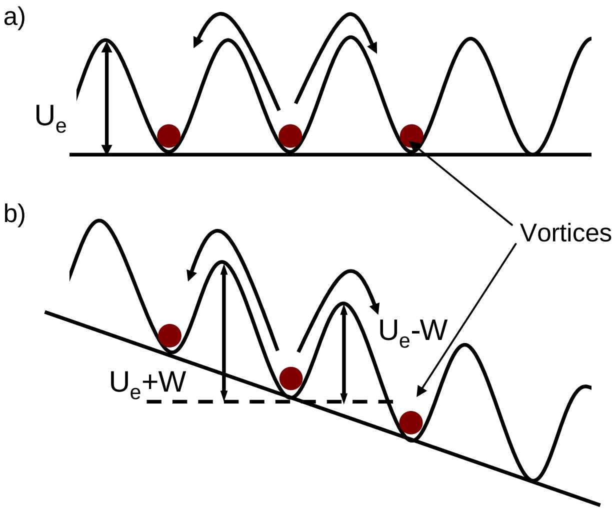

Fig. 1-10. Profile of the pinning potential in absence of any applied force, J=0 (a) and with an applied current, J∏0 (b).

According to equation 1-2, one found three different regimes for the resistivity, depending on the current density considered [15-17].

For large currents $J \Im J_c$ one has $W \Im U_e >> kT$ and thus $E \nabla \exp(J/J_1)$, with $J_1=J_c kT/U_e$. This regime is the so called flux creep regime and the resistivity is given by,

$$\psi \mid \psi_c \exp \Psi J / J_c \; 4 \; 1)U_e / kT \, \beta \nabla \exp(J / J_1) \qquad 1\text{-}3$$

For small currents $J<<J_1$ one may linearize the sinh(W/kT) in 1-2 and get an Ohmic behaviour with a thermally activated linear resistivity, $\psi_{TAFF} \nabla \exp(-U_e/kT)$. This regime is referred as thermally activated flux flow (TAFF), where the resistivity is defined as,

$$\psi \mid \frac{2\,\psi_c U_e}{kT} \exp(4 U_e / kT) \mid \psi_{TAFF} \qquad 1\text{-}4$$

For $J>>J_c$ the pinning force is much weaker than the driving force and thus a diffusive vortex motion occurs limited by a viscous drag. In this regime flux flows steadily with the usual flux flow resistivity of order $\psi_{FF} \Im \psi_n (B/B_c{}^2)$, where ψ_n is the normal resistivity, $B=\sigma_0 H$ is the magnetic flux density and $B_{c2}=\sigma_0 H_{c2}$, with H_{c2} the upper critical field.

$$\psi \mid \psi_{FF} (1 4 J_c^2 / J^2)^{1/2} - \psi_{FF} \qquad 1\text{-}5$$

Fig. 1-11 shows a schematic representation of the E(J) curve found for a superconductor with thermally activated flux motion with the three different regions indicated.

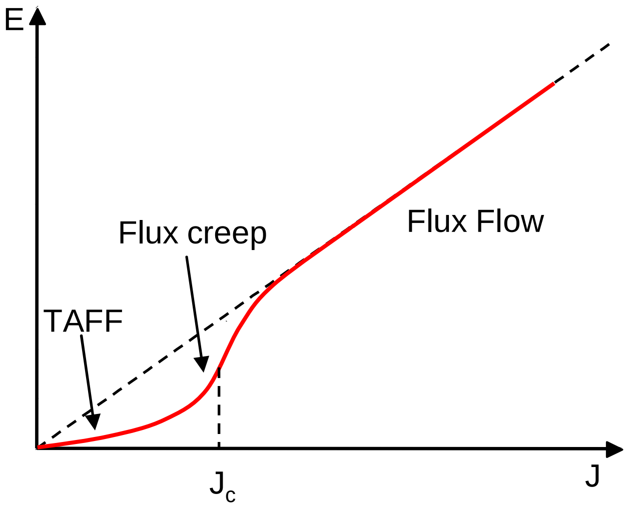

Fig. 1-11. –Schematic E vs. current density, J, for a superconductor with thermally activated depinning. At very low J one has Ohmic behaviour (TAFF), for $J \Im J_c$ E(J) increases steeply (flux creep) and for larger J one finds the usual flux flow regime where pinning is negligible.

A common phenomenological way to describe the electrodynamics in the flux creep regime is to assume a nonlinear current voltage relation (nonlinear resistivity), which can be described as [18,19]

$$E(J)\,|\,E_c(J/J_c)^n \qquad \text{1-6}$$

where n is the flux creep exponent that determines the degree of nonlinearity, or equivalently the importance of flux-creep effects. Small n means large creep effects. In the limit n=1 it describes an Ohmic conductor with constant resistivity which corresponds to the TAFF regime and for n⇓ ←the power law is equivalent to the Bean model (see section 3.1).

1.4 GRAIN BOUNDARIES

Grain boundaries (GB) are one of the principal limitation for critical current density in HTSC since they are strong barriers to the current flow. The depression of the critical current density flowing through grain boundaries has been widely studied in [20-24].

Grain boundaries are usually classified according the rotation of the crystals grains forming the GB as shown schematically in Fig. 1-12. A distinction is made between the tilt and twist components of the misorientation. Tilt component refers to a rotation around an axis in the plane of the grain boundary, and twist to a rotation of the crystal grains around the axis perpendicular to the grain boundary plane. In general, combinations of tilt and twist components may occur, leading to so-called mixed grain boundaries. GB with identical misorientations of the grains with respect to the grain-boundary interface are called symmetric, otherwise they are asymmetric.

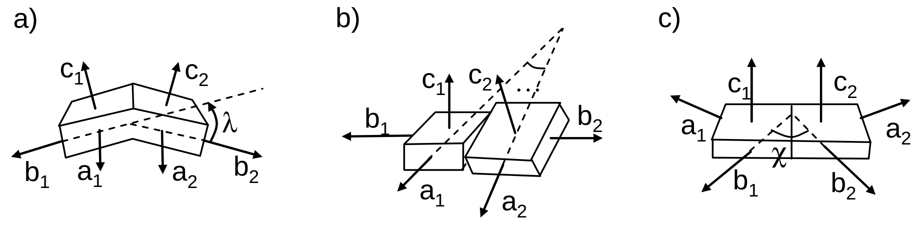

Fig. 1-12. Schematic diagram showing an a-axis tilt grain boundary (a), b-axis twist grain boundary (b) and c-axis tilt grain boundary (c).

A symmetrical tilt low angle grain boundary is built of a chain of edge dislocation with the Burgers vector, **b**, perpendicular to the GB plane [20,23-25] (Fig. 1-13). In general, the structure of a GB can be more complicated than the ideal one due to partial GB dislocations, long-range strain fields, and compositional variations near GBs [23,25]. The GB dislocation structure is the reason for the decreasing of $J_c(\chi)$ since near the dislocation cores there are regions of suppressed superconducting order parameter which block the supercurrent through GBs. These non superconducting regions can result from local compositional and hole concentration variations, additional electron scattering, and significant strains near the dislocation cores.

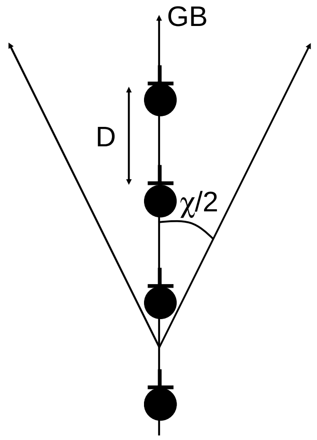

Fig. 1-13. Chain of edge dislocations which form a symmetric low-angle grain boundary. The non superconducting regions are shown are dark zones.

1.4.1 GRAIN BOUNDARY CRITICAL CURRENT DENSITY

For symmetrical tilt GB, assuming that the order parameter for superconductivity is depressed only within a strained region associated with the grain-boundary dislocations, the dislocation model predicts that the critical current density across a grain boundary, J_c^{GB}, is determined by the area of current channels of the GB between the dislocation cores [20,25]. Therefore the ratio of the critical current density across a grain boundary J_c^{GB}, to that within the grain, J_c^G, is

$$\frac{J_c^{GB}}{J_c^G} = \frac{D - 2r_m}{D} \qquad 1\text{-}7$$

where $D=|\mathbf{b}|/2\sin(\chi/2)$ is the dislocation spacing, b is the Burgers vector of the dislocation, χ is the tilt angle of two adjacent grains, and r_m is the effective radius of the non superconducting region around each dislocation core.

For small tilt angles, $D=|\mathbf{b}|/\chi$ and thus it appears a linear dependence

$$\frac{J_c^{GB}}{J_c^G} = 1 - \frac{2r_m}{|b|}\chi \qquad 1\text{-}8$$

The critical misorientation angle, above which the non superconducting regions overlap, and GBs become a continuous insulating or normal Josephson junction when $D=2r_m$, and thus,

$$\chi_c = 2\sin^{-1}(b/4r_m) \approx 20^o - 40^o \qquad 1\text{-}9$$

For $\chi>\chi_c$, the dislocation model predicts an exponential dependence of $J_c^{GB}(\chi)$ characteristic of a Josephson junction [25]. However the exponential dependence of $J_c^{GB}(\chi)$ is already observed experimentally for misorientations above χ ℑ4°-7° [21,24,26].

$$J_c^{GB}(\chi) \mid J_c(0)\exp(4\chi/\chi_0) \qquad 1\text{-}10$$

where $J_c(0)$ and χ_0 are constants.

The observed behaviour is consistent with models describing GBs as an array of parallel point contacts [27] that exhibit weak link behaviour when their width (or equivalently, the dislocation spacing) becomes smaller than the superconducting coherence length, •, that is, D-2r_m<•, or $\chi>\chi_1$ℑb/[•(T)+2r_m] (Fig. 1-14).

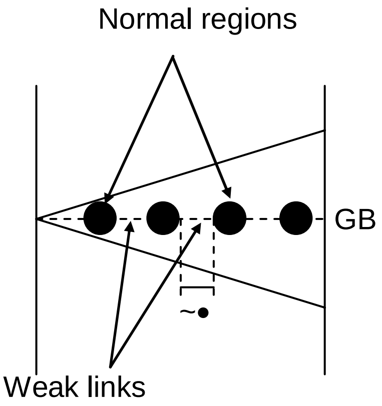

Fig. 1-14. Schematic representation of a grain boundary configuration in a bicrystal junction of $\chi>\chi_1$ℑ4°-7°.

For YBCO, at 77K, the in-plane •(T) is about 35Å and r_m=b=3.8Å, the critical angle χ_1ℑ5°, which correlates with the observed exponential decrease of $J_c^{GB}(\chi)$ above χ_1ℑ4°-7°. Fig. 1-15 shows experimental $J_c^{GB}(\chi)$ data of YBCO thin films grown on bicrystal substrates combined with J_c^{GB} measurements of textured polycrystalline tapes (IBAD and RABiTS coated conductors) with different texture degree [26]. In chapter 2 we will describe the granular structure of these particular samples and the average angle used as χ. For misorientation angles χ<4°, $J_c^{GB}(\chi)$ can be fitted with a linear dependence according to 1-8, while for χ>4° the $J_c^{GB}(\chi)$ dependence is exponential and can be fitted with equation 1-10 with $J_c(0)=3.2.10^{10}$A/m^2 and χ_0=3.2° (see Fig. 1-15).

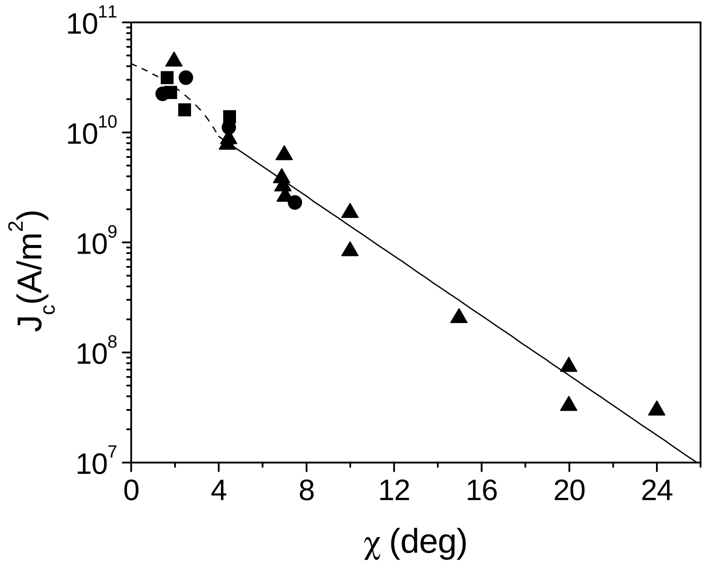

Fig. 1-15. J_c versus χ for YBCO thin films with a single GB (p) and granular IBAD (∉) and RABiTS (Á) coated conductors, at 77K. For misorientation angles, χ, below 4^o the curve fits a lineal dependence (dashed line) and for angles above 4^o the fitting curve is exponential (solid line)[26].

This strong dependence of $J_c^{GB}(\chi)$ dictates the need to shift the grain boundary misorientation angle, χ, to as small values as possible in order to obtain high critical current densities. In the particular case of having polycrystalline samples it will be very important to texture them in order to obtain well aligned grains, avoiding high angle grain boundaries.

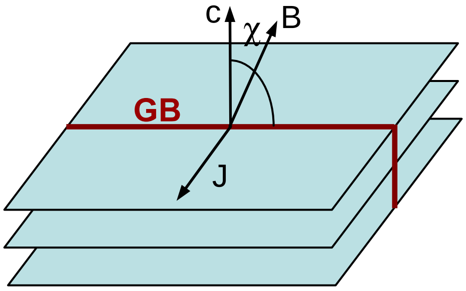

Fig. 1-16. Schematic representation of the current and magnetic field directions disposed in a measurement of J_c as a function of the magnetic field direction within the grain boundary, $J_c(\chi)$, where a peak of J_c is obtained at $\chi\Im 0$ due to pinning of GB dislocations.

However, since the effective size of the dislocation cores is of the order of the vortex coherence length, an active flux pinning has been observed by dislocations in LAGB. Measuring the angular dependence of J_c^{GB} when rotating the magnetic field within the grain boundary plane (Fig. 1-16) one observes a peak in J_c for fields aligned with the c axis of the film, $\chi\Im 0$, i.e. when the magnetic field is aligned with the array of dislocations indicating an effective vortex pinning by dislocations in the GBs [28]. So that, the J_c of a current track containing a LAGB is determined by the balancing of two opposing effects, the reduction in the effective GB cross section by the dislocation cores (the current flow through the undisturbed channels between dislocations) and the enhanced flux pinning due to accommodation of vortices in the dislocation array.

1.4.2 VORTICES AT THE GRAIN BOUNDARIES

The extreme sensitivity of $J_c^{GB}(\chi)$ to the misorientation angle makes a grain boundary a unique tool to trace the fundamental transition between Abrikosov vortices (AV) and Josephson vortices (JV) in a magnetic field above the lower critical field, H_{c1} [29]. For $\chi<<\chi_c$, vortices on a GB are AV with normal cores pinned by GB dislocations [28]. For $\chi>\chi_c$, the maximum vortex current density circulating across the GB is limited to its $J_c^{GB}(\chi)$, much smaller than the bulk depairing current density, J_d (current density that breaks Copper pairs). Since vortex currents must cross the GB which can only sustain $J_c^{GB} << J_d$, the normal core of an AV turns into a J core, whose length $l\Im\bullet J_d/J_c^{GB}$ along the GB is greater than $\bullet$, but smaller than the London penetration depth, ς, $J_c^{GB} > J_d/\rho$, where $\rho=\varsigma/\bullet\Im 10^2$ for YBCO [29]. As χ increases, the core length $l(\chi)\Im\bullet J_d/J_c^{GB}(\chi)$ increases, so the GB vortices evolve from AV for $\chi<<\chi_c$ to mixed Abrikosov vortices with Josephson cores (AJV) at $J_d/\rho<J_c^{GB}<J_d$. The AJV turn into J vortices at higher angles, $\chi>\chi_J$ for which $l(\chi)$ becomes greater than ς. Therefore, the AJV determine the in-field behaviour of GBs in a rather wide range of misorientations, $4^o<\chi<\chi_J\Im 22^o$-40^o, which comprises the crucial region of the exponential drop of $J_c^{GB}(\chi)$ and which comprehend the range of misorientation angles considered in the coated conductors that we will analyze, 4^o-12^o (see section 2.2.4).

The 1D AJV networks have two length scales, the core size along the GB, $l>\bullet$, and the intervortex spacing $a=(\lambda_0/B)^{1/2}$. The elongated core of AJV leads to their weaker pinning along a GB, which becomes a channel for motion of AJV between pinned AV at the grains [29,30] (Fig. 1-17). However, up to now, there is no evidence of experimental observation of the cores of GB vortices, since the lack of normal core makes AJV “invisible” under STM (scanning tunnelling microscope), while neither the Lorentz microscopy nor magneto optics have sufficient spatial resolution to distinguish AV and AJV. Magnetic decoration may probably be the best candidate.

Pinning of AJV results from interaction of the AJV phase core with structural inhomogeneities of GB and the magnetic interaction of AJV with more strongly pinned AV in the grains [31].

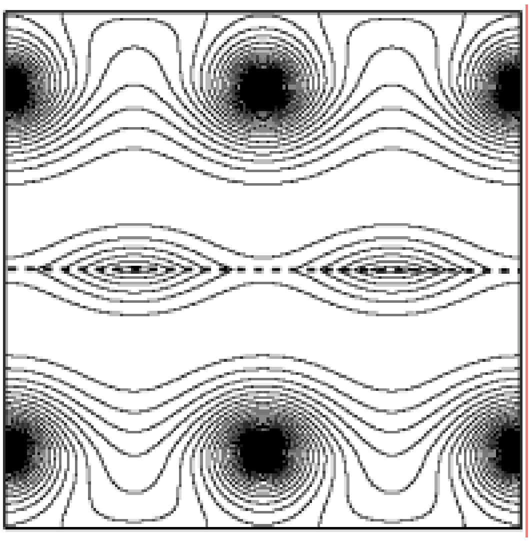

Fig. 1-17. Current streamlines around AJV on a GB (dashed line) and the bulk AV in the grains [31] .

The percolative motion of AJV gives rise to a linear region in the V-I characteristic of HTS policrystals that is dominated by motion of AJV along GBs [30,32,33]. This behaviour corresponds to a measure of the flux flow state in the AJV motion which is usually found in transport experiments. When the current density exceeds the critical current density, the narrow line of vortices pinned at the GB moves in response to the Lorentz force acting on the vortices, generating a voltage, V, across the boundary [30,32,33]. It should be noted that this voltage is generated over a very short distance, of the order of a_0 (see Fig. 1-18), around the boundary. As a consequence, even for very low voltages, very high electric fields, E, are generated and dissipation is dominated by viscous flux flow giving a linear V-I curve. However, by ac-susceptibility or magneto optical measurements it is possible to obtain transport properties of grain boundaries in the TAFF or flux creep state measuring at very small electric field levels [34,35]. At high electric fields it has been observed that motion of AJV can start dragging neighbouring rows of AV in a flux flow channel along GB [30,32,33].

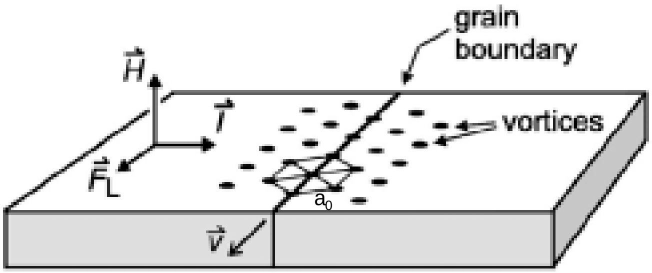

Fig. 1-18. Sketch of the hexagonal vortex lattice in the vicinity of a GB. For an applied field, H, within the plane of the grain boundary, vortices are pinned at the GB. However, when current in excess of the critical current density is applied, vortices at the GB start to move with a velocity v [32].

1.5 HIGH T_C SUPERCONDUCTING WIRES

Superconductivity can have a significant role in electric power applications such as magnets, motors, transformers and transmission lines. However, significant market penetration of HTS devices requires high T_c superconducting wires that fully exploit their fundamental current-carrying capability.

The goal is to produce robust, economical, and scaleable processes for making wires that can carry sufficient current at liquid nitrogen temperature in presence of high magnetic fields. Nowadays two different kind of superconducting wires have been developed. Those denominated first generation tapes fabricated by the powder-in-tube method using a Bi-based superconductor [36,37] and the second generation tapes based in textured YBCO coatings grown on metallic substrates [38-40].

1.5.1 FIRST GENERATION SUPERCONDUCTING TAPES

Bi-based wires and tapes are made by the powder-in-tube technique. This process consists of different sequences of heat treatment steps separated by intermediate rolling steps performed in silver tubes filled with superconducting Bi-based powder in the phases $Bi_2Sr_2CaCu_2O_{8+\iota}$ or $(Bi,PL)_2Sr_2Ca_2Cu_3O_{10+\iota}$ (BSCCO). By means of mechanical deformation and thermal treatments in the tubes, one obtains an uniaxial texture in the superconductor, since all the crystals are oriented with the a-b planes parallel to the BSCCO-silver interface Fig. 1-19

Fig. 1-19. Cross section of a first generation superconducting wire, where several Bi-2223 filaments are encased in a silver matrix.

This progress has enabled to produce superconducting wires of long length (up to 1000 m) but, due to the very low irreversibility line of the Bi-based superconductors (see section 1.3.1), high current at high field applications of these wires are restricted to lower temperatures. At 77K only a maximum field of 0.2T can be applied.

1.5.2 SECOND GENERATION SUPERCONDUCTING TAPES

YBCO superconductor is more isotropic than BSCCO, thus having a much higher IL which allows applications at high magnetic fields (7-10T) in liquid nitrogen (77K). However, for YBCO, the production of wires by the powder-in-tube process is not well suited since large angle grain boundaries cannot be avoided. In order to get long length superconducting tapes, the most promising method so far is the deposition of highly textured YBCO on flexible metallic tapes. In this work we have studied these YBCO coated conductors (CC) and thus we will describe them in more detail.

1.5.2.a SUBSTRATE REQUIREMENTS FOR COATED CONDUCTORS

Good quality YBCO coated conductors can only be obtained if the YBCO layer is grown on high textured non reactive substrates with a good matching between the different crystallographic cells and similar thermal expansion coefficient. In addition, for conductor applications, the substrate must be flexible and available in long lengths and therefore needs to be metal based.

Uniaxially aligned YBCO films (with the c axis perpendicular to the substrate) are easily grown on polycrystalline substrates, but the superconducting properties are heavily degraded at the grain boundaries where the in-plane a and b axis are disoriented as shown in Fig. 1-20a (See section 1.4). The only way to obtain good properties is by forming a biaxially aligned structure with both c-axis and a-b basal planes of all grains aligned (Fig. 1-20b). The most essential point is thus, how to obtain such a textured structure on metallic flexible substrates.

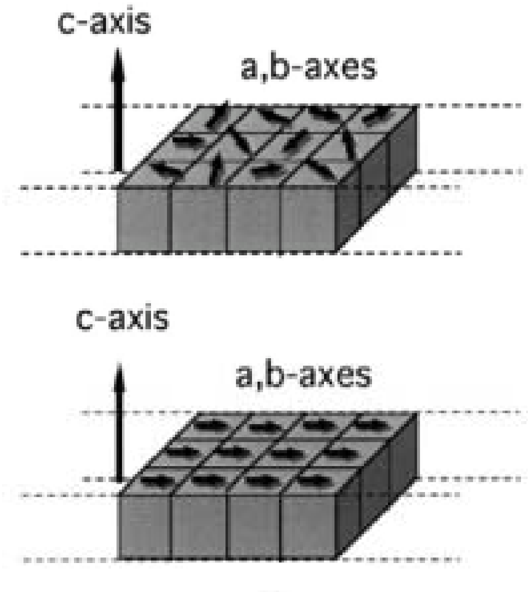

Fig. 1-20. Schematic diagrams for crystalline alignment structures of YBCO superconducting tapes uniaxially aligned (a) and biaxially aligned (b).

There are two different basic architectures of YBCO coated conductors, where the texturing processes are either applied on the metallic substrate or on a ceramic buffer layer grown on a polycrystalline metallic substrate.

1.5.2.b DESCRIPTION OF IBAD COATED CONDUCTORS

In the ion beam assisted deposition (IBAD) process, an insulating buffer layer, YSZ (yttria-stabilized zirconia), GZO (gadolinium zirconiate) or MgO, is deposited in a vacuum system onto a polycrystalline substrate (typically made of Inconel, Hastelloy or stainless steel). The trick is to perform this deposition in the simultaneous presence of an argon ion beam directed at an angle to the surface so that eliminating the undesired orientations and obtaining a biaxially textured buffer layer [41-43] Fig. 1-21 shows a schematic diagram of the IBAD system, in which two sets of ion sources are used. One is used for sputtering the target material onto the substrate and a secondary one is used for ion bombardment of growing films. This system is called a dual-ion-beam sputtering system. This method allows free choice of the desired substrate materials because no crystalline alignment of the metallic substrate is needed.

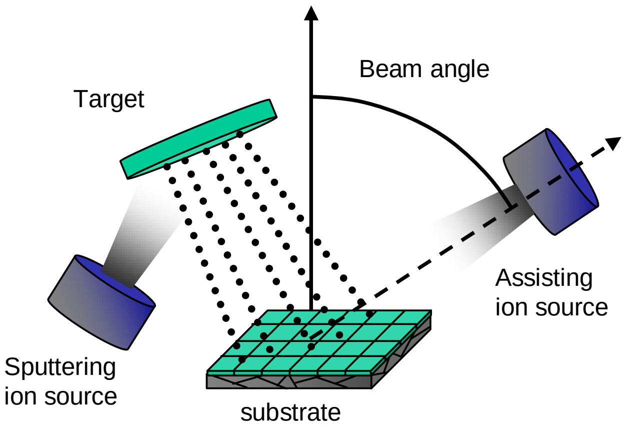

Fig. 1-21. Schematic diagram of the ion beam assisted deposition (IBAD) system.

Once the textured template IBAD buffer layer is obtained, a YBCO layer can be grown epitaxially onto this buffer layer by using standard vacuum techniques (Pulsed Laser Deposition (PLD), Thermal evaporation..) or by using chemical solution techniques (Liquid Phase Epitaxy (LPE), Chemical Vapor Deposition (CVD), Metal Organic Decomposition (MOD)..). Then, the ion beam induced texture is transferred to the superconductor. Additionally, some extra buffer layers can be grown between the IBAD-textured layer and the YBCO in order to enhance crystallographic coupling between different layers and avoid chemical reactivity. Perovskite buffer layers such as $SrTiO_3$ (STO), $BaZrO_3$ (BZO), and $SrRuO_3$ (SRO) are used and also a fluorite buffer of CeO_2 which forms an excellent template for YBCO growth. Fig. 1-22 shows an schematic representation of the typical layer architecture in an IBAD coated conductor.

On IBAD-MgO templates, 1.4σm thick YBCO films with I_c values of 109A/cm-with (3.8m length) and 144A/cm-width (1.6m length) have been achieved at 77K (LANL). On IBAD-YSZ templates one have values of I_c=360/cm-width (8m length)

(ZFW Göttingen) and on IBAD-GZO I_c=126A/cm-width, 105 m (Fujikura). In all these coated conductors the YBCO layer has been grown by PLD.

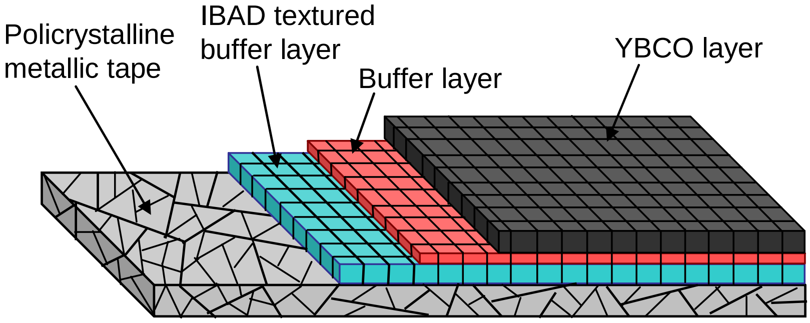

Fig. 1-22. Schematic diagram of biaxially aligned YBCO coated conductor using an IBAD textured buffer layer.

1.5.2.c DESCRIPTION OF RABiTS COATED CONDUCTORS

In the rolling assisted biaxially textured substrate (RABiTS) process [44-46], a flexible metallic tape is biaxially textured by rolling and annealing processes (Fig. 1-23). FCC materials such as nickel, copper or silver can be used since in these materials a biaxial texture can be obtained only by adequate heat treatment after cold rolling. Up to now nickel or nickel alloyed RABiTS substrates are used since cooper needs to be protected from oxidation while silver substrates present problems of re-crystallization at the temperatures where YBCO has to be deposited.

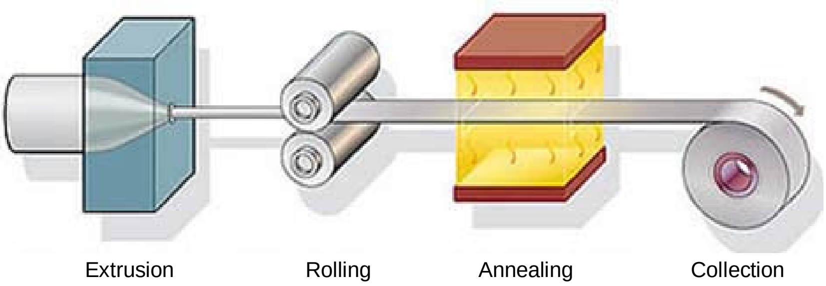

Fig. 1-23. Schematic drawn of the rolling assisted biaxially textured (RABiTS) process.

In the RABiTS process, the use of an already textured metallic substrate avoids the need to use special methods to texture any buffering layer and thus they can be epitaxially deposited by conventional methods before the superconducting film is grown. Buffers must provide good adhesion with the substrate, a barrier to diffusion of metal atoms up from the substrate, and good mismatch with the YBCO layer. The YBCO superconducting layer is then deposited epitaxially on the buffer layer by means of the same techniques used for the IBAD substrates (Fig. 1-24).

The buffer layer architectures most commonly used in RABiTS coated conductors such as CeO_2/YSZ/Y_2O_3/Ni, CeO_2/YSZ/Y_2O_3/ or YSZ/CeO_2 involve several layers in general grown by vacuum techniques. With this architectures, 10m lengths with I_c=250-270A/cm-width have been obtained (ORNL, AMSC). However simpler architectures based on two effective Ni diffusion barrier layers, $LaMnO_3$ (LMO) and $La_2Zr_2O_7$ (LZO) with an optional cap layer of CeO_2 are already developed with low cost chemical solutions where up to now the value of $J_c=2.7\cdot10^{10}A/m^2$ (short length) has been achieved (ORNL, AMSC).

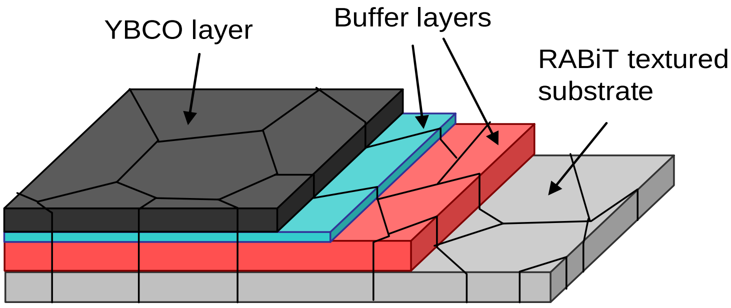

Fig. 1-24. Schematic diagram of a biaxially aligned YBCO coated conductor using a RABiTS textured metallic substrate

1.5.3 PERCOLATIVE CURRENT FLOW IN COATED CONDUCTORS

Although high textured YBCO layers can be achieved by means of the IBAD or RABiTS techniques, inherent granularity induced by the metallic substrate is present in YBCO coated conductors. Because of the strong dependence of the critical current density J_c on grain boundary angle, the current transport in these materials flows in a percolative way through the network of grain boundaries [26,47-49]. This behaviour is clearly visible with Magneto-optical imaging where non uniformities of current flow can be identified. Fig. 1-25 shows a representative MO image of flux penetrating into a typical RABiTS coated conductor, which evidences preferential flux penetration along grain boundaries.

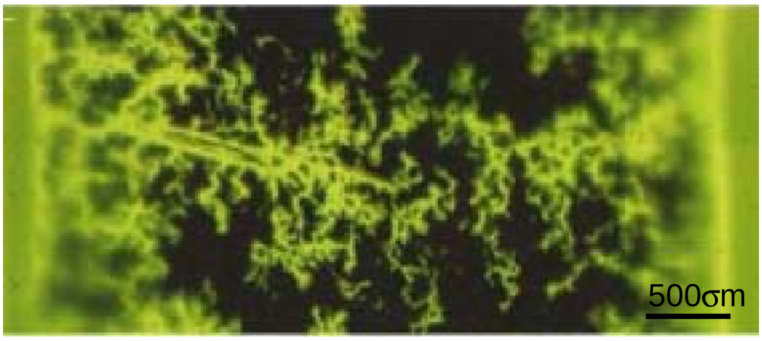

Fig. 1-25. MO image of a YBCO coated conductor taken after cooling in zero field to 15K and applying a field of 60mT. Bright areas indicate magnetic flux penetration and dark areas flux shielding [48].

Several 2D percolative models have been developed in order to study the probability of percolation through a sample and the restricting paths for current flow which limit the critical current density across coated conductor [50-52]. Fig. 1-26 shows a possible representation of the two-dimensional grain structure in a YBCO coated conductor with identical regular polygons in a hexagonal array.

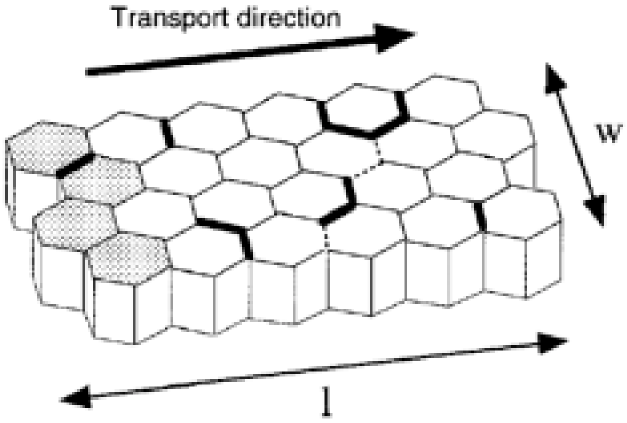

Fig. 1-26.Schematic representation of the granular structure in a YBCO coated conductor of with w and length l by means of a two-dimensional hexagonal array. In the model, current is injected for the shadowed grains on the left and flow across the sample [51].

When a given angle criterion is imposed, the grain boundaries become either “open” or “closed” depending on whether their misorientation is smaller or greater than the threshold. The percolation probability is an indication of the possibility that an open path exists from one end of the sample to the other. If such a path does exist it is useful to identify what fraction of the sample width is open, i.e. whether there is effectively free flow across the whole width of the sample, or whether percolation through the tape is restricted within few grains. For the sample represented in Fig. 1-26 with a certain value current transport, all the boundaries are considered to be open, except those marked with a heavy line. Percolation to the other side can occur, hence in this sample the percolation probability is 1. The region marked with a dotted line, is the limiting path, where only 3/7 of the sample width is open. Percolation models predict that high critical current densities are obtained in short and wide samples.

A coated conductor may be then considered as a superconducting network of low-angle grain-boundaries through which a percolative current flows, separating superconducting grains. However, by means of percolative models it is not possible to study the interaction between grain and grain boundary current densities. In this thesis we have developed an inductive methodology based on dc-magnetometry that has enabled us to determine simultaneously J_c^G and J_c^{GB} of coated conductors and therefore has allowed us to analyze the relationship between the two critical current densities in a systematic manner.

1.6 THESIS CONTENT

In Chapter 2 we have described the basic characteristics of the different samples analyzed and the experimental techniques that we have used.

In Chapter 3 we present a general background of the theoretical models that we have considered in this Thesis. We have described the influence of the geometrical shape of the superconducting samples in the magnetization hysteresis loops, ac-susceptibility response and flux and current distribution in the sample. We have considered the limit of thin specimens.

In Chapter 4 we compare the magnetic hysteresis loops measured for non-granular thin films with the ones obtained for coated conductors. By analysing the behaviour of several minor hysteresis loops measured in coated conductors we have developed an inductive methodology that allow us to determine the grain, J_c^G, and grain boundary, J_c^{GB}, critical current densities and the magnetic grain size, <2a>, of YBCO coated conductors. In this chapter we present the bases of this methodology and we show several tests performed to our model which demonstrates its consistency and check the validity of our assumptions.

In Chapter 5 we present data of both J_c^G and J_c^{GB}, determined in several coated conductors by varying some characteristic parameters, such us the YBCO grain size, the texture of the conductors, the YBCO thickness or the effects of mechanical deformation of the tapes. We show a complete analysis of the obtained data which has allowed us to study the interaction between the two critical current densities and thus infer in the interaction between the Abrikosov vortices located inside the grains and the Abrikosov Josephson vortices located at the grain boundaries. By analysing the magnetic field dependence of J_c^G in non-granular thin films and J_c^{GB} in coated conductors we have built a phase diagram which differentiates between different regimes of vortex motion.

In Chapter 6 we present a complete analysis of the ac response measured in non-granular YBCO thin films and coated conductors. By means of this analysis we have identified different percolative grain boundary domains associated to the granular nature of YBCO coated conductors which may generate an important dissipation in the coated conductor. Additionally we present a dynamic phase diagram of vortex motion in these particular materials and analyze the activation energies for thermally activated flux motion of coated conductors in comparison with those of non-granular material.

We finally include the different vortex states in a single magnetic phase diagram where both, the magnetization and ac-susceptibility results are joined and which enables to describe the behaviour of AJV and JV in coated conductors

CHAPTER 2

EXPERIMENTAL TECHNIQUES AND BASIC SAMPLE CHARACTERIZATION

2.1 EXPERIMENTAL TECHNIQUES

The techniques that we have directly used in this Thesis to characterize non-granular YBCO thin films and coated conductors are presented in this section. Dc-magnetometry and ac-susceptibility measurements have been performed at the “Institut de Ciència de Materials de Barcelona (ICMAB)”. MO imaging was done at “Zentrum für FunktionWekstoffe” in Göttingen (Germany) during my short stay of 1 month, in collaboration with Prof. H.C. Freyhardt and Dr. Ch. Jooss. Moreover some magneto optic images carried out by Dr. D.M. Feldmann at the University of Wisconsin (UW) are presented. Transport measurements have been performed during my stay of 2 month at Oak Ridge National Laboratory (ORNL) in Oak Ridge (USA) thanks to the collaboration with Dr. R. Feenstra. Recenly transport critical currents have also been performed by other members of the superconducting group at ICMAB and will also be presented.

Additionally, a brief description of the EBSD technique will be given for the importance of the results presented in this Thesis. The EBSD analysis has been performed by Dr. D.M. Feldmann at the University of Wisconsin (UW).

2.1.1 DC-MAGNETOMETRY MEASUREMENTS

We have analyzed the electromagnetic response of coated conductors by means of dc-magnetometry. Dc-magnetic measurements determine the value of the magnetization in a sample magnetized by a constant magnetic field. The magnetic moment as a function of the applied field is measured, producing a dc-magnetization curve M(H). Magnetic hysteresis loops have been measured with two Quantum Design SQUID (Superconducting Quantum Interference Device) magnetometer provided with a 5.5 T and 7 T superconducting coils.

The magnetometer integrates a SQUID detection system and a precision temperature control unit in the bore of a high-field superconducting coil. The sample is located inside the superconducting coil so that a uniform dc-magnetic field can be applied. The detection system is based in a set of pickup coils which are placed in the centre of the superconducting coil; the sample is then displaced through the coil set, inducing a current in the detection coils proportional to magnetic flux variation. The signal is amplified by means of a SQUID sensor which converts current to voltage achieving a high sensibility. Hence, the magnetic moment induced by the sample is proportional to the voltage variations that the SQUID detects, which can resolve magnetic moments as small as 10^{-9} Am^2 (10^{-6} emu). All the system is located inside a Helium cryostat which refrigerates the superconducting coil and allows a temperature variation in the sample place from 5K to room temperature. In order to assure a good homogeneity of field and temperature during the measurement, we have used scans of 2cm through the coil set.

The sample is mounted with the dc-magnetic field applied perpendicular to the substrate and the standard measurements of magnetic hysteresis loops have been performed cooling the sample at zero field (ZFC).

2.1.2 AC-SUSCEPTIBILITY MEASUREMENTS

Ac magnetic measurements yield information about magnetization dynamics which are not obtained in dc-measurements. Since the ac measurement is sensitive to the slope of the magnetization curve, M(H), and not to the absolute value, small magnetic shifts can be detected even when the absolute moment is large. Ac-susceptibility measurements have been performed in order to study dissipation mechanisms present in granular YBCO coated conductors. Ac-susceptibility curves have been measured with an ac Measurement System (ACMS) integrated in a Quantum Design PPMS (Physiscal Property Measurement System).

An ACMS coil set, which provides the excitation field for ac measurements includes the detection coils that measure the sample's magnetic response. The coil set is located concentric inside a superconducting coil of 9T which allows applying a dc-magnetic field superimposed to the ac drive magnetic field. To increase the accuracy of the phase and amplitude calibration during each measurement, a calibration coil array is used. To perform the ac measurement, a small ac drive magnetic field is superimposed on the dc-magnetic field, causing a time-dependent moment in the sample. The field of the time-dependent moment induces a current in the pickup coils, allowing measurement without sample motion with a sensibility of 10^{-11}Am^2 (10^{-8} emu). The detection circuitry is configured to detect only a narrow frequency band, normally at the fundamental frequency (that of the ac drive field). Drive coil frequency can go from 10Hz to 10KHz, temperature range from 1.9K to 350K and driving ac amplitude from 0.2σT to 1.5mT. Both ac and dc-magnetic fields are applied perpendicular to the sample substrate.

2.1.3 MAGNETO OPTICAL IMAGING

The magneto-optical (MO) Faraday-effect represents an excellent method for the space-resolved measurement of the magnetic flux density distribution of a superconductor [53-55]. According to this effect, when linearly polarized light passes through a magnetized medium, the plane of polarization is rotated with an angle which is proportional to the magnetic field. Since up to now a significant Faraday Effect of superconductors is not observed, one has to use magneto optical active layers (MOLs) as indicators, which are placed or evaporated on top of a superconductor. The magnetic field distribution in the superconductor is imaged by detecting the rotation of the polarization plane of a linearly polarized light within the MOL.

MO experiments have been performed by a device designed at the “Zentrum für FunktionWekstoffe” [56]. The system includes a polarized light microscope, an optical cryostat, an electromagnetic coil for the generation of magnetic fields and a CCD (Charge-Coupled device) camera for image recording. The polarized light microscope consist of a stabilized light source with sufficient power, a polarizer, an analyzer and optical components to project the image into the recording system. The superconductor with a MOL is placed in the light beam path between the polarizer and the analyzer crossed 90 degrees. Magneto optical measurements are performed in reflection mode by using ferromagnetic doped iron indicator films with a mirror layer deposited on top (see Fig. 2-1). The light enters the MOL and is reflected at the mirror layer. In areas where no flux is present in the sample, no Faraday rotation takes place hence these regions stay dark in the image. In all areas where flux is present, the Faraday rotation changes the polarization plane so that this light is able to pass through the analyzer thus leading to bright areas. The special resolution of this system is limited by the film thickness of the iron garnet, the measurement height, when the MOL is placed onto the surface of the superconductor and the resolution of the optical microscope. Typically, a spatial resolution of ℑ5σm is achieved.

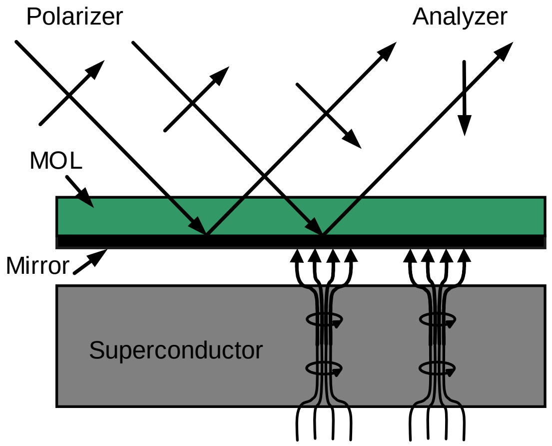

Fig. 2-1. Basic principle of the measurement of the magnetic flux distribution of superconductors by magneto-optical technique.

2.1.4 TRANSPORT MEASUREMENTS

A four-probe method has been applied to determine the critical current density of YBCO coated conductors with transport measurements. Since the voltage drop across the contact resistant of the current leads is generally much larger than the voltage across the sample itself, the latter must be measured with a separate pair of terminals. So that, four silver paths of 0.1σm in thickness has been sputtered onto the YBCO layer. After the deposition a thermal treatment in flowing oxygen has to be applied to assure a good silver diffusion and reduce the contact resistivity. Transport current is introduced in the sample through copper leads placed by pressure onto the silver paths. Between the copper and the silver, there is an indium layer which allows a good connection. This makes possible to apply at the system a maximum current of 40 A without significant heating.

Transport properties have been measured in a He-gas flow cryostat equipped with a magnet of 9 T with currents going from 1 σA to 40 A. For current values >100 mA, current pulses of 50ms have been applied in order to reduce heating while retaining sufficient voltage sensibility. Data have been taken upon cooling the sample in zero field (ZFC). Critical current densities have been determined using a 1σV/cm criterion onto the sample width. Temperature in the inset can be changed from 5K to 300K.

2.2 SAMPLE DESCRIPTION, MICROSTRUCTURAL CHARACTERIZATION AND BASIC SUPERCONDUCTOR PROPERTIES

In this section, we will describe the different variety of samples analyzed and we present the results of microstructural and magnetic basic characterization performed to these samples. Several YBCO IBAD and RABiTS coated conductors grown by means of different techniques have been studied as well as YBCO films grown on single crystal substrates prepared in the same way. A description of the IBAD and RABiTS substrates has been presented in section 1.5.2. The deposition of a YBCO layer epitaxially grown onto these substrates has been performed by Pulsed Laser Deposition technique (PLD) or by a BaF_2 ex situ process using e-beam evaporated precursors.

2.2.1 PULSED LASER DEPOSITION OF THE YBCO FILM

Two different kind of samples grown by pulsed laser deposition (PLD) have been analyzed. Samples grown at the “Zentrum für FunktionWekstoffe” in Göttingen (Germany) with Prof. H.C. Freyhard and at the IFW in Dresden (Germany) with Dr. B. Holzapfel.

The coated conductors prepared in Dresden consist of a buffer layer architecture composed of a thin layer of $Ce0_2$ (50nm) grown directly onto a RABiTS Nickel tape, and a thick layer of YSZ (600nm) with the YBCO layer of variable thickness on top. The films were deposited in a standard PLD geometry using a KrFexcimer (Lambda-Physik LPX305i) laser running at fΩ50Hz with a deposition rate of about 0.1nm/pulse. The deposition of the YBCO was carried out in an oxygen atmosphere with a substrate temperature of 770^{o}C. Nickel-0.1% Manganese (Ni-Mn) RABiTS with a typical thickness of 100σm were used as substrates [44]. For the coating process the tapes were cut into pieces of about 1x1cm^{2}.

CCs prepared in Göttingen were grown with a high-rate pulsed laser deposition (HR-PLD) technique [40]. This technique enables a considerable increase of the integral deposition rate together with a large area deposition. It is based on scanning a large-area target with the laser beam and it is capable of HTS film depositions on long flexible ribbons with a width from 10 to 200 mm and with lengths of several meters. An integral deposition rate of 35 nm m^{2}/h was achieved using an industrial LAMBDA 3308 laser with fΩ300Hz. The substrate employed consists of a polycrystalline 100σm Cr-Ni Stainless steel (SS) exhibiting a high stability in oxygen at high temperatures. The metallic tape was coated with an IBAD-YSZ layer with a thickness of 1.1-1.5σm [40,41]. In order to improve the final texture of the YBCO layer, an intermediate buffer layer of CeO_2 (ℑ1σm) was grown on top of the IBAD-YSZ in some of the CCs. For the magnetic analysis of the samples, small pieces of about 5x5mm^{2} were cut from the long length coated conductors.

2.2.2 BAF$_2$ EX SITU YBCO COATINGS USING EVAPORATED PRECURSORS

YBCO films of variable thickness were deposited by simultaneous evaporation from electron-beam Y, BaF_2, and Cu sources on both RABiTS and IBAD templates. Composition control was achieved by quartz crystal monitors of the three individual evaporation rates. During the deposition, the substrates were slightly heated to ℑ100^{o}C. Small amounts of O_2 were dosed into the vacuum chamber to partially oxidize the deposit and minimize the reduction of substrate CeO_2 buffer layers. Ex situ conversion was performed in a standard tube furnace described in [57], equipped to operate with flowing gas mixtures at atmospheric pressure. Maximum temperatures during anneal reached 780^{o}C and the growth rate was about 0.1–1.2 nm/s for thickness values ranging from 0.2-2σm. The oxygen partial pressure was ranged between 0.01KPa and 0.1KPa and the water partial pressure (needed to decompose incorporated BaF_2 of the precursor layer) was kept below 0.7KPa [57].

The RABiTS architecture used for coatings with the BaF_2 process consist of a 50σm thick Ni-3%W metal tape (Ni-W) coated with a Ni overlayer (1.5σm), and Y_2O_3

(0.2σm), YSZ (0.15σm), CeO_2 (0.015σm) buffer layers. Additionally, YBCO films grown by the BaF_2 process on IBAD YSZ templates with a Hastelloy substrate coated with a CeO_2 buffer layer have also been analyzed. All these samples have been prepared at the Oak Ridge National Laboratory (USA) by Dr. Feenstra [58].

2.2.3 MICROSTRUCTURAL CHARACTERIZATION OF THE STUDIED SAMPLES

2.2.3.a STRUCTURAL GRANULARITY: EBSD

We have seen that due to its metallic textured substrate coated conductors are granular on a microscopic scale, such that predominantly low-angle grain boundaries exist. For a direct comparison of the YBCO films on IBAD and RABiTS substrates, the differences in grain sizes and GBs has to be taken into account.

The local texture information in a coated conductor can be obtained by Electron Backscattering Diffraction (EBSD) measurements which provide images of grain maps for the YBCO layer and also for the metallic substrates. EBSD patters are generated in a SEM system by illuminating highly tilted samples ($\Im 70^{o}$) with a stationary electron probe. Backscattered electrons that satisfy the Bragg law for a given plane emanate in diffraction cones from both the front and the back surface of the plane. A phosphor screen is used to intercept the diffraction cones which appear as pairs of parallel nearly straight lines (Kikuchi lines).

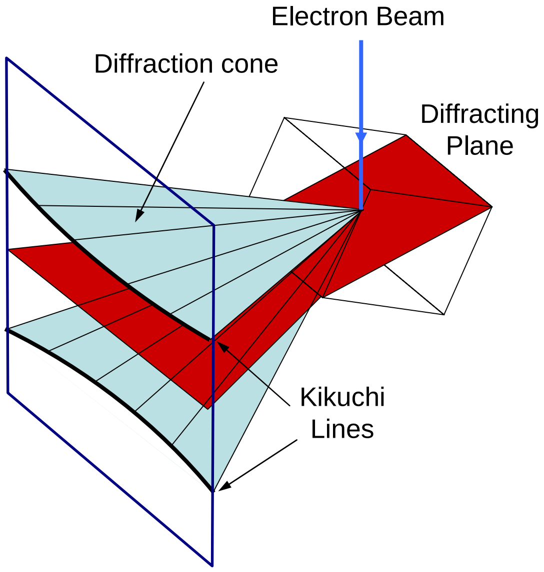

Fig. 2-2. Schematic representation of Kikuchi lines determination in a EBSD system

Orientation mapping using EBSD is accomplished by obtaining EBSD patterns at an array of points on a sample. At each pixel the EBSD pattern is collected and automatically indexed and the crystallographic orientation calculated. A map of the crystallographic orientation (texture) of the sample can then be formed.

Grains are defined as continuous set of points aligned within a certain misorientation degree. Orientations higher than a fixed threshold are represented by different colours. With this technique it has been observed [48,50] that the grain size in RABiTS coated conductors is determined by the grain size of the metallic substrate since in general the YBCO layer directly replicates the substrate metallic GBs. In Fig. 2-3 we present the EBSD data obtained one of the standard RABiTS sample analyzed. Fig. 2-3b and Fig. 2-3a are grain maps of the YBCO and underlying nickel substrate respectively. The same grain boundary network structure is clearly visible in both images. The typical grain size measured in a RABiTS coated conductor is 30 -100σm.

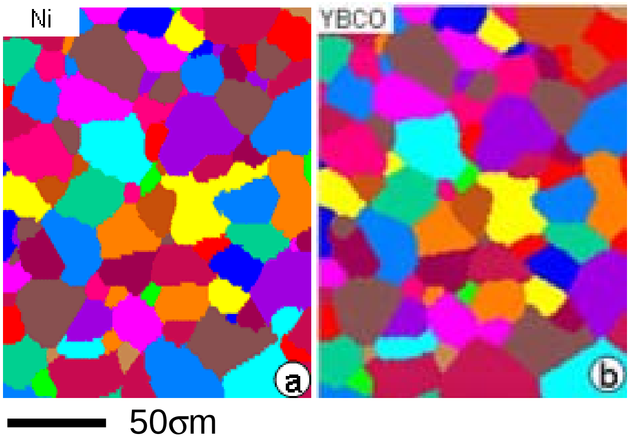

Fig. 2-3. EBSD maps of a nickel tape (a) and the YBCO layer grown on the same tape area (b). Different colours identify grains with points aligned within 1^{o}.

In IBAD coated conductors since the metallic substrate is polycrystalline, the grain size reflects the grain structure formed in the IBAD buffer layer grown on top of the metallic substrate. EBSD images of the GB network in IBAD coated conductors show the presence of small grains of about 0.5-5σm in these materials (Fig. 2-4). Thus, the average grain size is more than one order of magnitude smaller compared to RABiTS conductors.

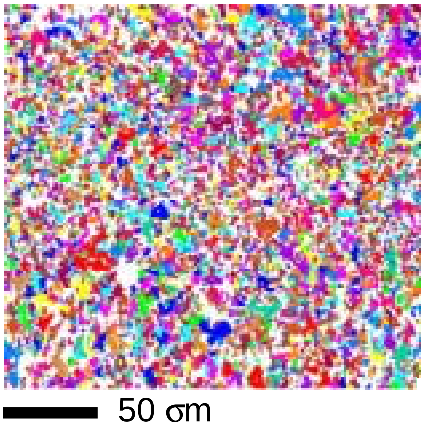

Fig. 2-4. Grain map produced by EBSD of a YBCO film grown on an IBAD-YSZ buffered substrate. Different colours identify grains with points aligned within 1^{o}.

2.2.3.b TEXTURE ANALYSIS: X-RAY DIFFRACTION

The simplest modelling of a network of GBs in YBCO CCs is just the assumption that the current density of each GB only depends on its individual misorientation angle and, thus the pattern of magnetic flux penetration and its critical current is simply determined by the average degree of biaxial alignment of the individual grains. The texture of CCs has been determined by means of X Ray Diffraction measurements performed at the microscopy services in the “Universitat de Barcelona”.

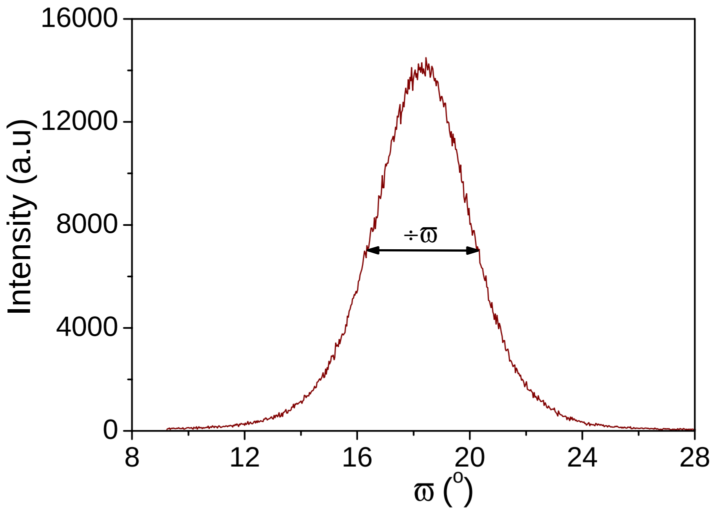

Fig. 2-5. Rocking curve measured for the sample, IBADt1.6a$_{Gott}$*, with the FWHM,* $\div\varpi=3.9^{o}$*, indicated.*

With the χ-2χ spectra it has been checked that only the peaks corresponding to the (00l) reflections for the YBCO are present, indicating that the YBCO layer is oriented with the c-axis perpendicular to the substrate. The different alignment of the grains for the out of plane texture, is characterized by the full width at half maximum (FWHM) of the rocking curve for the (005) peak, ÷ϖ. Fig. 2-5 shows an example of a rocking curve measured for an IBAD CC where ÷ϖ=3.9^{o}. The values of ÷ϖ obtained for coated conductors are quite higher than the typical values obtained for YBCO layers grown on single crystals (÷ϖℑ0.3^{o}-0.5^{o}) since in CCs, the YBCO is grown on top of a buffered metallic substrate which already presents a much higher out of plain misorientation than a single crystal.

The in-plane texture is characterized by measuring the average FWHM of the phi-scan for the (103) YBCO reflections, ÷λ. Fig. 2-6 shows the phi-scan measured for an IBAD sample (IBADt1$_{Gott}$) were ÷λ=6.5^{o}. Only four peaks, separated 90^{o}, are present, indicating the existence of one unique in-plane orientation of the grains. Once again the values of ÷λ are determined by the texture of the underneath buffer layers.

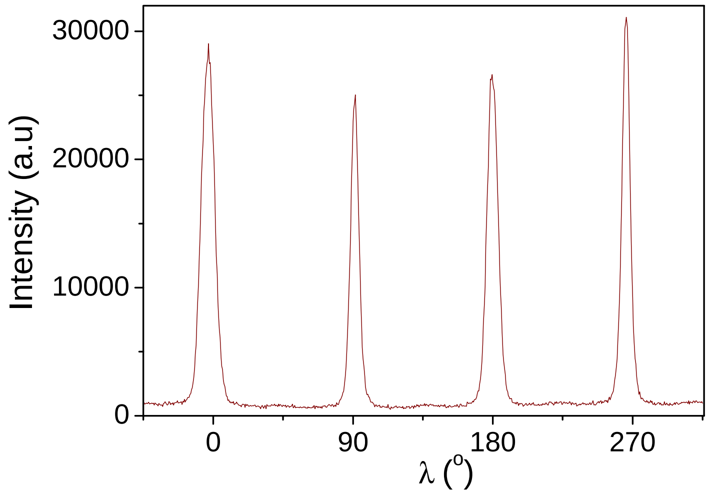

Fig. 2-6. Phi-scan measured for the sample IBADt1$_{Gott}$. The average FWHM of the four peaks gives ÷λ=6.5^{o}.

2.2.4 GENERAL DESCRIPTION OF THE STUDIED SAMPLES

Some of the relevant parameters determined for all the samples analyzed in this Thesis are presented in Table 2-1. We have named the different samples according the laboratory where they have been grown (Oak Ridge National Laboratory (USA), “Zentrum für FunktionWekstoffe” in Göttingen (Germany) and IFW in Dresden (Germany)) (see section2.2.1 and 2.2.2). Additionally we have included an extra sample grown by the company SCt0.2$_{THEVA}$ (Germany) which consist of a YBCO thin film grown on a STO single crystal by Thermal evaporation.

Sample name	*Grown process*	*t(um)*	*R (cm)*	*T_c(K)*	*<2a> (σm)*	*J_c^G (A/m^2)*	*J_c^{GB} (A/m^2)*	$\div\varpi(^o)$	$\div\lambda(^o)$
RABt0.20$_{ORNL-A}$	BaF$_2$-A	0.20	0.17		20	7.30.10^{10}	1.33.10^{10}		
RABt0.34$_{ORNL-A}$	BaF$_2$-A	0.34	0.18	91.8	46	7.29.10^{10}	9.47.10^{9}	5.6	6.5
RABt1.08$_{ORNL-A}$	BaF$_2$-A	1.08	0.19	91.2	60	2.58.10^{10}	6.10.10^{9}	5.3	6.3
RABt2.53$_{ORNL-A}$	BaF$_2$-A	2.53	0.2	92.2	70	1.11.10^{10}	3.40.10^{9}	7.56	9.51
RABt2.60$_{ORNL-A}$	BaF$_2$-A	2.60	0.18		100	1.22.10^{10}	3.61.10^{9}	6.6	8
RABt2.66$_{ORNL-A}$	BaF$_2$-A	2.66	0.21		70	1.05.10^{10}	4.28.10^{9}		
RABt0.18$_{ORNL-B}$	BaF$_2$-B	0.18	0.23		32	7.36.10^{10}	1.79.10^{10}	5.02	6.74
RABt0.34$_{ORNL-B}$	BaF$_2$-B	0.34	0.19		40	5.76.10^{10}	1.48.10^{10}	5.28	6.91
RABt0.49$_{ORNL-B}$	BaF$_2$-B	0.49	0.21		26	4.59.10^{10}	1.55.10^{10}	5.29	6.8
RABt0.63$_{ORNL-B}$	BaF$_2$-B	0.63	0.20		24	3.61.10^{10}	1.66.10^{10}	4.9	6.51
RABt1.01$_{ORNL-B}$	BaF$_2$-B	1.01	0.19		20	3.05.10^{10}	1.41.10^{10}	5.23	7.18
RABt1.32$_{ORNL-B}$	BaF$_2$-B	1.32	0.18		30	2.35.10^{10}	1.06.10^{10}	5.76	7.67
RABt2.53$_{ORNL-B}$	BaF$_2$-B	2.53	0.20		50	1.56.10^{10}	7.75.10^{9}	6.57	8.1
RAB.t1.37$_{ORNL-C}$	BaF$_2$-C	1.37	0.15	91.8	20	2.73.10^{10}	1.35.10^{10}	5.28	6.78
RABt1.41$_{ORNL-C}$	BaF$_2$-C	1.41	0.16	90.9	28	2.45.10^{10}	1.61.10^{10}		
RABt1.82$_{ORNL-C}$	BaF$_2$-C	1.82	0.16		32	2.22.10^{10}	1.22.10^{10}	6.4	7.24
IBADt2.90$_{ORNL-A}$	BaF$_2$-A	2.90	0.24						
IBADt1.33$_{ORNL-A}^{mill}$	BaF$_2$-A	1.33	0.24		70	2.33.10^{10}	6.76.10^{9}	5.17	8.74
IBADt1.13$_{ORNL-B}$	BaF$_2$-B	1.13	0.22		2	3.10.10^{10}	1.42.10^{10}	3.48	8.33
SCt0.27$_{ORNL-A}$	BaF$_2$-A	0.27	0.19	90.5		5.67.10^{10}			
SCt0.66$_{ORNL-A}$	BaF$_2$-A	0.66	0.22			3.15.10^{10}		0.76	0.68
IBADt0.23$_{Gott}$	PLD	0.23	0.26	88.8	0.6	4.79.10^{10}	1.40.10^{10}		7.8
IBADt1$_{Gott}$	PLD	1.00	0.25	90.8	2	3.06.10^{10}	1.27.10^{10}		6.5
IBADt1.2$_{Gott}$	PLD	1.20	0.24				6.49.10^{9}		6.3
IBADt1.6a$_{Gott}$	PLD	1.60	0.31	88.3	60	4.62.10^{9}	1.52.10^{9}		12.7
IBADt1.6b$_{Gott}$	PLD	1.60	0.27	88.6	1.2	3.56.10^{10}	7.94.10^{8}		17.2
SCt0.25$_{Gott}$	PLD	0.25	0.27	90.5		3.00.10^{10}			
BICt0.25-4^{o}$_{Gott}$	PLD	0.25							
SCt0.25-4^{o}$_{Gott}$	PLD	0.25	0.27	90.5		3.00.10^{10}			
RABt0.25$_{Dres}$	PLD	0.25	0.24		60	3.10.10^{10}	3.89.10^{9}		
RABt0.8$_{Dres}$	PLD	0.80	0.26	89.7	90	1.80.10^{10}	3.42.10^{9}		5.7
SCt0.2$_{Dres}$	PLD	0.20	0.27			2.95.10^{10}			
SCt0.2$_{THEVA}$	Th. Ev.	0.30	0.27	88.1		2.40.10^{10}			

Table 2-1. Description of the samples analyzed in this Thesis with several relevant sample parameters.

The radius of the sample, R, has been determined by considering a disk with the same surface than the sample surface, S, i.e. $S=\phi R^2$. The value that we obtain is similar to the sample radius determined magnetically by means of the initial susceptibility calculated for a thin disk in the Meissner state, $\theta_0=8R/3\phi t$, (section 3.3.1) which is the initial slope of the first magnetization curve [59].

The critical current density, T_c, has been determined by means of the ac-susceptibility curves, θ'(T) and θ''(T) as the onset temperature where the superconducting response vanishes and both $\theta'(T_c)=0$ and $\theta''(T_c)=0$ (see Fig. 2-7)

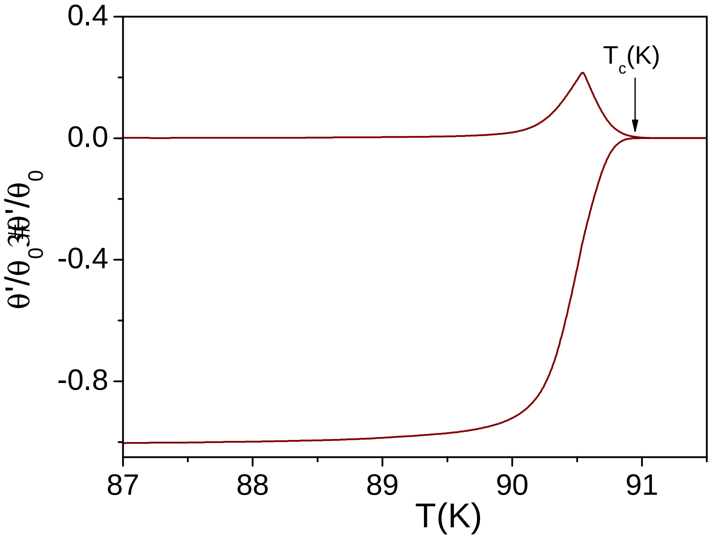

Fig. 2-7 Real, θ', and imaginary, θ'', parts of the complex susceptibility, normalized to $\theta_0=8R/3\phi d$*, as a function of temperature, measured for the sample* $IBADt1_{Gott}$ *at* $H_{ac}=0.01mT$ *and f=1111Hz.*

The values of grain size, <2a> grain critical density, J_c^G, and grain boundary critical current density, J_c^{GB}, have been calculated by means of magnetic hysteresis loops using a methodology developed during this Thesis and presented in Chapter 4.

CHAPTER 3

GENERAL THEORETICAL BACKGROUND OF MAGNETIC BEHAVIOUR OF SUPERCONDUCTING THIN FILMS

In general, due to the complexity of the microscopic description of the superconducting mixed, the magnetic response of type-II superconductors has been studied by means of approximations which describe the observed macroscopic behaviour. The most common approach is the critical-state model.

3.1 CRITICAL STATE MODEL

In the mixed state of pinned type II superconductors, the flux density decreases with increasing the distance from the surface due to the pinning of the vortices in the material defects when they penetrate into the superconductor from the surface. According to the Maxwell equation, the spatial distribution of the flux density, B, gives a transport current, J, determined by the equation 3-1.

$$\nabla \times \vec{B} = \mu_0 \vec{J} \qquad (3\text{-}1)$$

The critical state model assumes that the currents circulating in the superconductor flow with a density equal to the critical current density, J_c, that only depends upon the local magnetic field, $J_c(H_i)$. This model considers that the flux vortex array is stable, there is no flux creep, and that the lower critical field is zero. Although it can't explain the superconductivity phenomenon, it gives a good description of the magnetic behavior observed experimentally. Fig. 3-1 shows a schematic representation of the critical state in an infinite slab of size w.

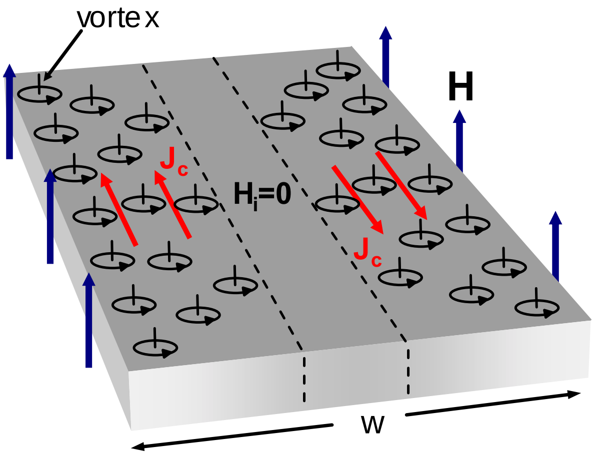

Fig. 3-1. Schematic representation of the critical state in an infinite slab of size w.

The gradient of flux inside the superconductor is subjected to the Lorentz force of the macroscopic currents induced, $\mathbf{F_L}$, (equation 3-2).

$$\vec{F}_L = \vec{J} x \vec{B} \qquad (3\text{-}2)$$

This force has to be compensated by the pinning force, $\mathbf{F_p}$, which holds the vortices pinned inside the superconductor. When the Lorentz force exceeds the pinning force the vortex motion occurs and the superconductor starts to dissipate. The critical current density will be given by the balance between these two forces.

$$\vec{F}_p = \vec{F}_L = \vec{J}_c x \vec{B} \qquad (3\text{-}3)$$

3.2 MAGNETIZATION HYSTERESIS LOOPS

3.2.1 INFINITE CYLINDER IN THE BEAN CRITICAL STATE MODEL

In the simplest critical state approach, the spatial variation of H or J_c is assumed to be constant inside the sample, and it is called Bean critical state model [60,61]. In a real case, J_c is dependent on B, and therefore J_c is not constant in the superconductor. However, it has been shown that the Bean model gives a fairly good approximation for the understanding of the magnetic behaviour of type II superconductors.

Fig. 3-2 shows the magnetization process of an infinite cylinder, increasing and decreasing the magnetic field, applied parallel to the cylinder axis, in the Bean critical state model. Different figures show the flux and current distribution inside the cylinder for several applied fields marked in the hysteresis loop curve (H^1, H* and 2H* increasing magnetic field and H*, H^1 and H=0 decreasing field). In the Bean model, J_c is considered to be constant, which means that the field gradient within the sample is constant and thus the magnetic field decreases linearly with the distance.

First, we will describe the hysteresis loop increasing the applied magnetic field. When we start to increase the field at the surface of the cylinder, vortices starts to penetrate inside the superconductor with a constant field slope, J_c (Fig. 3-2a). The field penetration distance, where supercurrents are induced, depends on the applied magnetic field, the sample dimension and the critical current density. The direction of superconducting currents is the one shown in the figure. The total magnetization can be determined from the area limited by the internal magnetic field profiles and the applied magnetic field (zone colored in gray). $M=H_i-H_a$. The magnetization is not uniform in the sample, and the measured M value shows the average for the total volume. In the flux free regions ($H_i=0$), where no flux gradients are present, one has J=0.

When the internal field reaches the centre of the sample, the applied magnetic field is named full penetration field, H* (Fig. 3-2b). For This particular value of the magnetic field, supercurrents are induced in the whole sample and the associated magnetization saturates, M^{sat}. For an infinite cylinder of radius, R, one has [62],

$$J_c \mid \frac{H^*}{R} \qquad 3\text{-}4$$

The full penetration field can also be determined from the hysteresis loop curve, $M(H_a)$, since it is the value of the applied magnetic field where the initial magnetization curve and the return curve after completing a saturated hysteresis loop merge (see hysteresis loop of Fig. 3-2). In order to obtain a saturated hysteresis loop it is necessary a maximum applied field of $H_m \varnothing 2H^*$, since the minimum value of H_m needed to saturate the remanent magnetization (magnitude of the magnetization when the applied field passes through zero, M^{rem}) is $H_m=2H^*$ (Fig. 3-2c). Later on the cases $H_m<2H^*$ and $H_m>2H^*$ will be analyzed.

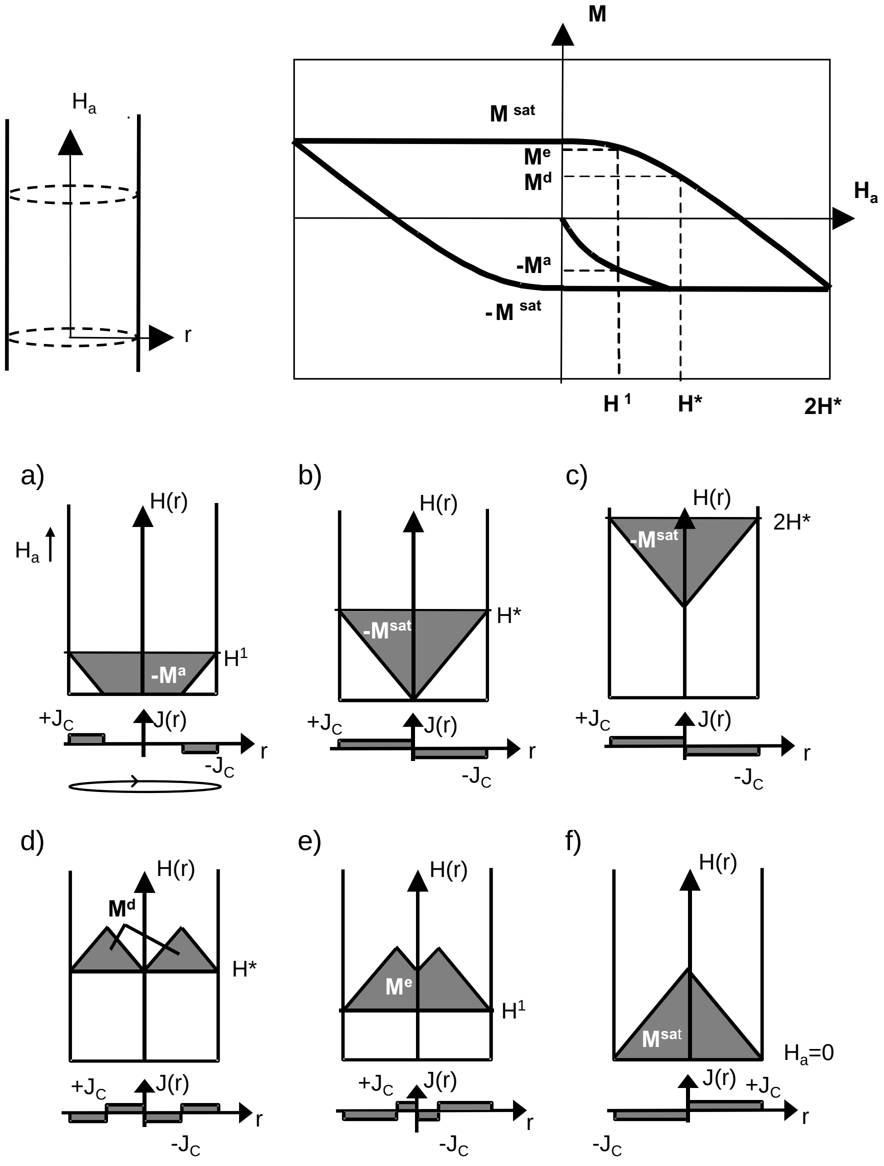

Fig. 3-2. Magnetization process of an infinite cylinder based on the Bean critical state model. Schematic illustration of Magnetic field and current distribution inside the sample increasing the magnetic field a) b) and c)and decreasing the magnetic field d) e) and f).

When the magnetic field is decreased, the supercurrents invert their direction from the superconductor surface (Fig. 3-2d). The current direction is determined by the slope of $H_i(r)$. At this point there is flux trapped inside the superconductor since the internal magnetic field is higher than the applied magnetic field and thus the magnetization is positive (M^d).

As the magnetic field is further decreased, the supercurrents flowing in opposite direction penetrate farther inside the sample and the positive magnetization increases. For $H_a=H^1$, the value of the magnetization, M^e, is almost saturated (Fig. 3-2e).

After a maximum applied field of 2H*, if the magnetic field is completely removed ($H_a=0$), all the supercurrents have changed their direction and the remanent magnetization in the sample is the saturated magnetization, $M^{rem}=M^{sat}$ (Fig. 3-2f).

Following the hysteresis loop, for negative values of the magnetic field, the critical state is formed in the opposite direction and an antisymmetrical hysteresis loop is described.

Fig. 3-3 shows three different hysteresis loops determined with the Bean critical state model for an infinite cylinder, with $H_m<2H^*$, $H_m=2H^*$ and $H_m>2H^*$, and schematic representation of the flux and current distribution inside the cylinder at the indicated positions.

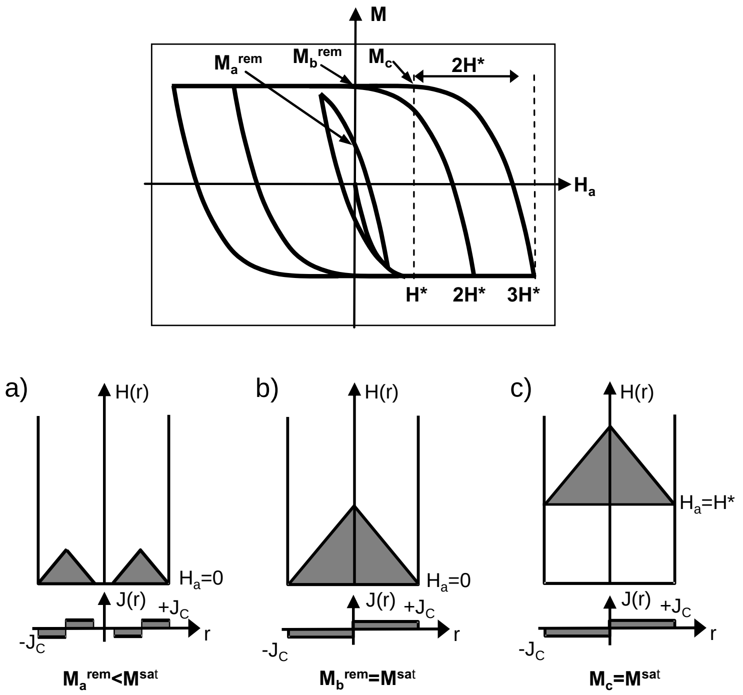

Fig. 3-3. Hysteresis loops determined with the Bean critical state model for an infinite cylinder with different maximum applied fields. Schematic illustration of the remanent magnetization in each case.

For the hysteresis loop with $H_m<2H^*$, the remanent magnetization, M_a^{rem}, is smaller than the saturation magnetization, $M_a^{rem}<M^{sat}$ (Fig. 3-3a). The maximum applied field needed in order to saturate the remanent magnetization is $H_m=2H^*$, in this case $M_b^{rem}=M^{sat}$ (Fig. 3-3b). For $H_m>2H^*$ the magnetization is already saturated at

H_a=H_m. So that, after applying a maximum field of H_m=3H* the magnetization will be saturated when the applied field is decreased until 3H*-2H*=H*, M_c=M^{rem} (Fig. 3-3c).

The critical current can be calculated by means of the hysteresis loop using the Bean critical state model. For an infinite cylinder, J_c is determined with equation 3-5 [62].

$$J_c \mid \frac{3\div M}{2R} \qquad 3\text{-}5$$

where ÷M is the width of the saturated hysteresis loop (for H_mÓ2H*), and R is the cylinder radius.

3.2.2 EFFECT OF DEMAGNETIZING FIELDS

The hysteresis loops described in the previous chapter are valid for infinite cylindrical samples. In the case of finite superconductors, the effects of demagnetizing fields have to be considered [18,59,62,63].

In an infinitely long superconducting cylinder, when a magnetic field is applied along the cylinder axis, supercurrents are induced along the lateral surface of the cylinder, creating a constant vertical current profile. In a finite sample, the penetration of the current inside the cylinder is affected by edge effects and thus, near the ends of the superconductor, currents penetrate deeper into the sample. Fig. 3-4 shows a schematic representation of the current profiles for an infinite sample (t/R=←) and two finite samples with t/R=10 and t/R=1 [62]. Where t is the length and R the radius of the cylinder.

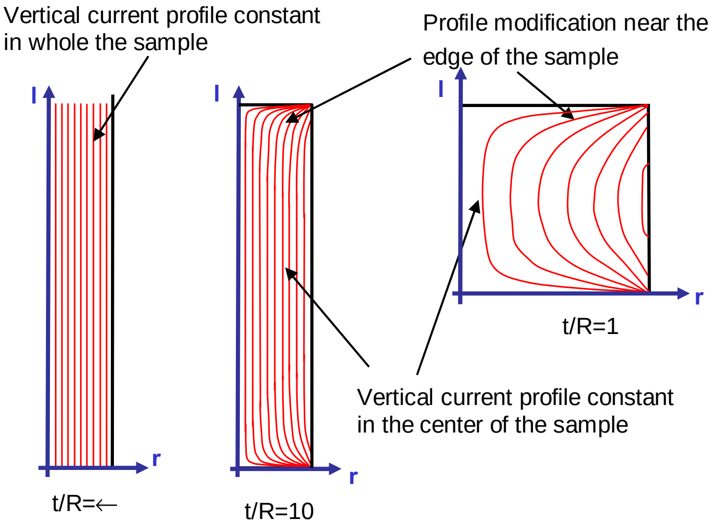

Fig. 3-4. Current profiles for three different cylinders. The axis of the cylinder is at the right of each figure. t is the length and R the radius of the cylinder [62].

The effect of sample size in the hysteresis loops is displayed in Fig. 3-5 [62]. The applied magnetic field is normalized to the value $H^*_{t/R=\leftarrow}=J_cR$, which corresponds to the full penetration field for an infinite cylinder, whereas the magnetization is normalized to the saturation magnetization in each case, M^{sat}. This normalization makes the results independent of the particular values of J_c and R. Notice that the first slopes in both the initial and reverse curves of the hysteresis loops become larger with decreasing t/R. Consequently, the saturation magnetization (achieved when the superconductor is fully penetrated) is reached at lower applied magnetic fields for shorter samples.

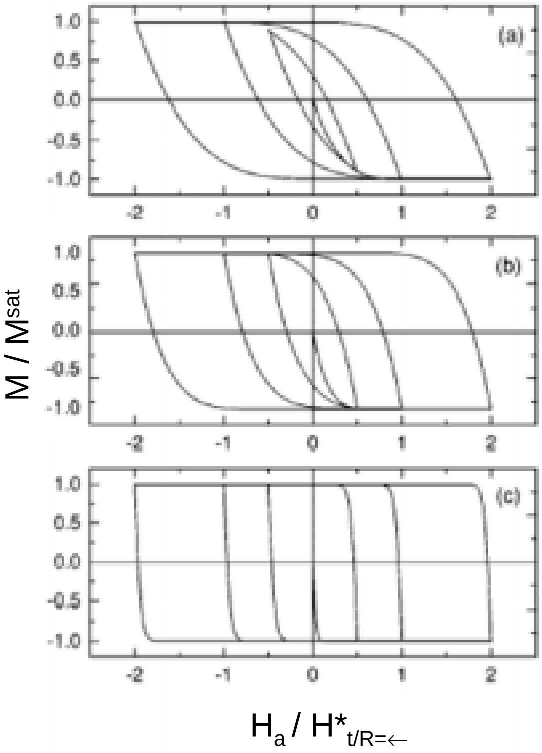

Fig. 3-5. Magnetization loops in the Bean critical state model for different maximum applied fields calculated for cylinders with t/R=10 (a), t/R=1(b) and t/R=0.1 (c) [62].

The current distribution in a finite sample creates a field that modifies the external field everywhere (not only in the interior region, as in the infinite case). Therefore, outside the superconductor, the magnetic field is no longer the applied magnetic field except in points far from the superconductor. The effect of the field produced by the first penetrated currents in the corners is to increase the field in some regions so that, the real field in the lateral surface of the cylinder is larger than the applied field. As result, the magnetization produced by such currents apparently corresponds to larger values of the applied field. Thus, the effect of this is to increase the slope of the initial $M(H_a)$ curve and in the same way, the first slope of the reverse curve. Moreover, the full penetration field, H*, decreases when the sample thickness decreases.

Since for finite samples, the applied magnetic field approach very slowly at H* when the sample is almost fully penetrated, an effective penetration field calculated from the maximum in the imaginary part of the ac-susceptibility has been considered (see section 3.3.1). Then, for thin films with 2R/t>100 one can use the equation 3-12 presented in section 3.3.1, and

$$H^* \,|\, \frac{1.94 J_c t}{2} \qquad \text{3-6}$$

The full penetration field calculated for cylinders different aspect ratios, t/R, has been presented in section 4.2.3.a.

Once the full penetration field is reached, as long as the applied field is not decreased, the magnetization has the saturation value $M^{sat}=J_cR/3$, independent of t/R. So that, the critical current density for any kind of cylindrical samples is given by equation 3-5.

3.2.3 EFFECT OF THE J_C DEPENDENCE WITH THE MAGNETIC FIELD

The Bean critical state model is a first approximation to describe the magnetic behaviour of type II superconductor, assuming constant J_c. In fact, in a real superconductor J_c depends on the local internal magnetic field at the current position, $J_c=J_c(H_i)$. Several approximations have been developed, each one based on a particular relationship between the internal field and the critical current density [18,62,64]. Particularly, Fig. 3-6 shows several magnetization loops obtained in the Bean critical state model (Fig. 3-6a) and assuming an exponential model with $J_c=J_{c0}\exp(-\sqrt{}H_i\sqrt{}/H_0)$, for different values of t/R (Fig. 3-6b) [62]. First notice that, the general effect of the demagnetizing fields is that the thinner sample has a larger first slope in both the initial and the reverse curves of the hysteresis loops (independently of the fact of considering J_c constant or dependent on the magnetic field).

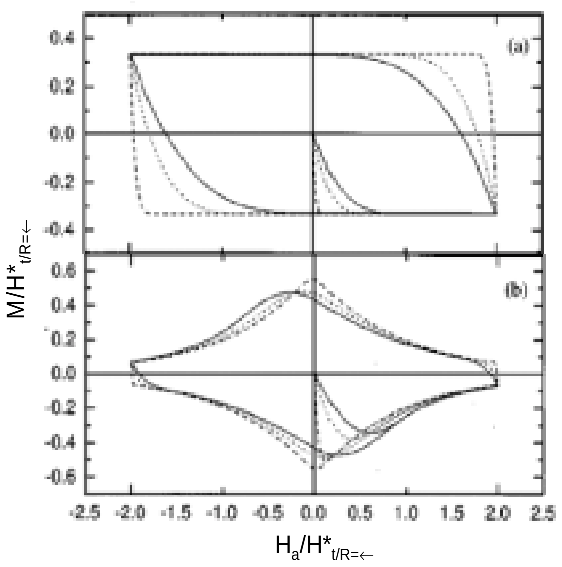

Fig. 3-6. Magnetization loops for a superconductor with J_c constant (a) and with an exponential dependence of $J_c(H_i)$ (b), for different values of t/R. The solid line corresponds to t/R=10, the dotted line to t/R=1, and the dashed line to t/R=0.1[62].

In the Bean critical state model (Fig. 3-6a), once the magnetization reaches the saturation, its value stays constant, even in a finite sample since the width of the loop is proportional to the constant value of J_c (equation 3-5). However, an important variation is observed for a non-constant J_c. When a certain dependence of $J_c(H_i)$ is considered, a peak appears in the reverse magnetization curve at $H_a<0$ for which an averaged value of the internal field inside the superconductor H_i is minimum (Fig. 3-6b) [62]. The general trend of the peak position is that it tends towards $H_a=0$ with decreasing the sample t/R ratio. This behaviour can be explained due to the fact of having large effect of demagnetizing fields in thin samples which induce almost constant field profiles for all the values of H_a in the reverse magnetization curve (Fig. 3-7b). Hence, the minimum average value of the internal field occurs at H_aℑ0. In contrast, for long samples a constant internal field profile in the reverse magnetization curve can only be considered for high applied fields (Fig. 3-7a) [65].

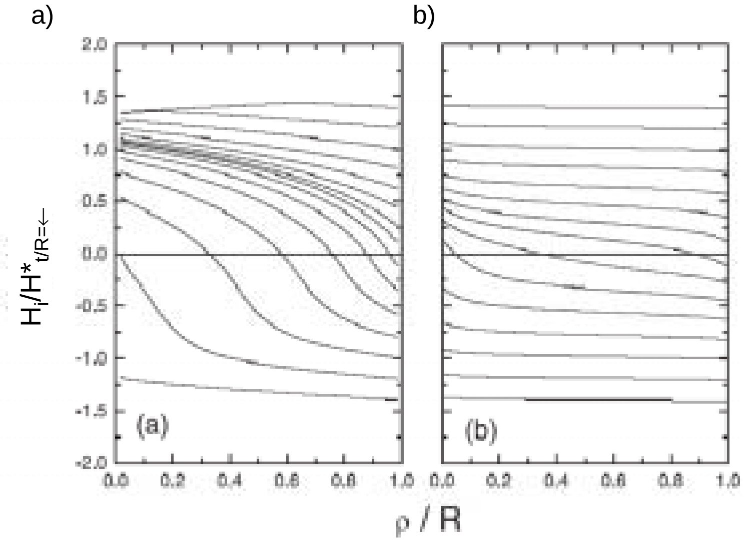

Fig. 3-7. Internal magnetic field profiles in the midplane of a superconducting cylinder calculated assuming an exponential dependence of $J_c=J_{c0}exp(-\surd H_i\surd/H_0)$. The different curves corresponds to the internal field, at different values of the applied field, H_a, in the reverse magnetization curve after a maximum applied field of $1.5H^*_{t/R=\leftarrow}$. It has been considered the case of a long sample, t/R=10 (a) and a thin disk, t/R=0.1 (b).

The critical current density $J_c(H_i)$ can be obtained from the width of the magnetization loop using the same equation as in the Bean critical state model (equation 3-5) but considering in this case the magnetization field dependence $M(H_a)$,

$$J_c(H)\,|\,\frac{3\div M(H)}{2R} \qquad 3\text{-}7$$

being ÷M the width of the saturated hysteresis loop at the applied magnetic field H. This formula is valid when the magnetization on ascending and descending branches of the hysteresis loop corresponds to fully penetrate states, and when the internal field is not very different from the applied one [66,67]. Since the field profiles in the case of thin samples are much more spatially uniform than in the case of long superconductors these samples are an optimum case for obtaining J_c from the width of the magnetizing loop. Actually, the value of the internal field for thin samples is basically equal to the external H_a value except within a narrow region around $H_a=0$ (see Fig. 3-7b).

The value of the full penetration field, H*, also varies when a certain dependence of critical current with the magnetic field is considered. For a given t/R, it is seen that H* increases when the dependence of J_c with the magnetic field increases [62]. However, due to the difficulty to introduce a certain field dependence of J_c in the determination of H*, for cylinders of different ratio, t/R, we have considered the equations derived in the Bean model (see section 4.1.2 and 4.2.3.a). As we will see in section 4.1.2 this assumption will not strongly affect the values of J_c that we obtain.

3.3 COMPLEX AC-SUSCEPTIBILITY

The hysteretic dependence of the magnetization M when the applied field, H_a, is cycled leads to ac losses. According to the critical state model, the losses are given by the area of the magnetic hysteresis loop. Usually, the ac response is expressed through the imaginary and real parts of the so-called nonlinear magnetic susceptibility [59,68]. If the applied magnetic field is oscillated harmonically with amplitude, H_{ac}, and a frequency f=ϖ/2ϕ.

$$H_a \mid H_{ac}\cos(\varpi t) \tag{3-8}$$

the complex ac-susceptibility components are defined as,

$$\theta' \mid \frac{\varpi}{\phi H_{ac}} \int_0^T M(t)\cos(\varpi t)d(t) \tag{3-9}$$

$$\theta'' \mid \frac{\varpi}{\phi H_{ac}} \int_0^T M(t)\sin(\varpi t)d(t) \tag{3-10}$$

The real component of the ac-susceptibility, θ’, is a direct measure of flux penetration into the sample, while the imaginary component, θ’’, takes into account the hysteretic losses due to this flux penetration.

3.3.1 BEAN CRITICAL STATE MODEL: CRITICAL CURRENT DENSITY DETERMINATION

Fig. 3-8 shows plots of both θ’ and θ’’ versus the ac applied magnetic field, calculated in the Bean critical state model, for a superconducting thin disk of thickness t, radius R (t<<R). The value H_{ac} has been normalized to $H_d=J_ct/2$, which is a characteristic field for thin film geometry, while the values of θ’ and θ’’ have been normalized to the initial susceptibility for a thin disk in the Meissner state, $\theta_0=8R/3\phi t$ [59]. With these normalization the real component of the ac-susceptibility, θ'/θ_0, at low magnetic field amplitudes, H_{ac}, where no flux penetration exists, is equal to $\theta'/\theta_0=-1$ and the imaginary component, associated to the hysteretic loses is equal to $\theta''/\theta_0=0$. Notice that the response θ’’ shows a maximum as a function of the field amplitude. Such a maximum is in fact a common feature in all geometries. In the Bean model for a long cylinder the peak is known to occur when H_{ac} is equal to the full penetration field. In the thin film geometry the interpretation of the peak position is not so simple. Even in the Bean model for a thin disk only numerical values are available: the peak in θ’’

occurs at H_{ac}/H_d=1.94 and $\theta''=\theta''_{peak}=0.24\theta_0$ [59]. The values of θ''_{peak} for cylinders of different aspect ratio, 2R/t, have been calculated theoretically by A. Sánchez et al. owing to our collaboration with the “Universistat Autònoma de Barcelona” (see section 6.2.1).

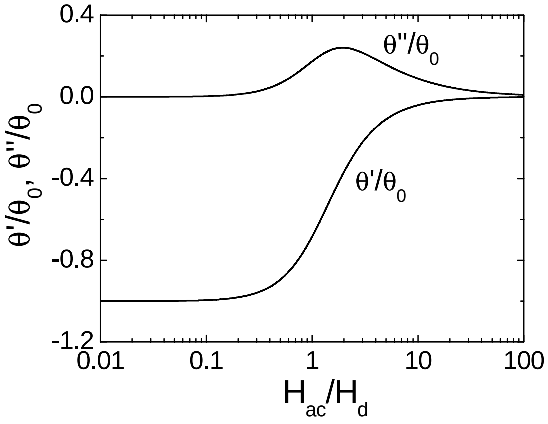

Fig. 3-8. Real, θ', and imaginary, θ'', parts of the complex susceptibility, normalized to $\theta_0=8R/3\phi d$, as a function of H_{ac}/H_d, for a thin film cylinder in the Bean critical state.

One of the fundamental physical quantities that can be extracted from ac-susceptibility measurements is the critical current density, J_c. Measuring several sets of θ''(T) curves, at different ac field amplitudes, H_{ac}, it is possible to find the dependence of $J_c(T)$. Since for a long cylinder the peak of θ''(T) occurs when the applied ac magnetic field, H_{ac}, is equal to the full penetration field. From equation 3-4, $J_c=H^*/R$, we have,

$$J_c(T_{peak}) \approx H_{ac}/R \qquad (2R/t \ll 0.1) \tag{3-11}$$

In the thin film approximation, since for a thin disk (2R/t>100), θ'' occurs at H_{ac}/H_d=1.94 with $H_d=J_ct/2$,

$$J_c(T_{peak}) \approx 2H_{ac}/1.94t \qquad (2R/t \gg 100) \tag{3-12}$$

3.3.2 PLOTS OF θ'' VERSUS θ'

In contrast to graphs of θ as a function of the field amplitude or temperature, a plot of θ'' versus θ' contains only dimensionless quantities, and is therefore a very useful scenario for analyzing experimental data [18,69,70]. In practice, such a parametric plot θ''(θ') can be obtained by scans either over ac the magnetic field amplitude or over the temperature. Fig. 3-9 shows the parametric plot of the complex susceptibility for a thin disk in the Bean critical state model. The Bean model predicts a peak located at θ'_{max}/θ_0 =-0.38 with θ''_{max}/θ_0 =0.24 in the case of thin superconducting disks.

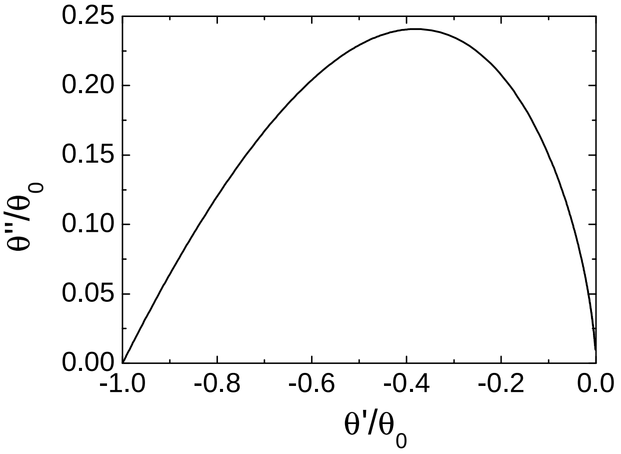

Fig. 3-9. Parametric θ''(θ') plot for a thin disk in the Bean critical state model.

If a certain dependence of the critical current with the magnetic field is considered, the θ''(θ') curve is modified increasing the magnitude θ''_{max} and shifting the peak towards θ'=0 (Fig. 3-10). Meanwhile, at small H_{ac} or T, as θ'⇓ -1, the slope of θ''(θ') curve remains the same as in the Bean model. If vortex dynamics is affected by flux creep (see section 1.3.2), the maximum of θ'', θ''_{max}, also increases but now the peak shifts towards θ'=-1. Moreover the slope at θ'⇓ -1 becomes steeper (Fig. 3-10). The creep situation is therefore in strong contrast to the effect of having a field dependent J_c in the critical state model. Consequently, an analysis of that θ''(θ') plot allows us to discriminate between a pure critical state model behaviour and one where flux creep is an important ingredient [70].

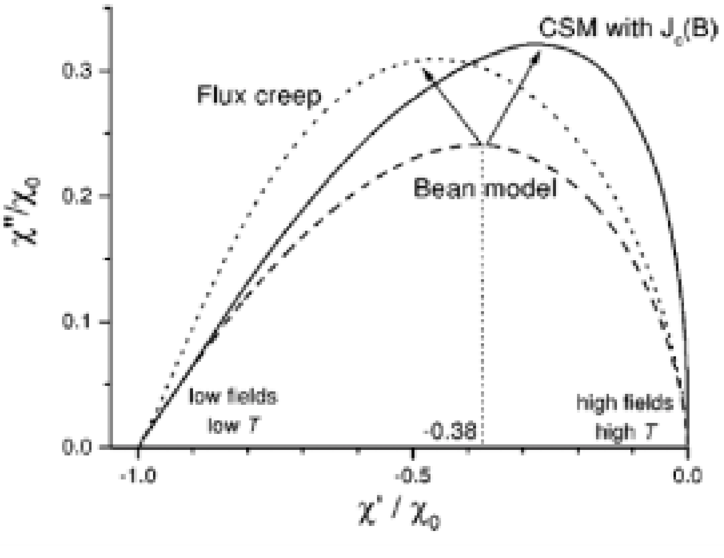

Fig. 3-10. Behavior of θ''(θ') for various models. Bean model (dashed line), critical state model (CSM) with $J_c(H)$ (solid line), and flux creep (dotted line) [70].

3.3.3 IDENTIFICATION OF THE DIFFERENT REGIMES IN THE AC-SUSCEPTIBILITY

In ac measurements, by varying the amplitude of the ac field, in an already FC sample with a certain H_{dc}, we are able to cover different flux dynamic regimes [17,68,69,71,72].

At the lowest amplitudes it is found a linear response, characterized by θ' independent of H_{ac}, with a low dissipation. In this region, where, $J<J_c(T,B)$, two different mechanisms may be responsible for the ac response of the superconductor. At high temperatures, an ohmic response with a real resistivity exist, where flux motion occurs due to thermally activated flux flow, TAFF. At low temperatures the ac response is dominated by the oscillations of vortices inside their potential wells (Campbell regime [73], in this case, the ac penetration depth can be written as;

$$\partial_c \mid \sqrt{\frac{Br_p}{\mu_0 J_c(T,B)}} \qquad \text{3-13}$$

Where $r_p \Im \bullet_{ab}(T)$ is the potential well range, thus, no frequency dependence of the ac signal is expected in this regime.

The crossover from linear to nonlinear response, $H_{ac}^{l}(T)$, marks the beginning of H_{ac} dependence of θ'. At large enough H_{ac}, vortex displacements will be much larger than the defect size (and even than the average defect distance), and eventually intervalley motion will dominate over most of the sample. In this case a critical state develops. In between the linear regime, at low ac fields, and the critical state regime, a large nonlinear transition region is observed.

At high enough amplitudes, a new crossover to a linear regime occurs, the ohmic flux flow regime, FF. This regime should take place when the Bean penetration length, $\Theta_c=H_{ac}/J_c(T)$ (see equation 3-14), becomes longer than the characteristic flux flow penetration length, given by the skin penetration depth, $\iota_{ff} \Im (\psi_{ff}/f)^{1/2}$, where, ψ_{ff} is the flux flow resistivity. Fig. 3-11 shows a schematic representation of the dynamic phase diagram in the plane (H_{ac}, T) expected for a high T_c superconductor, where we have identified the different dynamic regimes described above.

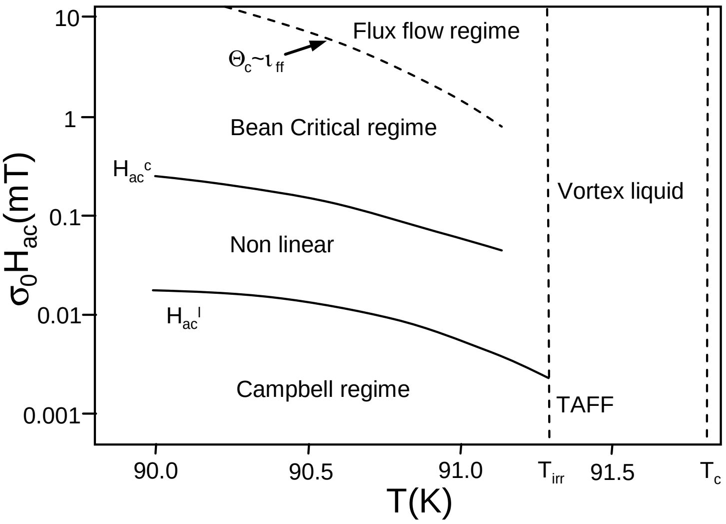

Fig. 3-11. Schematic representation of the dynamic phase diagram in the (H_{ac}, T) plane for a high T_c superconductor.

The onset of nonlinear response, defined with H_{ac}^{l}, can be determined directly from the $\theta'(H_{ac})$ curves measured at different temperatures, as the value of H_{ac} where θ' departs from the linear constant response (see Fig. 3-12). However, the definition of the lower boundary for the critical state regime, H_{ac}^{c}, also indicated in Fig. 3-12, is much more difficult to determine. To do that, we can apply a method developed by G. Pasquini et al. [69] which uses the $\theta'(T,H_{ac})$ data.

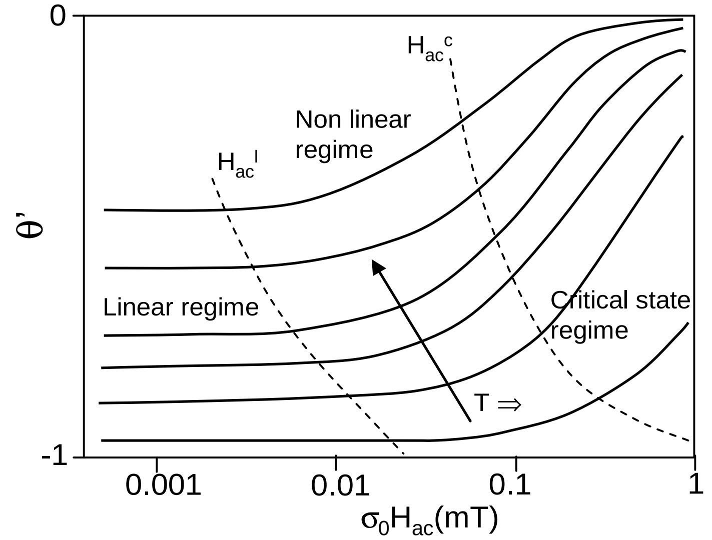

Fig. 3-12. schematic representation of the θ' component of the ac-susceptibility for various temperatures as a function of the ac field. Dashed lines indicate the onset of nonlinear response, H_{ac}^{l}, and the beginning of the critical state regime, H_{ac}^{c}.

The basic concept of the Bean model is that in any region of the sample, where intervalley vortex motion occurs, the persistent current density is uniform, as determined by the balance between Lorentz and pinning forces (see section 3.1). This determines a characteristic Bean length.

$$\Theta_c(T, H_{ac}) \mid \frac{H_{ac}}{J(T)} \qquad 3\text{-}14$$

However, due to creep effects, the current density is smaller than J_c and depends on the frequency of the measurement [7,74]. For this reason, the analysis must be performed at fixed frequency. The characteristic Bean length, Θ_c, is a function of the shielding component, θ', which only depends on the sample shape and dimension. According to the model developed by [69], this function can be determined by identifying θ' data at different T and H_{ac} that combine to produce the same Θ_c, according to equation 3-14. As a starting point, one takes two curves $\sigma'(T)=(1+\theta'(T))$ at fields H_{ac}^1 and H_{ac}^2, that we presume are in the critical regime, as shown in the inset of Fig. 3-13 and then trace a horizontal line that intersects the curves in points A and B. As σ' is the same in both points, so $\Theta_c^A=\Theta_c^B$, one can write $\sigma'_A=\sigma'_B=\sigma'(\Theta_c^A)$. We now trace a vertical line from B that intersects the curve for H_{ac}^1 in C. As B and C are at the same temperature then, provided that the Bean model applies, the persistent current density J(T) is the same in both cases, thus $\Theta_c^C/\Theta_c^B=H_{ac}^1/H_{ac}^2$, implying that $\sigma'_C=\sigma'(\nu\Theta_c^A)$, where $\nu= H_{ac}^1/H_{ac}^2$. Tracing a horizontal line through C that intersects the curve for H_{ac}^2 in D, one have $\sigma'_D=\sigma'_C$, and a vertical line through D that intersects the curve for H_{ac}^1 in E would imply that $\sigma'_E=\sigma'(\nu^2\Theta_c^A)$. Repeating this procedure moving through the curves one can obtain the function σ' evaluated at a set of Θ_c values equally spaced in logarithmic scale $\nu^n\Theta_c^A$ where n is an integer. Fig. 3-13 shows the curve $\Theta_c(\sigma')$, obtained for an irradiated YBCO single crystal in [69].

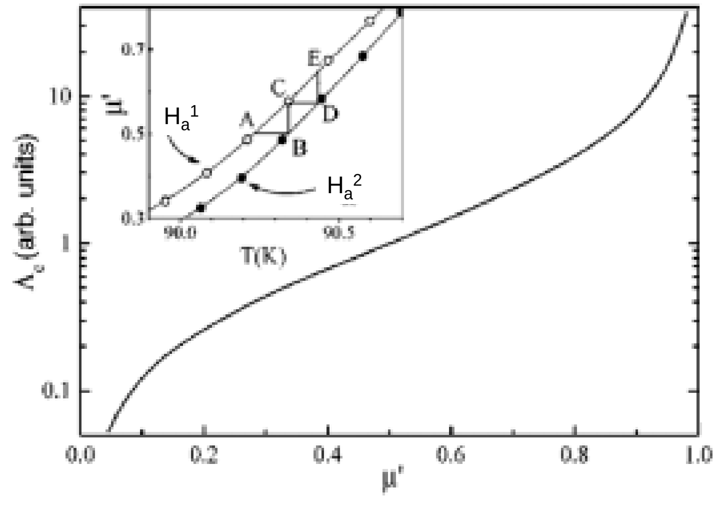

Fig. 3-13. Bean length, Θ_c, as a function of $\sigma'=1+\theta'$ obtained through the method described in [69] and sketched in the inset.

Once we have determined the curve $\Theta_c(\sigma')$, one can take values of σ' from several curves obtained at different H_{ac} at a fixed temperature and determine the value of Θ_c for each H_{ac}. Fig. 3-14 shows the result of such analysis performed by Pasquini et al. [69] to an irradiated YBCO single crystal, at several temperatures. If Θ_c is proportional to H_{ac}, then from equation 3-14 one can conclude that J_c is independent of H_{ac}, as occurs in the Bean critical state. In all cases we observe that $\Theta_c \nabla H_{ac}$ at high amplitudes, thus proving the existence of a Bean regime. At low amplitudes, there is a systematic deviation from a straight line and Θ_c becomes larger than the expected in the Bean regime, indicating the absence of a fully developed critical state regime. The arrows mark the lower boundary of the critical state regime, $H_{ac}^c(T)$. At very low H_{ac}, a plateau of Θ_c is expected which would indicate the region where the linear regime is attained.

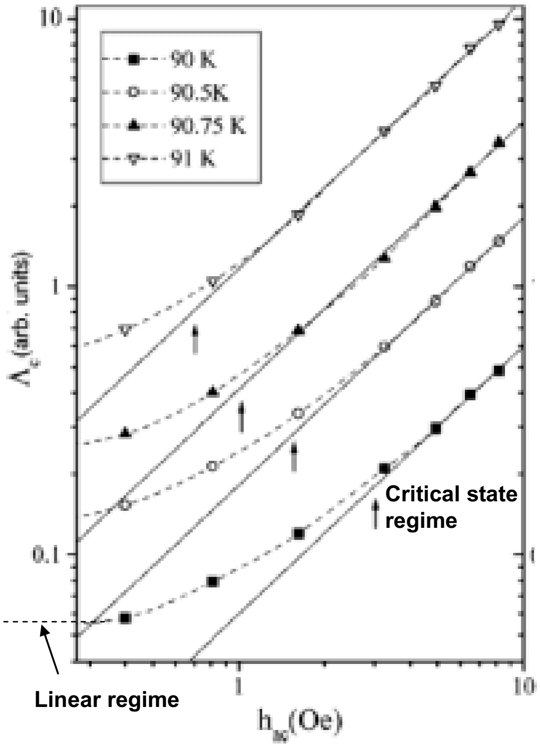

Fig. 3-14. Test to prove the existence of a critical regime, i.e., the consistence of the function $\Theta_c(\sigma')$, for several temperatures. Θ_c is proportional to H_{ac} above $H_{ac}^c(T)$ indicated with arrows [69]. Notice that this plot is in c.g.s. units.

We have seen then, that we are able to determine the dynamic phase diagram of a high T_c superconductor, by means of ac-susceptibility measurements performed at different H_{ac} and temperatures.

3.4 FLUX AND CURRENT DISTRIBUTION APPLIED TO LOW ANGLE GRAIN BOUNDARY SUPERCONDUCTORS

3.4.1 FLUX AND CURRENT DISTRIBUTION IN THIN FILMS

It has been described in section 3.1 that when the magnetic field at the surface of a type II superconductor exceeds H_{c1}, magnetic flux lines enter into the sample from all surfaces. Pinning at material defects leads to the generation of magnetic flux gradients towards all superconductor surfaces. Whereas, in fact the development of the critical state during flux penetration is a full three dimensional problem, only the flux penetration from a surface which is oriented parallel to the applied external field is considered in the original Bean critical state model [61] (see Fig. 3-15a). For thin superconductors in a perpendicular external magnetic field, the edge effects strongly change the field distribution assumed in the original Bean model and cause a curvature of the field lines (see Fig. 3-15b) [59].

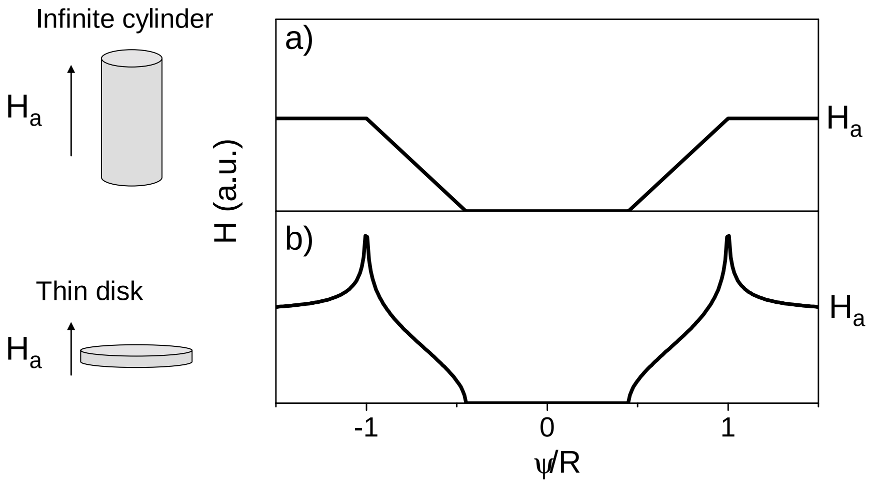

Fig. 3-15. Profiles of the axial magnetic field determined at the central plane, for an infinite cylinder (a) and for a thin disk (b) both of radius R, at an applied magnetic field H_a.

Particularly, in the remanent state (H_a=0), for a finite sample, the flux lines that have penetrated inside the superconductor and which are not longer supported by the external field, have to close through the edges of the sample resulting in a reverse flux component at the edge of the superconductor. Fig. 3-16a) shows a schematic illustration of the magnetic flux lines in a finite cylindrical superconductor and Fig. 3-16b) shows the surface field profiles calculated by A. Sanchez et al, assuming the Bean critical state model, for several cylindrical samples with different R/t [75]. Notice that the return flux that appears at the edge of the sample becomes more important when reducing the sample thickness (high R/t values) since the demagnetizing effects are then stronger.

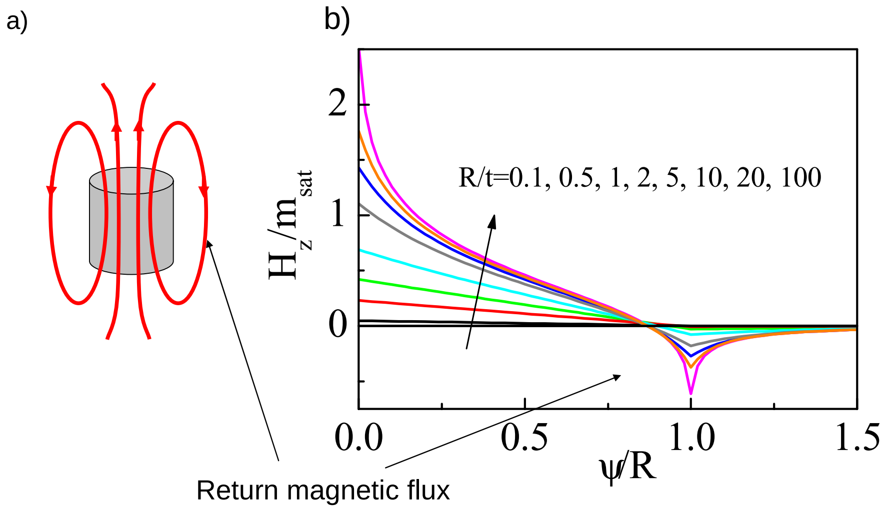

Fig. 3-16. Schematic illustration of the magnetic flux lines in the remanent state for a finite cylindrical superconductor (a). Surface axial field profiles at the remanent state, normalized to the saturated magnetic moment, determined at the central plane of several cylinders with different R/t (b).

In the case of infinite samples, where no demagnetizing fields have to be considered, the current distribution inside the sample can be easily constructed. Fig. 3-17 shows the planar current stream lines in the critical state for an infinite type-II superconductor with a) circular and b) square shape.

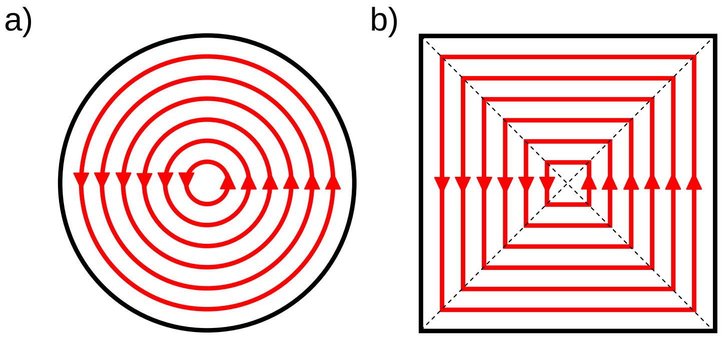

Fig. 3-17. Current stream lines calculated for an infinite specimen of cylindrical shape (a) and square shape (b) in the critical state model.

The currents flow parallel to the sample edge. In the case of square shaped sample the current stream lines have sharp bends. The current distribution shows a pattern of current domains of uniform parallel current flow which are separated by current domain boundaries. In the framework of the Bean model, the bending of the current is discontinuous and thus the size of current domain boundaries becomes infinitesimal small. In this case they form the so called discontinuity lines (dashed line in Fig. 3-17b). One distinguishes two types of d lines [56]: At d^+ lines the orientation of $\mathbf{J_c}$ changes discontinuously but the magnitude of J_c remains the same. At d^- lines the magnitude of J_c changes. The dashed lines shown in Fig. 3-17b are d^+ lines.

In the case of finite samples one has to consider edge effects in the field profiles (see Fig. 3-4). However, it has been observed that for thin film samples the planar current distribution determined from Magneto Optical measurements is similar to that obtained for an ideal infinite sample in almost all surface although one has to consider that the current stream lines at the edge of the sample are affected for the demagnetizing effects (Fig. 3-18) [56].

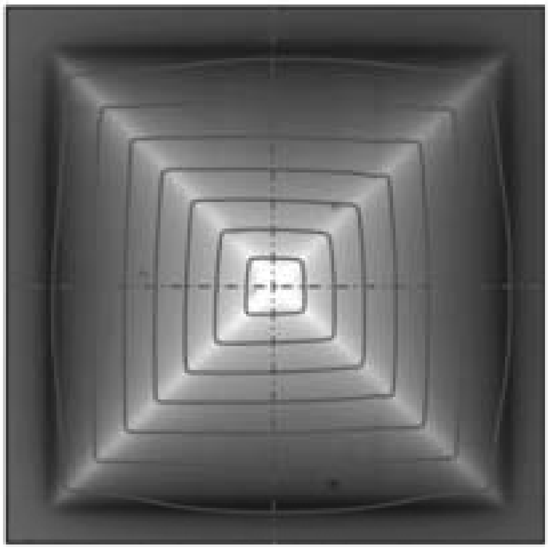

Fig. 3-18. Measured flux distribution of a square-shaped YBCO thin film in the remanent state and the corresponding planar current density distribution determined by applying the Biot-Savart law [56].

3.4.2 FLUX AND CURRENT DISTRIBUTION IN A LOW ANGLE GRAIN BOUNDARY

The flux penetration into a bicrystaline film starts in the region with lower critical current which is at the grain boundary. In the case of high angle grain boundaries (HAGB) with very low critical current density, the complete penetration of the GB occurs while no flux has penetrated the adjacent grains. The resulting flux density distribution is qualitatively indistinguishable from that of two totally separated superconductors, indicating that the GB critical current density is very small. In contrast, the low angle grain boundary (LAGB) is in partly penetrated state; though, the penetration depth of the flux along the GB is much larger than in the grains.

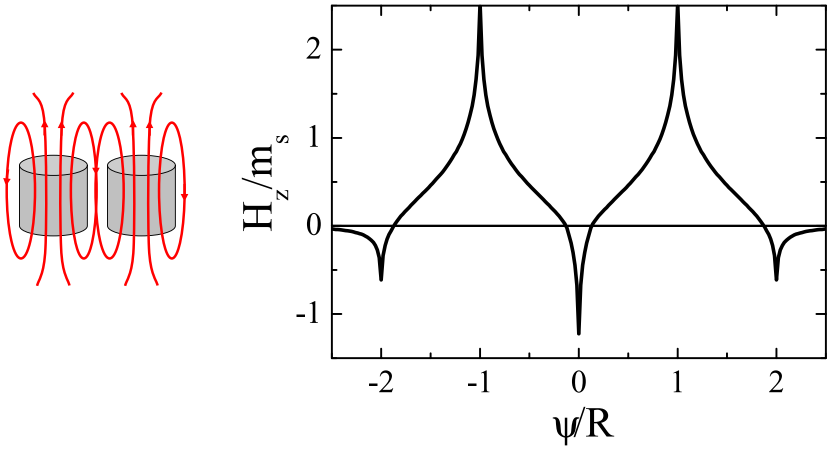

Fig. 3-19. Field profile across a grain boundary (ψ/R=0) at the remanent state determined from two cylindrical grains of R/t=100

When after a maximum applied magnetic field one starts to decrease the external field, the magnetic flux first starts to move out of the sample through the GB. In contrast to single crystalline thin films (Fig. 3-16), the area of reversed flux gradients not only return through the sample edges but also through the grain boundary. Consequently, at the remanent state, a negative flux is present at the GB besides the one that appears at the sample edges. The field profile at the GB can be determined considering the return field at the edge of two cylindrical grains with a certain dimension R/t (Fig. 3-19).

In the framework of Bean critical state model with a constant grain critical current density, J_c^G, and constant GB critical current density, $J_c^{GB} < J_c^G$, a model for the current pattern near the grain boundary can be given for the planar currents [55,56]. A schematic representation of the current pattern for $J_c^{GB}/J_c^G=0.5$ is shown in Fig. 3-20. Typically there is a three fold bending of current stream lines around the GB, outside the GB two d^+ lines are formed at an angle ζ to the GB. An additional bending occurs at the GB itself. Here as well the orientation and the magnitude of J_c changing and thus GB line can be considered to consist of two parallel d^- lines in the limit of vanishing distance. The angle ζ of the d^+ line is given by

$$\zeta = \frac{1}{2}\, ar\cos\left(\frac{J_c^{GB}}{J_c^{G}}\right) \tag{3-15}$$

Dashed lines with arrows indicate the direction of magnetic flux motion during the flux penetration. Flux line motion is perpendicular to the current stream lines (Lorentz force).

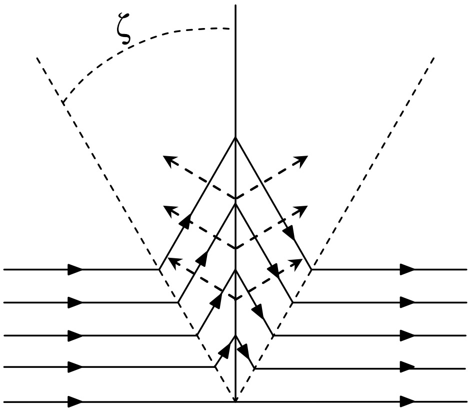

Fig. 3-20. Sketch of the current pattern at a grain boundary for a ratio $J_c^{GB}/J_c^{G}=0.5$*, assuming the Bean model.* ζ *is the angle of the* d^+ *line with respect to the GB according to equation 3-15.*

For $J_c^{GB}=0$, equation 3-15 gives the well known result $\zeta=45^o$ of the isotropic Bean model for a rectangular sample edge (section3.4.1).

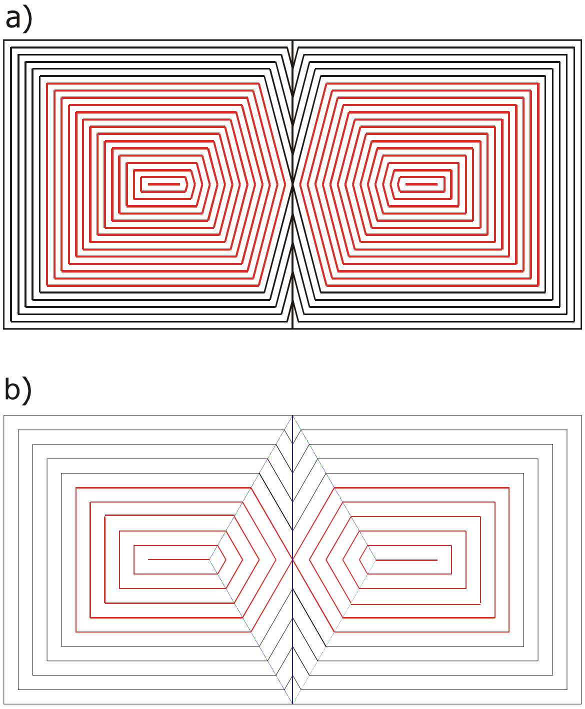

Fig. 3-21. Current stream lines calculated for two rectangular bicrystals with $J_c^{GB}/J_c^{G}=0.25$ *(a) and* $J_c^{GB}/J_c^{G}=0.5$ *(b), in the critical state model.*

Fig. 3-21 shows the planar current stream lines determined according to this model for two rectangular bicrystals with $J_c^{GB}/J_c^{G}=0.25$ and 0.5. For simplicity we have considered the current patterns that one would obtain without demagnetization effects. Notice that the current penetration through the grain boundary is faster than the penetration inside the grains since the lower grain boundary critical current. When the stream current lines reach the centre of the sample through the grain boundary, closed current loops are formed inside the grains which penetrate according to the grain critical current. Both critical sates formed by these closed loops will define the two magnetic grains present in the bycristal (red lines of Fig. 3-21). As the ratio J_c^{GB}/J_c^{G} decreases the penetration of current lines through the grain boundary occurs faster and thus the magnetic grain size becomes larger in comparison with the structural grain size. Additionally in this configuration, mutual inductance effects will be present which are beyond the studies performed in this thesis.

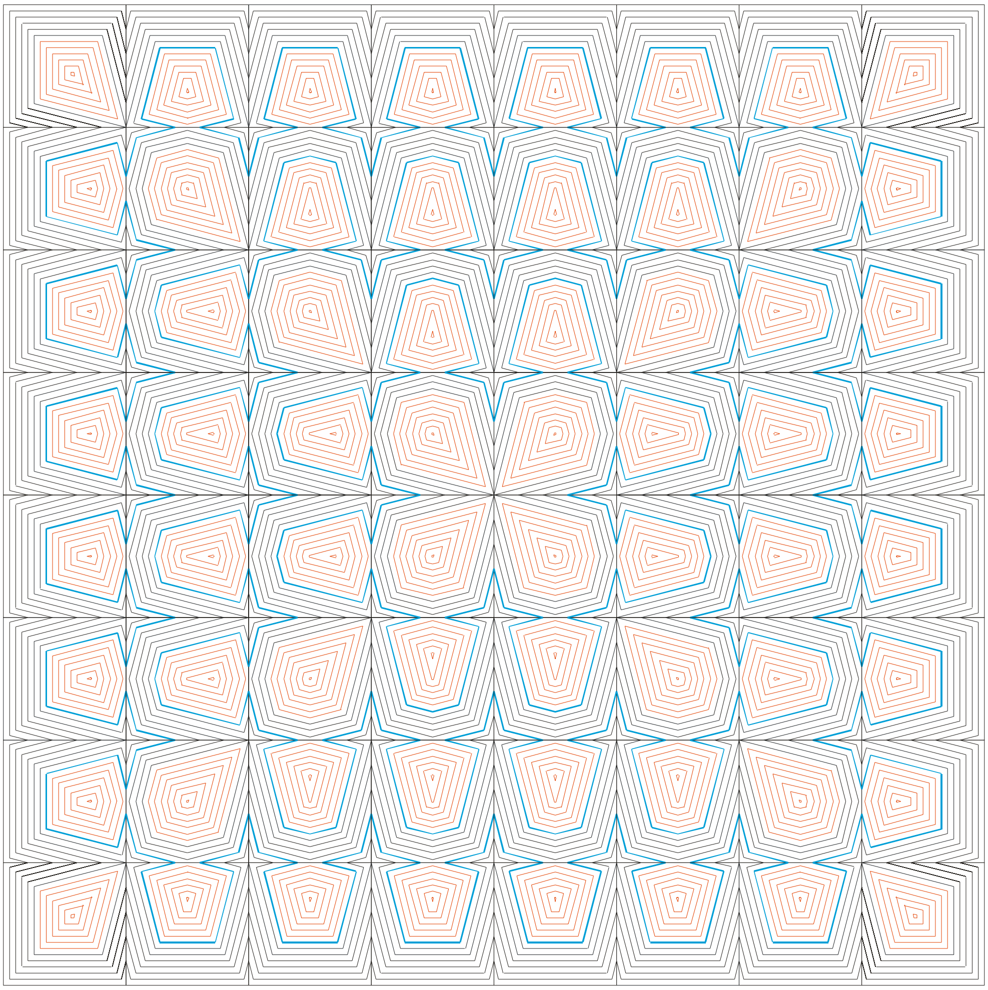

Fig. 3-22. Current stream lines calculated for a polycrystalline sample of 64 identical square grains with J_c^{GB}/J_c^{G}=0.25.

In order to estimate planar distribution of current lines in coated conductors we have applied the same model at a polycrystalline sample with several grains. Fig. 3-22 shows the current distribution that one would obtain for a polycrystalline sample with 64 square grains with identical low angle grain boundaries of J_c^{GB}/J_c^{G}=0.25 (misorientation angle $\Im 5^{o}$). Where again, we have considered no influence of the demagnetizing fields. This is the ideal case that would describe a very homogeneous coated conductor.

Closed loops which define the magnetic grains, represented in red, are clearly visible. The percolative grain boundary critical current density is shown in black. Notice that a general critical state is formed since currents flowing across the grain boundaries penetrates through all the sample until reaching the sample centre.

CHAPTER 4

MAGNETIC STUDY OF NON-GRANULAR YBCO THIN FILMS AND COATED CONDUCTORS.

In this chapter we present a complete analysis of the magnetic hysteresis loops measured for non-granular YBCO thin films and coated conductors. Comparing the results obtained for both systems we will be able to analyze the effect that, inherent granularity present coated conductors, produce to the features of magnetic hysteresis loops.

4.1 MAGNETIC STUDY OF NON-GRANULAR YBCO THIN FILMS

YBCO thin films grown on $SrTiO_3$ (STO) single crystal substrates have been used in this thesis as standard samples to describe the general behaviour of YBCO thin films without granularity. The magnetic analysis of these samples will be compared with those performed in YBCO coated conductors which present inherent granularity induced by the low angle grain boundaries replicated from the substrate through the multilayer structure.

4.1.1 ANALYSIS OF MAGNETIC HYSTERESIS LOOPS

In the previous chapter we have seen that it is possible to determine the critical current density of a superconductor by means of the measurement of its magnetic hysteresis loop.

First we will present a magnetic analysis of a non-granular YBCO thin film based on dc-magnetometry which will allow us to study the general behaviour of a reference sample with a thin film geometry, without granularity. Fig. 4-1 shows a typical saturated hysteresis loop measured for sample $SCt0.27_{ORNL-A}$ applying a maximum field, H_m, of $\sigma_0 H_m$=0.2T, at T=50K. A peak of maximum magnetization, $M_{peak}\Im$100MA/m, appears at zero applied field, H_a=0, as expected for a superconducting thin film with large demagnetizing effects (t/R<0.1) subjected to a field dependent J_c (see section 3.2.3). Moreover, from this saturated loop one can determine the full penetration field of the sample, $H^*\Im$48MA/m ($\sigma_0 H^*\Im$0.06 T), indicated with an arrow in Fig. 4-1(see section 3.2.1).

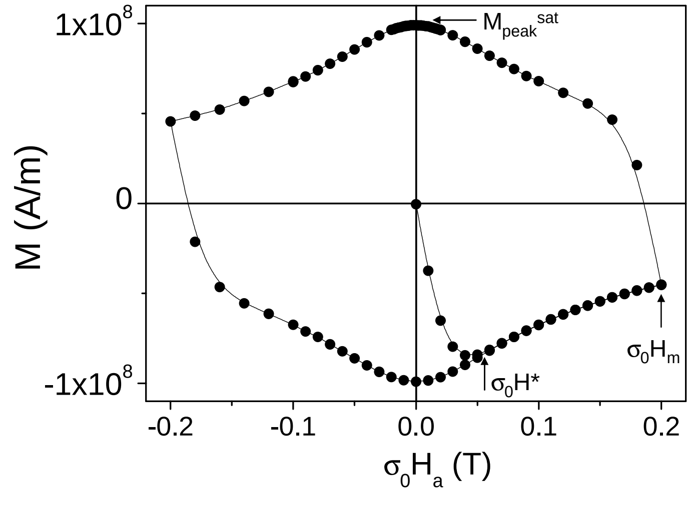

Fig. 4-1. Saturated magnetic hysteresis loop measured for the film $SCt0.27_{ORNL-A}$ at a maximum field of $\sigma_0 H_m$=0.2T and T=50K

For minor hysteresis loops, when H_m<2H*, the value of M_{peak} does depend on the maximum field applied in each loop (see Fig. 4-2). As H_m increase, a higher magnetic flux density can be trapped inside the sample and thus, the value of M_{peak} increase until it reaches the saturated value, M_{peak}^{sat}. The maximum applied field needed to saturate M_{peak}, will be named $H_m(M_{peak}^{sat})$ and as we had described in section 3.2.1 $H_m(M_{peak}^{sat})=2H^*$. Therefore, measuring several minor loops we can find this maximum field, $H_m(M_{peak}^{sat})$, and determine H*. Fig. 4-2 shows some minor loops measured at different maximum applied fields where the values M_{peak}^{sat}, $\sigma_0 H^*$ and $\sigma_0 H_m(M_{peak}^{sat})=2\sigma_0 H^*$ are indicated.

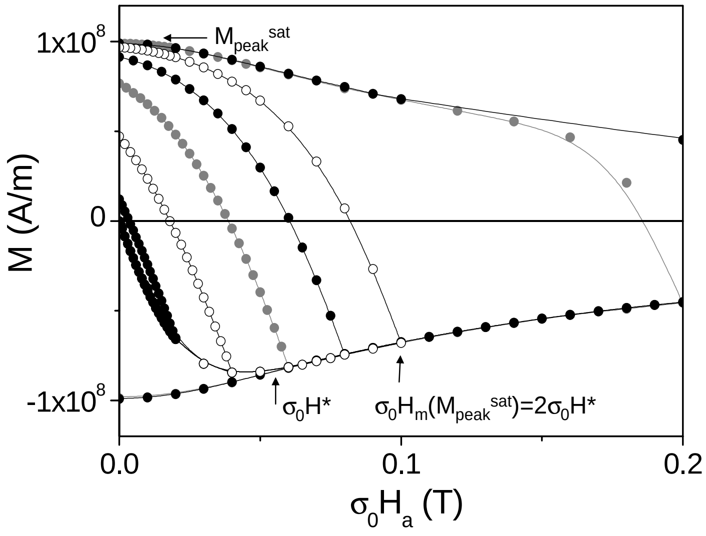

Fig. 4-2. Several hysteresis loops, measured at 50K for SCt0.27$_{ORNL-A}$ with maximum applied fields of $\sigma_0 H_m$=0.02, 0.04, 0.06, 0.08, 0.1, 0.2 and 0.5T.

One can also determine the value of the full penetration field, from a saturated hysteresis loop, as the point where the initial magnetization and the return curve merge, $\sigma_0 H^*(50K)$ℑ0.055T, for the coated conductor presented in Fig. 4-2. The same parameter H* obtained from the first saturated hysteresis loop by means of the relation $H_m(M_{peak}^{sat})=2H^*$, gives $\sigma_0 H^*(50K)$ℑ0.05T. Therefore, since the error in the determination of these two values is about 0.005T one can say that the two processes can be used indistinctly to determine the full penetration field.

From the experimental values, M_{peak}^{sat} and $\sigma_0 H^*$, the sample critical current density, J_c, can be determined from two independent equations (see next section).

4.1.2 CRITICAL CURRENT DENSITY DETERMINATION

On one hand, with the value M_{peak}^{sat} and using equation 3-5 it is possible to determine J_c at zero applied field, with

$$J_c \mid \frac{3\div M}{2R} \mid \frac{3M_{peak}^{sat}}{R} \qquad 4\text{-}1$$

where R is the sample radius,

On the other hand, from the full penetration field, H*, we can determine J_c by using equation 3-6, since the samples analyzed are thin films with 2R/t>100. As we have seen above, the full penetration field can be obtained experimentally in two ways. Directly from a saturated full hysteresis loop or with the value of the maximum applied field applied needed to saturate the magnetic moment (Fig. 4-2). For the later case, equation 3-6 becomes,

$$J_c \mid \frac{2H^*}{1.94t} \mid \frac{H_m(M_{peak}^{sat})}{1.94t} \qquad 4\text{-}2$$

By measuring hysteresis loops at different temperatures, it is possible to determine the dependence of J_c with the temperature. Fig. 4-3 shows three saturated hysteresis loops measured at T=5K, 50K and 77K for the film SCt0.27$_{ORNL\text{-}A}$ at σ_0H_m=1T. Note that the values of M_{peak}^{sat} and H*, decrease as the temperature increases which directly implies a decrease of J_c(T).

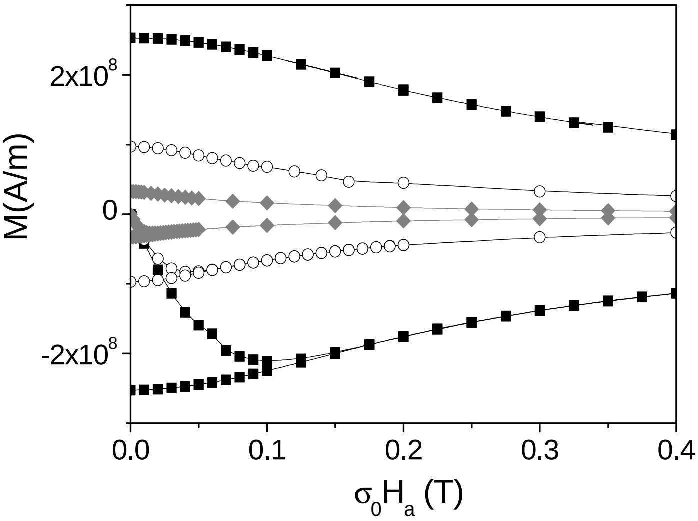

Fig. 4-3. Hysteresis loops measured for the film SCt0.27$_{ORNL\text{-}A}$ with a maximum applied field of σ_0H_m=1T, at T=5K (Â), 50K (¹) and 77K (Î).

Table 4-1 shows the experimental values M_{peak}^{sat} and H* obtained for several non-granular thin films analyzed at T=5K, 50K and 77K and the respective critical current density determined with equations 4-1 and 4-2. The values of J_c obtained with the two equations are quite similar although the error that we have in the determination of H* is higher than the one associated to M_{peak}^{sat}. Additionally we have to take into account that equation 4-2 is strictly valid in the Bean critical state model. Hence, we could consider that the value of J_c calculated from equation 4-1 is more exact. Notice that, for all the samples analyzed we observe a decrease of J_c(T), where J_c(77K) is about one order of magnitude smaller than J_c(5K).

Sample	**T(K)**	**$M_{peak}{}^{sat}$(A/m)**	**J_c(A/m^2) (eq. 4-1)**	**H*(A/m)**	**J_c(A/m^2) (eq. 4-2)**
	5	2.53E+08	4.39E+11	1.19E+05	4.56E+11
$SCt0.27_{ORNL\text{-}A}$	50	9.72E+07	1.69E+11	4.38E+04	1.67E+11
	77	3.27E+07	5.67E+10	2.71E+04	1.03E+11
	5	2.05E+08	2.97E+11	1.59E+05	2.49E+11
$SCt0.66_{ORNL\text{-}A}$	50	7.18E+07	1.04E+11	6.37E+04	9.94E+10
	77	2.18E+07	3.15E+10	1.99E+04	3.11E+10
	5	3.36E+08	3.98E+11	8.75E+04	4.51E+11
$SCt0.2_{Dres}$	50	8.33E+07	9.88E+10	1.59E+04	8.20E+10
	77	2.49E+07	2.95E+10	3.98E+03	2.05E+10
	5	4.31E+08	5.2E+11	1.6E+05	5.5E+11
$SCt0.2_{THEVA}$	50	1.09E+08	1.3E+11	4.0E+04	1.4E+11
	77	2.00E+07	2.4E+10	-	-
	5	2.18E+08	5.1E+11	9.9E+04	4.1E+11
$SCt0.25_{Gott}$	50	5.64E+07	1.3E+11	2.8E+04	1.1E+11
	77	1.26E+07	3.0E+10	5.6E+03	2.3E+10

Table 4-1. Values of $M_{peak}{}^{sat}$ and H obtained for all the thin films analyzed at T=5K, 50K and 77K, and the respective critical current density determined with equations 4-1 and 4-2*

Additionally, from the saturated hysteresis loops and using equation 3-7 (i.e. $J_c(H)=3\div M(H)/2R$), it is possible to determine the dependence of critical current density with the applied magnetic field $J_c(H_a)$, at different temperatures. Fig. 4-4 shows the $J_c(H_a)$ curves obtained for the film $SCt0.27_{ORNL\text{-}A}$ at 5K, 50K and 77K. The analysis of these dependences will be presented in section 5.3.2.

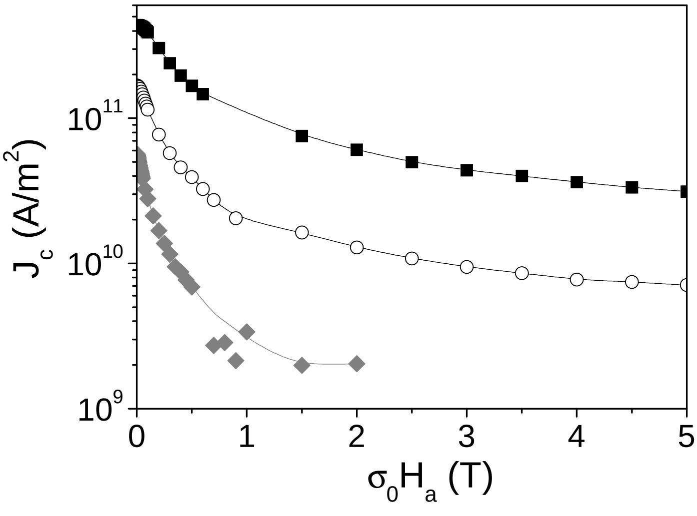

Fig. 4-4. Magnetic field dependence of J_c for the film $SCt0.27_{ORNL\text{-}A}$ at T=5K (Â), 50K (¹) and 77K (Î).

We have seen then, that the analysis of magnetic hysteresis loops in YBCO thin films grown on single crystalline substrates, allow us to determine the critical current density as a function of temperature and magnetic field.

4.2 MAGNETIC STUDY OF COATED CONDUCTORS

In this section we will discuss the anomalous behaviour observed in the hysteresis loops of coated conductors due to the inherent granularity present in these materials and we will distinguish them from those encountered in the previous section for non-granular thin films. In fact, the first thing that one has to realize is that the metallic substrate of a coated conductor is magnetic and therefore we need to separate its signal from the signal coming from the superconducting layer.

4.2.1 CONTRIBUTION OF THE MAGNETIC SUBSTRATE IN THE HYSTERESIS LOOPS

When we measure a hysteresis loop of a coated conductor both, the signal coming from the superconductor layer and the signal coming from the magnetic substrate, are measured by the SQUID magnetometer. Therefore the substrate subtraction is required from the measured hysteresis loops, especially for the case of RABiTS coated conductors with a nickel tape, since this substrate has a large magnetic signal.

First we will analyze the case of IBAD coated conductors, where the metallic tape used is Ni-Cr stainless steel (SS) or Hastelloy (2.2.1 and 2.2.2), which both has a low magnetic signal. In order to see the contribution of the substrate in the total magnetic signal, the hysteresis loop of a substrate without the superconducting layer has been measured under the same conditions as the coated conductor (Fig. 4-5). Notice that the hysteresis loop obtained for the coated conductor (closed symbols) appears tilted according to the magnetic moment contribution of the substrate (open symbols). Therefore, the signal coming from the substrate can be removed directly, subtracting a hysteresis loop measured for a substrate at the total hysteresis loop obtained for the coated conductor. Although, we have to take caution in using a substrate with the same surface as the coated conductor, in order to minimize the demagnetizing effects sensible to the sample geometry.

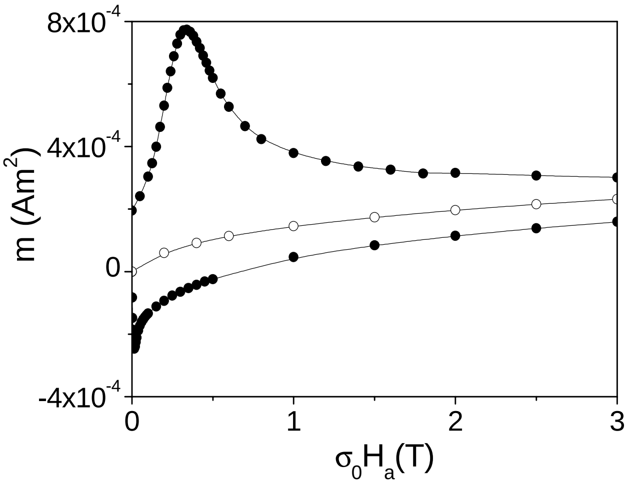

Fig. 4-5. Hysteresis loops measured for the tape IBADt1.6a$_{Gott}$ (closed symbols) and for an IBAD substrate of stainless steel (open symbols), at 5K and $\sigma_0 H_m$=5T

The dependence of the stainless steel magnetic moment with the temperature, in the working range (5K, 77K) is significant and thus it is important to measure the coated conductor and the substrate at the same temperature if one wants to perform a direct subtraction. The same has to be considered for IBAD coated conductors with Hastelloy substrate. Fig. 4-6 shows the magnetic hysteresis loops obtained for a stainless steel tape at T=5K and 77K. Notice that the magnetic moment at 77K is practically linear with the magnetic field whereas the signal obtained at 5K is much higher and shows the typical potential dependence with the magnetic field. Additionally one observes that although the tape has a magnetic signal, it does not present a hysteretic behaviour.

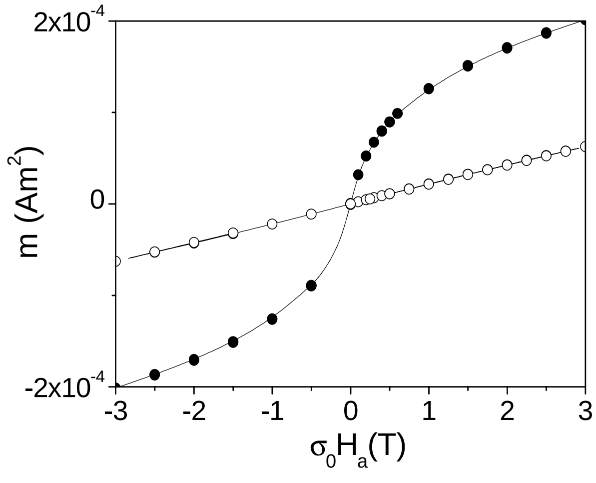

Fig. 4-6. Magnetic loops measured for a stainless steel tape, at T=5k (closed symbols) and 77K (open symbols).

The situation is rather different when analyzing RABiTS coated conductors. In that case, two different micro-alloyed nickel tapes have been used as a metallic substrate, Nickel-0.1%Manganese (Ni-Mn) and Nickel-3%Wolfram (Ni-W) (see sections

2.2.1 and 2.2.2). The magnetic signal is different depending on the alloy used in each case. Fig. 4-7 shows the magnetic hysteresis loops obtained for two equal pieces of the different nickel tapes at 100K. Notice that the Ni-Mn substrate shows a strong magnetic signal and presents a notable hysteresis, while the other substrate (Ni-W) is less magnetic.

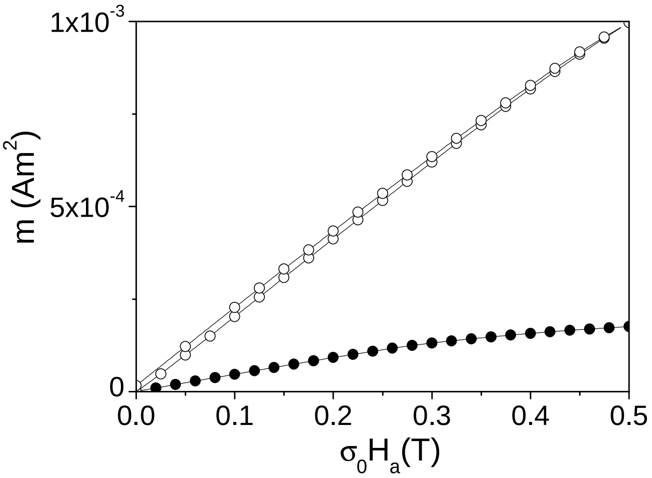

Fig. 4-7. Magnetic hysteresis loops measured for two different micro-alloyed tapes, Ni-W (closed symbols) and Ni-Mn (open symbols), at T=100K.

Contrary to that observed in the stainless steel or Hastellow tapes, the temperature dependence of the magnetic moment observed for all the nickel tapes is almost constant in the range of temperatures between 5K and 100K because of the higher Curie temperature. Fig. 4-8 shows the magnetic moment measured for a Ni-W tape in comparison with a Ni-Cr stainless steel IBAD substrate (SS), as a function of the temperature at σ_0H_a=0.5T, where the different behaviour in the range of T=5-100K can be seen. For this applied field, σ_0H_a=0.5T, the magnetic moment of the NiW tape is already saturated.

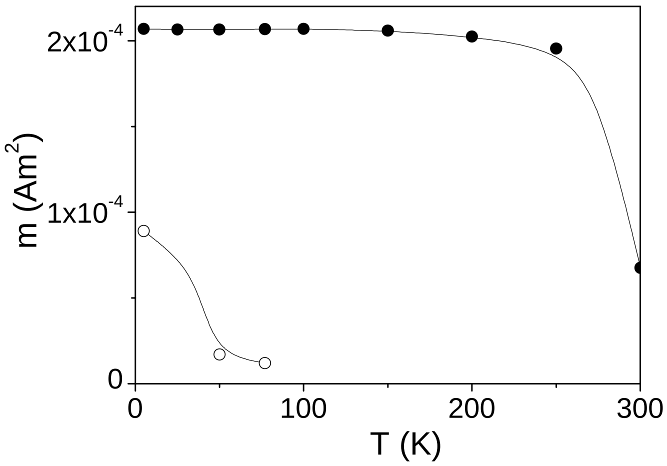

Fig. 4-8. Temperature dependence of the magnetic moment at σ_0H_a=0.5T, for a Ni-W tape (closed symbols) and a Ni-Cr Stainless steel tape (open symbols).

For RABiTS coated conductors, we could not obtain the hysteresis loops associated to the superconductor layer by subtracting the loops measured for a piece of substrate to those obtained for the coated conductor, as we have done for IBAD samples. In fact, we have realized that the demagnetizing effects for the nickel substrates are much stronger than that for the stainless steel tapes and thus the signal is very sensible to the substrate geometry. For instance, by using samples with exactly the same surface but slightly different lateral dimensions we have obtained very different magnetization loops. However, since the magnetic moment of the nickel tape stays almost constant until temperatures above the YBCO critical temperature (T_c=90K), we can subtract the substrate signal by measuring the sample at a temperature higher than the YBCO critical temperature (T=100K), where the superconducting layer doesn't give any signal. The hysteresis loop from the superconductor will be then, the one resulting from the subtraction of a hysteresis loop measured at 100K to the hysteresis loop measured at the wanted temperature. So that, by using the magnetic loop obtained for exactly the same substrate the possible variations in the magnetic moment due to the demagnetizing field effects sensible to the substrate geometry are avoided.

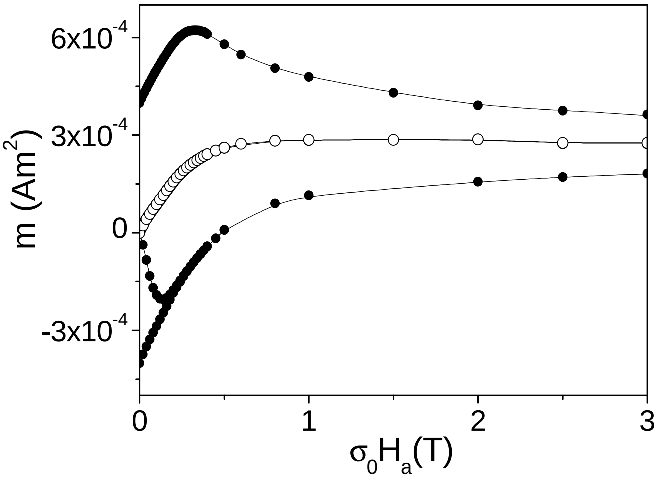

Fig. 4-9. Hysteresis loops measured for the tape RAB.t1.37$_{ORNL-C}$ at T=5K (closed symbols) and T=100K (open symbols), at the same conditions of magnetic field, σ_0H_m=5T

Fig. 4-9 shows two magnetic loops measured at T=5K (closed symbols) and T=100K (open symbols) for the RABiTS sample RAB.t1.37$_{ORNL-C}$ with σ_0H_m=5T. The magnetic loop measured at T=100K correspond to the substrate signal, which for this particular sample and at this temperature, presents negligible hysteresis compared with the one measured for the superconductor. When the hysteresis loop of the coated conductor is measured at higher temperatures, the signal coming from the superconducting layer is smaller and thus the contribution of the substrate, which remains constant with the temperature, is more important. In Fig. 4-10 we show a hysteresis loop measured for the same sample at T=77K (closed symbols) and the corresponding loop measured at T=100K (open symbols). In this case the hysteresis of the substrate, although is much smaller than the one of the superconductor, is not negligible.

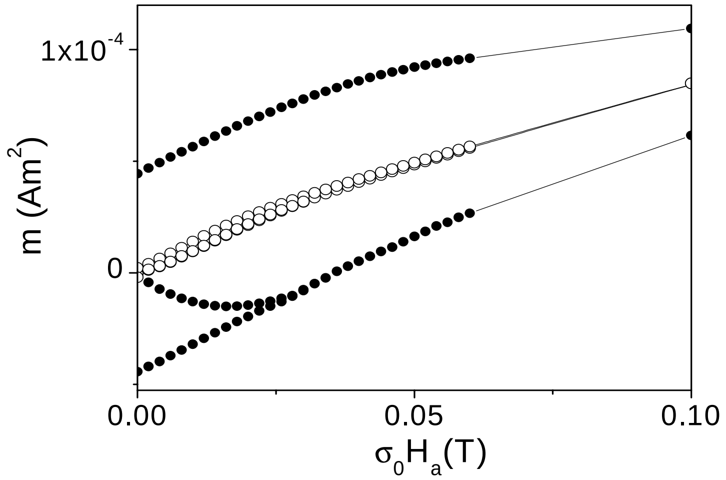

Fig. 4-10. Hysteresis loops measured for the tape RAB.t1.37$_{ORNL-C}$ at T=77K (closed symbols) and T=100K (open symbols), for σ_0Hm=0.5T

In order to be sure that the magnetic history of the nickel tape is the same for the superconductor as for the substrate, we have demagnetized the sample before starting any measurement at each temperature.

4.2.2 ANALYSIS OF THE MAGNETIC HYSTERESIS LOOPS

After the correction of the substrate signal, the superconducting hysteresis loops measured for coated conductors can be analyzed in order to study the granular behaviour present in these samples.

Fig. 4-11 shows a typical hysteresis loop of a coated conductor measured for a RABiTS sample (RABt1.08$_{ORNL-A}$) after substrate subtraction for a maximum applied field σ_0H_m=0.5T at 5K (open symbols). We have compared it with the hysteresis loop measured at the same conditions for a non-granular thin film, SCt0.27$_{ORNL-A}$ (closed symbols). Remarkably, the hysteresis loop for the coated conductor appears to be anomalous with a maximum on the reverse branch of the magnetization at a positive applied magnetic field, σ_0H_a=0.24T at 5K, instead of at σ_0H_a=0T as expected for a superconducting film (see section 3.2.3 and 4.1.1).

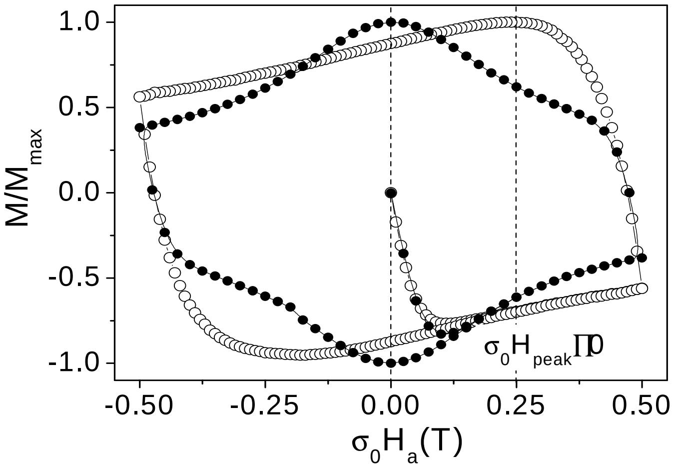

Fig. 4-11. Magnetic hysteresis loops obtained at T=5K and $\sigma_0 H_m$=0.5T, for the film SCt0.27$_{ORNL\text{-}A}$ (closed symbols) and for the coated conductor RABt1.08$_{ORNL\text{-}A}$ (open symbols).

This is up to our knowledge the first time that complete hysteresis loops of coated conductors have been measured. By doing that we have observed that the magnetization peak in the reverse branch of the hysteresis loops always appears at H_a>0 for this materials.

A magnetization peak at H_a∏0 has been predicted considering a certain field dependence of J_c, for samples without large demagnetizing effects (see section 3.2.3). In that case, however, the peak appears at H_a<0 instead of at H_a>0, as we observe. Additionally in coated conductors, we have to consider large demagnetizing effects since the ratio R/t is always very large. We neither can associate the peak appearing at H_a>0 to the fact of having field induced vortex pinning centres, since considering that, we should have a symmetrical loop with respect to H_a=0, i.e. a magnetization peak in the reverse magnetization curve at the same positive an negative values of H_a.

However, similar peaks have been observed previously in BiSCCO tapes [76], YBCO films with artificial granularity [77] and recently in YBCO bycristals [78], where the effect of having a peak in the reverse magnetization at H_a>0, could be ascribed to granularity effects and explained by the same mechanism as that of the hysteretic behaviour of J_c observed in transport measurements of polycrystalline samples [79,80].

The considered model describes the shift of the magnetization peak and the anomalous resulting hysteresis loops, by means of the size effects of the grains which induce a return magnetic field through the grain boundaries (see section 3.4.2).

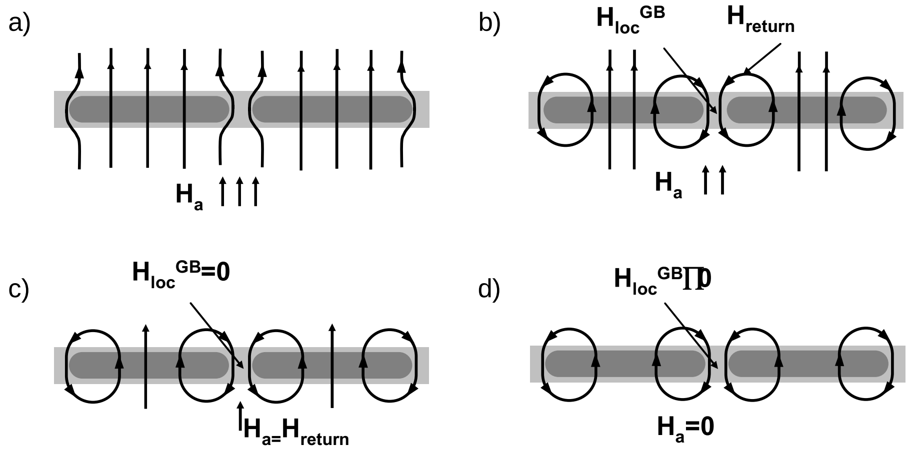

Fig. 4-12. Schematic representation of the magnetic fields at a grain boundary at different applied fields.

As the magnetic field is ramped up, flux enters the material and gets pinned into the grains (Fig. 4-12a), subsequent decrease of the magnetic field results in a reverse magnetic field component through the grain boundaries due to the flux lines trapped in the grains (Fig. 4-12b). Thus, the local magnetic field at the grain boundary, H_{loc}^{GB}, results from the vectorial sum of the applied magnetic field, H_a, and the return field coming from each grain that contributes at the grain boundary, H_{return}.

$$H_{loc}^{GB} \mid H_a 4 H_{return} \qquad 4\text{-}3$$

Consequently, the magnetization peak will appear when $H_{loc}^{GB}=0$, and thus when $H_{peak}\Im H_{return}$ (Fig. 4-12c). If the magnetic field is decreased until $H_a=0$, the local field at the grain boundaries will be given by the return field coming from the grains, $H_{loc}\Im\text{-}H_{return}$ (Fig. 4-12d).

Magnetization measurements are then a very powerful method to infer the granularity effects of coated conductors since one only has to detect a peak in the reverse branch of the magnetization at $H_a>0$. Fig. 4-13 shows several hysteresis loops measured at different H_m for RABt1.08$_{ORNL\text{-}A}$ at 5K. As the maximum applied field increase, the value of field where the maximum of the magnetization appears, $H_{peak,}$ increases until saturation is reached.

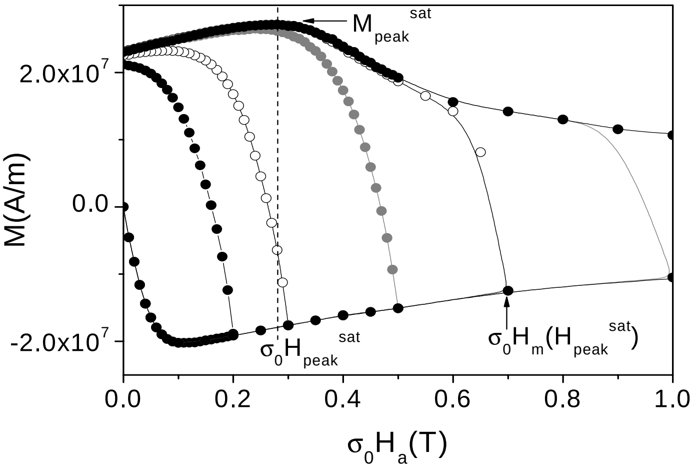

Fig. 4-13. Magnetic hysteresis loops at 5K measured for the RABiTS coated conductor RABt1.08$_{ORNL\text{-}A}$ for $\sigma_0 H_m$=0.2T, 0.3T, 0.5t, 0.7T, 1T and 2T.

Fig. 4-14 shows the evolution of H_{peak} as a function of the maximum applied field, H_m, determined from the hysteresis loops presented in Fig. 4-13. Clearly, H_{peak} increases for low values of H_m and then it saturates. So that, from this measurements, we can determine the maximum applied field that saturates the peak position, $\sigma_0 H_m(H_{peak}^{sat})\Im 0.7T$, and the saturated value of H_{peak}, $\sigma_0 H_{peak}^{sat}=0.28T$. These two magnitudes are characteristic of each coated conductor and will be used in order to determine the grain critical current density, J_c^G, and the average magnetic grain size, <2a>, by means of a formalism developed in this thesis and presented in section 4.2.3.

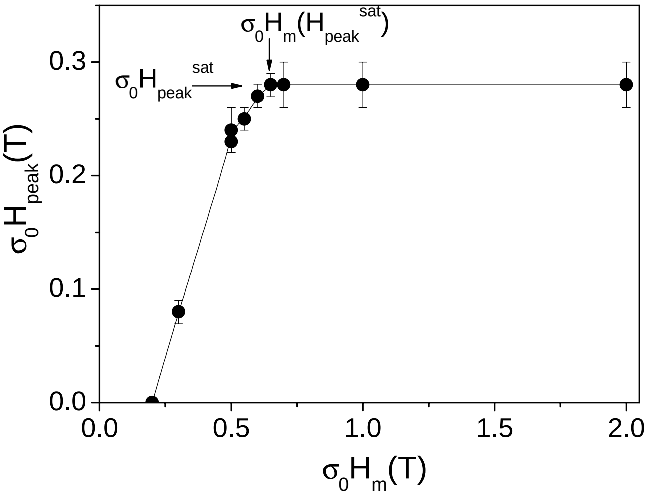

Fig. 4-14. Evolution of the peak position $\sigma_0 H_{peak}$ with the maximum applied field, $\sigma_0 H_m$, obtained for the sample RABt1.08$_{ORNL\text{-}A}$ at 5K. We have indicated with arrows the saturated values $\sigma_0 H_{peak}^{sat}$ and $\sigma_0 H_m(H_{peak}^{sat})$.

Furthermore, we could determine the percolating GB critical current density, J_c^{GB}, by using the value of the magnetic moment measured in a saturated hysteresis loop. We will see in section 4.2.3, that the magnetic moment associated to the grain current loops is negligible compared with the magnetic moment associated to the large percolative loops described for the GB critical current. Hence, the total magnetic moment measured in the hysteresis loop correspond to the magnetic moment of the GB part and thus, the saturated value of the magnetization at the peak position, M_{peak}^{sat}=27MA/m, will determine GB critical current density at H_{loc}=0 (see section 4.2.3)

Fig. 4-15 shows several magnetic hysteresis loops measured for an IBAD coated conductor (IBADt1$_{Gott}$) at the same maximum applied fields as for the RABiTS sample shown above. It is confirmed that both types of coated conductors display the maximum in the reverse magnetization brach at H_a>0. However the magnetization, from different samples, peaks at different H_a, H_{peak}, and this peak evolves differently by increasing H_m. For this particular IBAD sample, both the maximum field that saturates the peak position, $\sigma_0 H_m(H_{peak}^{sat})\Im 0.5T$, and specially the saturated value of H_{peak}, $\sigma_0 H_{peak}^{sat}$=0.14T, are smaller than for the previous RABiTS sample analyzed. The value of the magnetization peak obtained for this IBAD sample is, M_{peak}^{sat}=97MA/m.

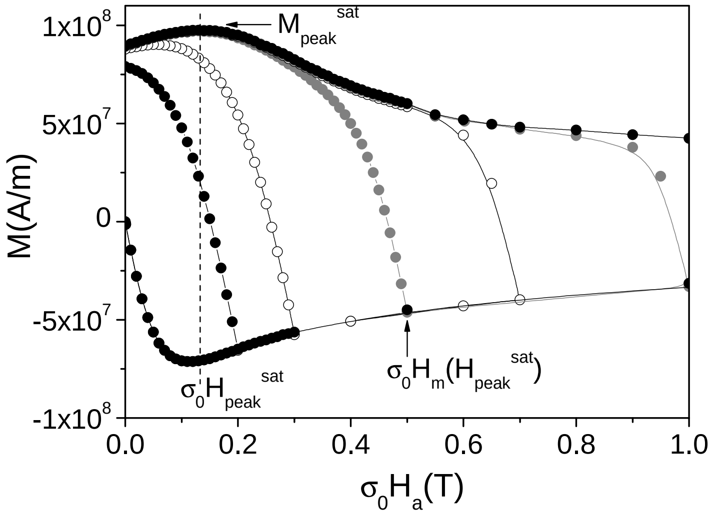

Fig. 4-15. Magnetic hysteresis loops at 5K measured for the IBAD coated conductor IBADt1$_{Gott}$ for $\sigma_0 H_m$ =0.2, 0.3, 0.5, 0.7, 1 and 2T.

The comprehension of the phenomenon that induces the peculiar anomalous hysteresis loops obtained for YBCO coated conductors, i.e. a peak in the reverse magnetization at H_a>0, has allowed us to devolve a unique methodology able to determine both J_c^G and J_c^{GB} in these samples, and study their correlation. Hence, by measuring several hysteresis loops at different temperatures, we could obtain the temperature dependence of J_c^G and J_c^{GB}.

We show in Fig. 4-16 three saturated hysteresis loops measured at T=5K, 50K and 77K for the sample RABt1.08$_{ORNL-A}$ at $\sigma_0 H_m$=1T, 0.5T and 0.2T respectively.

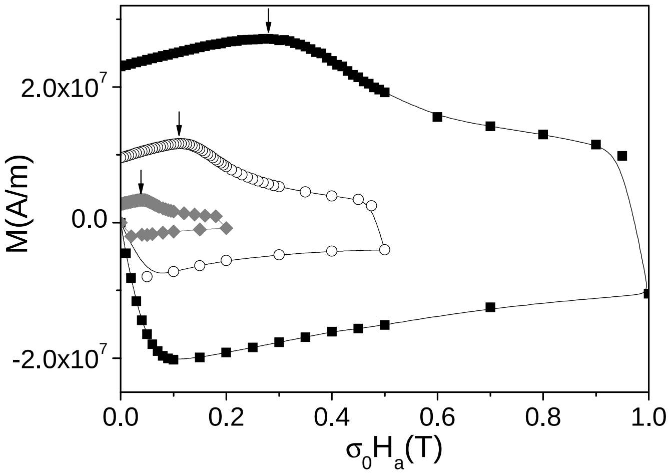

Fig. 4-16. Saturated hysteresis loops obtained for the sample RABt1.08$_{ORNL-A}$ at T=5K (Â), 50K (¹) and 77K (Î) for $σ_0H_m$=1T, 0.5T and 0.2T, respectively.

Notice that both the value of M_{peak}^{sat} and H_{peak}^{sat} decrease by increasing the temperature. We will see in section 4.2.3 that J_c^{GB} and J_c^{G} are proportional to M_{peak}^{sat} and H_{peak}^{sat}, respectively and thus a decrease of these values with the temperature is associated with a decrease of J_c^{GB}(T) and J_c^{G}(T).

Fig. 4-17 presents the evolution of H_{peak} as a function of the maximum applied field, H_m, determined with the hysteresis loops measured at 5K, 50K and 77K for RABt1.08$_{ORNL-A}$. Notice that, the maximum field that saturates the peak position, $H_m(H_{peak}^{sat})$, also decrease by increasing the temperature since, as we will see later on it will be related with the full penetration field of the grains, H^*_G, which depends on J_c^{G}(T), as well.

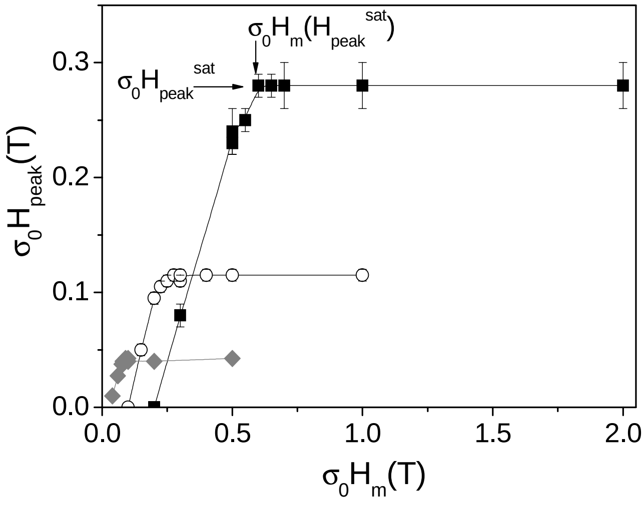

Fig. 4-17. $σ_0H_{peak}$ as a function of $σ_0H_m$ obtained for RABt1.08$_{ORNL-A}$ at T=5K (Â), 50K (¹) and 77K (Î). We have also indicated the saturated values $σ_0H_{peak}^{sat}$ and $σ_0H_m(H_{peak}^{sat})$ at 5K.

4.2.3 CRITICAL CURRENT DENSITY DETERMINATION: THEORETICAL MODEL DEVELOPED

Based on the peculiar features of the YBCO coated conductors hysteresis loops, which can be associated with the percolative nature of the grain boundary network, we have devolved a formalism by which J_c^{GB} and J_c^{G} can be evaluated simultaneously from a set of hysteresis loops, in the framework of the critical state model.

4.2.3.a GRAIN CRITICAL CURRENT DENSITY AND GRAIN SIZE

The model used in this analysis considers that the anomalous peak in the magnetic hysteresis loop for coated conductors can be explained by means of the magnetic flux trapped inside the grains which return through the grain boundaries (see section 4.2.2). Therefore, the local magnetic field at the grain boundaries can be determined by equation 4-3 ($H_{loc}^{GB}=H_a-H_{return}$). In fact, we would have to consider the contribution of the self-magnetic field arising from the percolating GB critical current density in the determination of the local magnetic field, i.e. $H_{loc}^{GB}=H_a+H_{self}^{GB}-H_{return}$. However, it has been evidenced by critical state model calculations [65,70] that this field can be neglected in the reverse magnetization curve for thin films (where we are performing the analysis) and thus we have considered the local magnetic field to be uniform over the sample as, $H_{loc}^{GB}=H_a-H_{return}$.

The relation $H_{peak}\Im H_{return}$ establishes that H_{peak}^{sat} is reached when the grain magnetization saturates and thus.

$$H_{peak}^{sat}(T) \mid H_{return}^{\max}(T) \qquad 4\text{-}4$$

Moreover, $H_m(H_{peak}^{sat})$ is a measure of the magnetic field required to saturate the grain magnetization at the peak position, so,

$$H_m(H_{peak}^{sat})\,4\,H_{peak}^{sat} \mid 2H^*_G \qquad 4\text{-}5$$

where H^*_G is the full penetration field of the grains (see section 3.2.1).

Due to the dependence of $J_c^{G}(H)$, the determination of the grains full penetration field by means of the saturation of the grain magnetization at $H_a=H_{peak}^{sat}$ will give us a smaller value of H^*_G than the one that we would obtain if the saturation at $H_a=0$ had been considered.

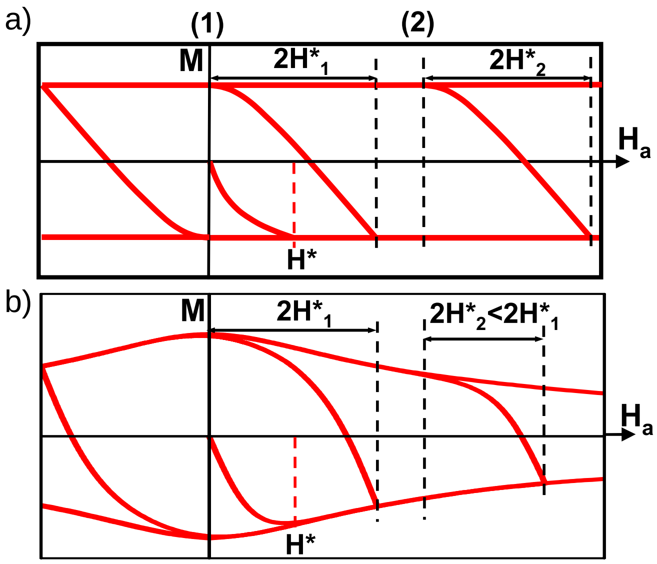

Fig. 4-18. Hysteresis loops for an infinite cylinder determined with the Bean critical state model (a) and measured for a real thin film with $J_c(H)$ (b) at different maximum applied fields.

Fig. 4-18 shows the hysteresis loops determined for thin films with the Bean critical state model at different maximum applied fields (Fig. 4-18a) and the equivalent ones measured for a real thin film which presents a $J_c(H)$ dependence (Fig. 4-18b). In the Bean critical state model (Fig. 4-18a), saturation at position (1) requires the same 2H* as saturation at position (2), $2H^*_1=2H^*_2$. However, considering a $J_c(H)$ dependence (Fig. 4-18b), saturation at $H_a=0$ (1) requires a higher applied magnetic field than saturation at $H_a>0$ (2), $2H^*_1>2H^*_2$.

Therefore, in order to find the value of $2H^*_G$ at $H_a=0$, i.e. the saturation of the grain magnetization at $H_a=0$, we have to measure the saturation of $H_{return}(H_a=0)$. In order to do that we have measured the saturation of the remanent magnetization at $H_a=0$, $H_m(M_{rem}^{sat})$ instead of measuring the saturation of the peak position at $H_a=H_{peak}^{sat}$, $H_m(H_{peak}^{sat})$. It has been shown, in section 4.2.2 (Fig. 4-12d), that at $H_a=0$, the local magnetic field at the grain boundaries is given by the return field coming from the grains, i.e. $H_{loc}\Im-H_{return}(H_a=0)$. So that, when for a certain maximum applied field the value of $H_{return}(H_a=0)$ is not saturated, the local magnetic field at the grain boundaries is neither saturated and thus, the magnetic moment associated to the percolative critical current will depend on this field, i.e. is not saturated. Then, the maximum applied field that saturates the remanent magnetic moment, $H_m(M_{rem}^{sat})$, corresponds to the applied magnetic field that saturates the local magnetic field at the GBs at $H_a=0$, i.e. that saturates the return magnetic field at $H_a=0$ and therefore $H_m(M_{rem}^{sat})\Im 2H^*_G$.

However, in this process, we have to be sure that the saturation of the remanent magnetization is due to the saturation of the return field (saturation of the grain magnetization) and not owing to the saturation of the GB magnetization, i.e that the full penetration field associated to the grains is higher than that associated to the whole sample, $H^*_G > H^*_S$. We have calculated H^*_S with the value of J_c^{GB} (determined by means of equation 4-12 shown in next section), and by using equation 3-6, valid for thin films, i.e. $H^*_S = 1.94 J_c^{GB} t/2$. For all the samples analyzed we have found that the condition $H^*_G > H^*_S$ occurs. Consequently instead of using equation 4-5 to determine the full penetration field of the grains we will use,

$$H_m(M_{rem}^{sat}) \mid 2H^*_G \qquad for \qquad H^*_G \} H^*_S \tag{4-6}$$

Thus, we have seen that we can determine the saturated value of the return field coming from the grains, H_{return}, by measuring the position of the magnetization peak, $H_{return} \Im H_{peak}$, and moreover that we can find the value of the grain full penetration field, H^*_G, by means of the experimental value $H_m(M_{rem}^{sat})$ according to equation 4-6. Therefore, by using the theoretical relations $J_c^G(H_{return})$ and $J_c^G(H^*_G)$ described below, we will be able to determine the grain critical current density, J_c^G, and the magnetic average grain size, <2a>, by means of the experimental values H_{peak}^{sat} and $H_m(M_{rem}^{sat})$.

Thanks to our collaboration with the "Universitat Autònoma de Barcelona", A. Sanchez et al. have calculated the return field for saturated cylinders of different aspect ratios a/t, where a is the cylinder radius and t the cylinder thickness, in order to emulate the grains composing IBAD and RABiTS coated conductors [81]. This return field will be more important when increasing the ratio a/t due to stronger demagnetizing effects (see section 3.4.1). We have assumed constant J_c (Bean critical state model), and that two isolated adjacent grains (zero separation) contribute to the return field at their grain boundary. According to these calculations the grain critical current density can be determined by,

$$J_c^G \mid \frac{H_{return}^{\max}}{xt} - \frac{H_{Peak}^{sat}}{xt} \tag{4-7}$$

where x is a numerically calculated dimensionless factor depending on the ratio a/t shown in Fig. 4-19.

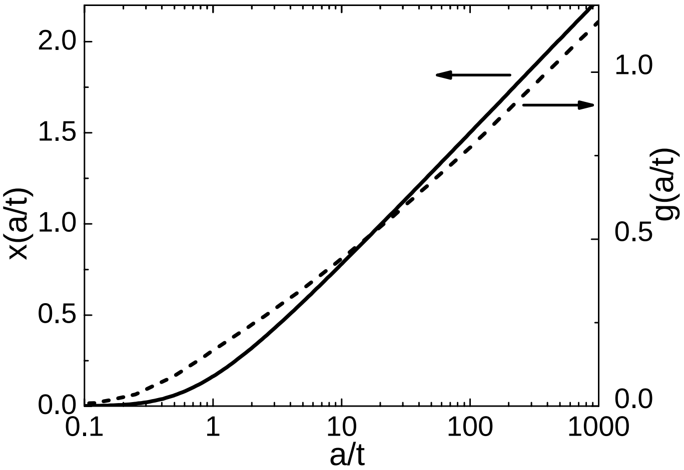

Fig. 4-19. Numerically calculated dimensionless factors g and x as function of a/t.

Additionally, by using a numerical simulation based on energy minimization in the Bean critical state model they have also calculated the full penetration field for cylinders of different aspect ratios, a/t [62,65]. In fact, they have considered an effective penetration field calculated from the maximum in the imaginary part of the ac-susceptibility (see section 3.3.1). Results for any value of 2a/t can be expressed as;

$$H^* \mid J_c n a \qquad 4\text{-}8$$

where, n is a numerically calculated dimensionless factor depending on the ratio 2a/t shown in Fig. 4-20. In the limits 2a/t<0.1 and 2a/t>100, the value n can be calculated analytically by means of equations 3-4 and 3-6, respectively.

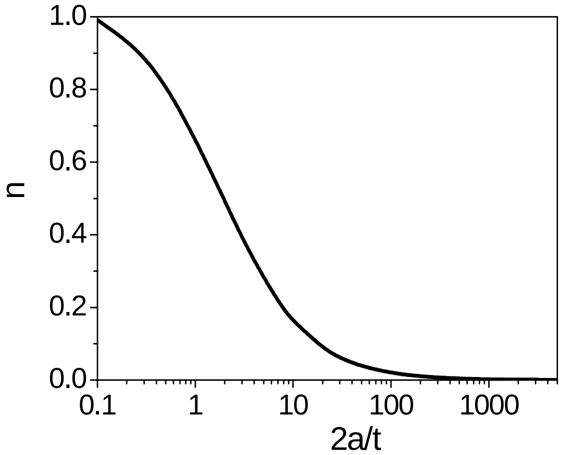

Fig. 4-20. Numerically calculated dimensionless factor n as function of the ratio radius thickness, 2a/t

So that, by using equation 4-8, we obtain the relation $J_c^G(H^*_G)$ as,

$$J_c^G \mid \frac{H^*_G}{na} - \frac{H_m(M_{rem}^{sat})}{2na} \qquad for \qquad H^*_G \} H^*_S \qquad 4\text{-}9$$

where the condition $H^*_G > H^*_S$ occurs for all the samples analyzed.

These equations derived for isolated cylindrical grains do not need to be corrected for any component of the grain boundary self-field since, as it has been commented above, this field can be neglected in thin film materials [65,70]. Therefore, combining equation 4-7 and 4-9 we obtain the relation,

$$\frac{H_{peak}^{sat}}{H_m(M_{rem}^{sat})} \mid \frac{x}{2n}\frac{t}{a} \mid g(a/t) \qquad 4\text{-}10$$

which can be used to estimate the average grain size, <2a>, by means of the function g(a/t) shown in Fig. 4-19, and the experimental value $H_{peak}^{sat}/H_m(M_{rem}^{sat})$. The determination of the grain size enables us to estimate J_c^G at zero applied field, by using equation 4-7 or 4-9 without any free parameter. However, in this process we have to take into account that the return field determined by equation 4-7 is not the value at $H_a=0$, but at $H_a=H_{peak}^{sat}$. In our calculations, we have estimated the decrease of J_c^G from $H_a=0$ to H_{peak}^{sat} from results of thin films and we have introduced this factor as error bar in the determined value of J_c^G.

In summary, we have seen that the values J_c^G and <2a>, at different temperatures, can be determined for a given coated conductor if we measure the correspondent hysteresis loops at each temperature and find the experimental values $\sigma_0 H_{peak}^{sat}$ and $\sigma_0 H_m(M_{rem}^{sat})$. Fig. 4-21 shows several loops measured at 77K for a RABiTS sample (RABt0.34$_{ORNL-B}$) where we have indicated the value $\sigma_0 H_{peak}^{sat}$ℑ0.033T. For this particular sample, we have obtained $\sigma_0 H_{peak}^{sat}$ℑ0.21T and 0.086T for T=5K and 50K, respectively.

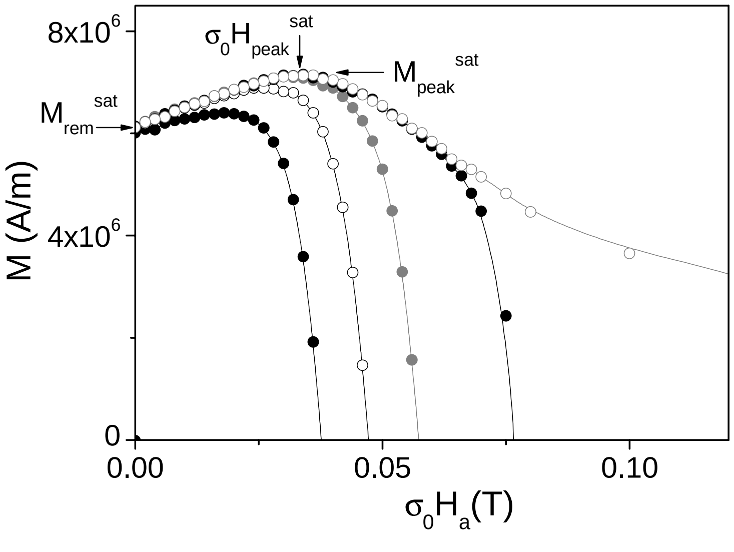

Fig. 4-21. Magnetic hysteresis loops measured for the RABiTS sample RABt0.34$_{ORNL-B}$, at 77K for $\sigma_0 H_m$=0.04T, 0.05T, 0.06T, 0.08T and 0.2T.

In order to determine the maximum field that saturates the remanent magnetization, $\sigma_0 H_m(M_{rem}^{sat})$, we have represented the evolution of the remanent magnetization normalized to its saturated value, M_{rem}/M_{rem}^{sat}, with the maximum applied field at different temperatures, being $\sigma_0 H_m(M_{rem}^{sat}) \Im 0.16$T, 0.063T and 0.024T at 5K, 50K and 77K, respectively (Fig. 4-22). Notice that, for the coated conductor considered in this case, the remanent magnetization increases until saturation. As we will discuss in section 4.2.4.e this is not a general dependence for all the samples analyzed since for other coated conductors we have observed that the remanent magnetization decreases until saturation is reached (see section 4.2.4.e).

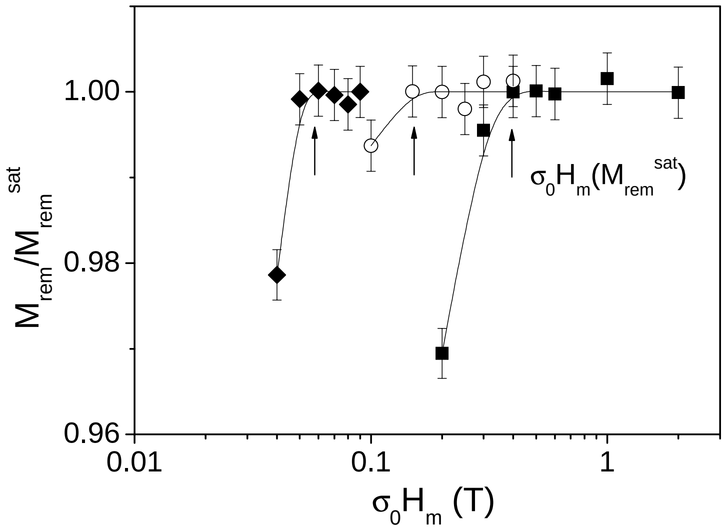

Fig. 4-22. Remanent magnetization, normalized to its saturated value, M_{rem}/M_{rem}^{sat}, as a function of the maximum applied field $\sigma_0 H_m$, determined for the sample RABt0.34$_{ORNL-B}$ at 5K (Â), 50K (¹) and 77K(Î). We have indicated with arrows the maximum applied field needed to saturate the remanent magnetization $\sigma_0 H_m(M_{rem}^{sat})$ at each temperature.

Once the experimental values $\sigma_0 H_{peak}^{sat}$ and $\sigma_0 H_m(M_{rem}^{sat})$ have been determined at different temperatures, we use the Labview program *JcG&JcGB*, devolved in this Thesis, which by means of these values and the thickness of the sample, t, as input parameters, give us the grain radius,<a>, and the grain critical current density, J_c^G, at each temperature according to equations 4-7 and 4-12 and the values x, and g in Fig. 4-19.

Fig. 4-23 shows the main screen of the Labview program devolved (Notice that the units in the program are in cgs). We have indicated in green the input parameters. Since we may have a quite large uncertainly in the determination of $\sigma_0 H_m(M_{rem}^{sat})$, we introduce the maximum value of $\sigma_0 H_m$ that we have measured, which does not saturates the remanent magnetization and also the minim value of $\sigma_0 H_m$ that has already saturate the magnetization. These two fields are used in order to calculate the error induced in the determination of the grain size and the grain critical current density. Orange tables in the screen show the resultant values of <a> and J_c^G obtained for the sample RABt0.34$_{ORNL-B}$ with its respective errors. The mean values together with the maximum and minimum errors, are represented in the graphs. The curve $J_c^{GB}(T)$ which can also be calculated with the program (see next section) is also represented in the graph $J_c(T)$.

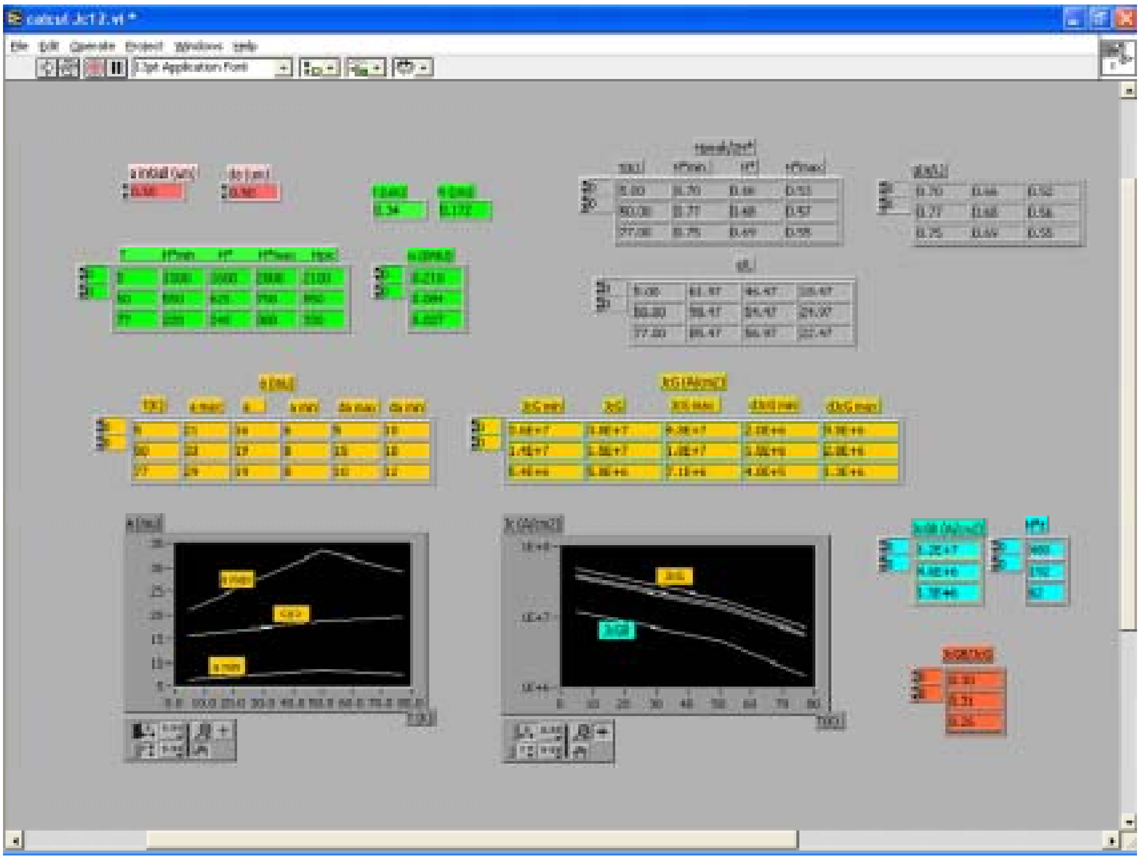

Fig. 4-23. Main screen of the Labview program, named JcG&JcGB, created in order to calculate J_c^G, J_c^{GB} and <2a> at different temperatures, for a certain coated conductor. The input parameters needed to run the program are indicated in green. We have shown the results obtained for the sample RABt0.34$_{ORNL-B}$.

4.2.3.b GRAIN BOUNDARY CRITICAL CURRENT DENSITY

The grain boundary critical current density can be determined from a saturated hysteresis loop by using equation 3-7 if we make sure that the total magnetic moment measured in the hysteresis loop, m, corresponds to the magnetic moment associated to the GB critical current density, i.e. $m \Im m^{GB}$. The magnetic moment associated to the grain current loops, m^G, can be estimated by means of

$$m^G \mid M^G V_G N - \frac{J_c^G a}{3} V_G N \,\Omega\, \frac{J_c^G a}{3} V_S \qquad 4\text{-}11$$

where V_G is the grain volume, N is the number of grains and V_S is the sample volume. We have considered that the grains fill the entire sample ($N=V_S/V_G$) and $J_c^G=3M^G/a$ (equation 3-7). For all the samples analyzed we have obtained $m^G ℑ 5.10^{-2}-10^{-3}m$ which indicates that the large current loops of the GB percolating currents generate a larger magnetic moment than the grain current loops associated to J_c^G. Thus, it can be considered that the magnetic moments of the m(H) cycles solely correspond to the magnetic moment of the GB component though strongly influenced by the return field of the grains.

Therefore, the temperature dependence of J_c^{GB} at $H_{loc} ℑ 0$ can be calculated from the value M_{peak}^{sat} (indicated in Fig. 4-21) determined at different temperatures, by using

$$J_c^{GB} \mid \frac{3M_{peak}^{sat}}{R} \qquad 4\text{-}12$$

where R is the sample radius.

By applying the equation 4-12 to the ascending and descending branches of the m(H) curve, the hysteretic dependence of $J_c^{GB}(H)$ can be determined (see section 4.2.4.c)

For the sample described above, RABt0.34$_{ORNL-B}$, we have obtained the experimental values M_{peak}^{sat}= 56.5MA/m, 22,6MA/m and 7.26MA/m at 5K, 50K and 77K, respectively. With the Labview program *JcG&JcGB* we can determine J_c^{GB} at each temperature, by using equation 4-12 with M_{peak}^{sat} and R as input parameters. Additionally, with the values of J_c^{GB} and by means of equation 3-6, we can also calculate the sample full penetration field, $H^*_s=1.94J_c^{GB}t/2$. Results obtained for the sample RABt0.34$_{ORNL-B}$ at different temperatures are shown in the blue tables of the program screen (see Fig. 4-23). Notice that the values of H^*_S obtained, $σ_0H^*_S$=0.048T, 0.019T and 0.0062T, at 5K, 50K and 77K, respectively, are much smaller than the correspondent maximum applied fields needed to saturate the remanent magnetization ($σ_0H_m(M_{rem}^{sat}) ℑ 0.16$T, 0.063T and 0.024T at 5K, 50K and 77K, respectively) and thus we can say that the saturation of the remanent magnetization is due to the saturation of the return field (saturation of the grain magnetization) and not due to the sample saturation, i.e. the condition $H^*_G>H^*_S$ is acomplished.

4.2.4 CONSISTENCY OF THE THEORETICAL MODEL

We have seen that from magnetic hysteresis loops measured at different maximum applied fields, it is possible to determine the three experimental parameters, $\sigma_0 H_{peak}^{sat}$, $\sigma_0 H_m(M_{rem}^{sat})$ and M_{rem}^{sat} which allow as to calculate simultaneously grain and grain boundary critical current densities of IBAD and RABiTS coated conductors as well as and average grain size, <2a>. In order to reach these determinations, a theoretical model based on the anomalous behaviour of the hysteresis loops and the critical state has been developed.

In this section we will check the consistency of this model and its assumptions.

4.2.4.a MAGNETIC FIELD AT A GRAIN BOUNDARY

First of all we will confirm the main idea of our model which is the existence of a negative return field at low angle grain boundaries in the reverse curve of the hysteresis loop due to the demagnetizing effect of the grains.

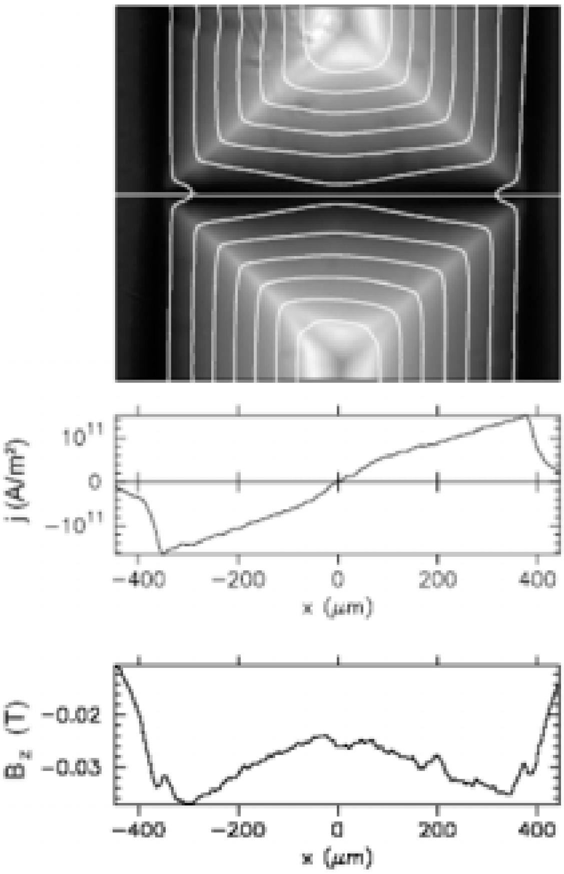

Fig. 4-24. Magneto optical picture at 4.2K from a [001] tilt GB with the current distribution visible as contour lines in the remanent state. Also shown the current and field profiles along the grain boundary.

The best way to verify the presence of this negative field is by means of the magneto optic technique (MO), which allows a direct visualization of magnetic flux in a grain boundary. Fig. 4-24 shows a MO picture with the magnetic field distribution measured for a YBCO thin film grown on a 4^0 [001] STO bycrystal at 4.2K in the remanent state. This picture have been perfomed in the "Zentrum für FunktionWekstoffe" of Göttingen (Germany) during my stay of one month there. The magnetic field can be seen as black and white contrast (strong field in white) and the current distribution as contour lines, calculated from inversion of the Biot Savart's law [56]. Also the profiles of the critical current density and the magnetic field along the grain boundary are shown. The figure clearly evidences the negative profile of magnetic field along the grain boundary. Although we have considered the magnetic field homogeneous over the entire grain boundary we see that a certain inhomogeneity is present.

4.2.4.b CONTRIBUTION OF THE GRAINS FAR FROM THE GRAIN BOUNDARY AT THE RETURN FIELD

The return flux density at the grain boundary has been calculated by assuming that only the two grains that form a grain boundary contribute to the return field. Since the number of grains around a grain boundary increases proportionally to the distance, if there would be a notable contribution of the distant grains, the return field would depend on the sample dimension, i.e. on the number of grains around the grain boundary (Fig. 4-25).

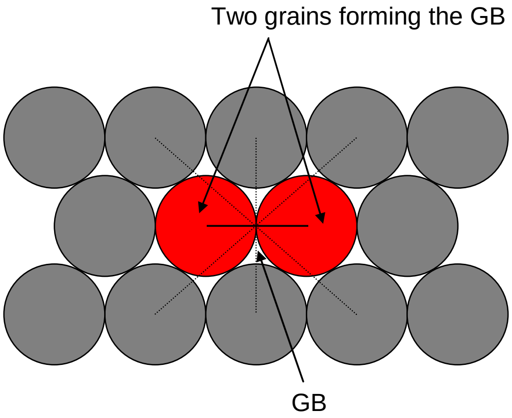

Fig. 4-25. Schematic representation of a granular sample with cylindrical grains. The two grains forming the GB are the ones are that mostly contributes in the total return field at the GB.

Sample IBADt1.6b$_{\mathrm{Gott}}$ has been patterned by standard photolithography two times in a disk shape, firstly with a radius, $R_1 \Im 0.3$cm and afterwards with $R_2 \Im 0.15$cm.

Fig. 4-26 shows two images of the sample taken with an optical microscope a) after the first patterning and b) after the second one, where the sample radius can be measured.

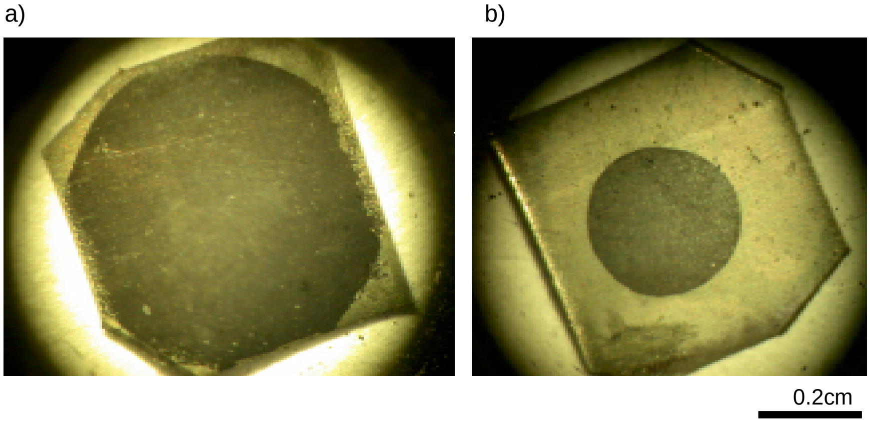

Fig. 4-26. Optical images of IBADt1.6b$_{Gott}$ after the first patterning with a radius R_1 (a) and after the second one with R_2 (b).

Magnetic hysteresis loops at 77K and H_m=0.02, 0.05, 0.1 and 0.2T have been performed at IBADt1.6b$_{Gott}$ after each patterning. Results are shown in Fig. 4-27, where closed symbols correspond to R_1 and open symbols to R_2. According to equation 4-12 the value of the measured magnetic moment decreases as the sample radius is reduced. Assuming that J_c^{GB} stays constant after the patterning, the reduction of the magnetic moment will be given by,

$$\frac{m_1}{m_2} = \frac{R_1^3}{R_2^3} \qquad 4\text{-}13$$

Additionally, from the magnetic hysteresis loops we can determine the sample radius by means of the initial susceptibility calculated for a thin disk in the Meissner state, θ_0, (seccion 3.3.1) which is the initial slope of the first magnetization curve [59].

$$\theta_0 = \frac{dM}{dH} = \frac{8R}{3\phi t} \qquad 4\text{-}14$$

The values obtained for R_1=0.27cm and R_2=0.15cm agree with the ones measured in the optic images. With this values and using equation 4-13 one finds the relation m_1/m_2=5.8 while from the experimental loops one obtain gets m_1/m_2=5.3. The agreement between these two values confirms that the total magnetic moment measured is associated to the GB loops and depends on the sample radius.

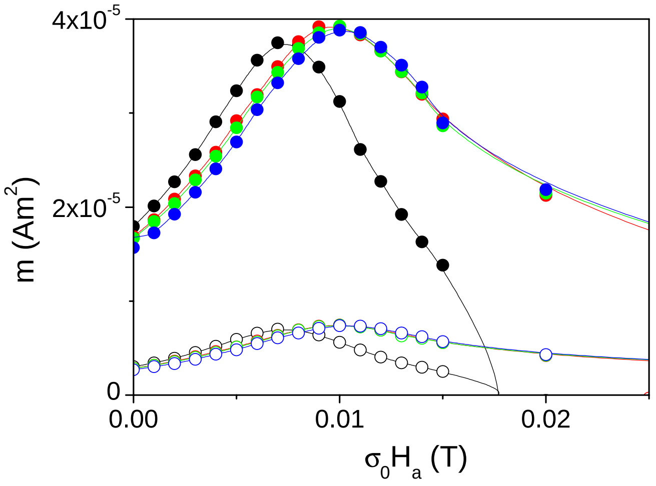

Fig. 4-27. Magnetic hysteresis loops measured for IBADt1.6b$_{Gott}$ patterned as a disk of radius R$_1$ (closed symbols) and R$_2$ (open symbols) at 77K and different H$_m$.

Although the patterning strongly affects the value of magnetic moment in the hysteresis loop, the fact of having a sample with a smaller radius does not change the position of the peak and the saturation of the remanent magnetization. Fig. 4-28 shows the hysteresis loops presented in Fig. 4-27 normalized to m_{sat}^{peak} where the evolution of the peak can be seen more clearly. Since the magnetization peak appears exactly at the same position for all the loops, one can conclude that the return field does not depend on the sample dimension and so the contribution of the distant grains can be neglected.

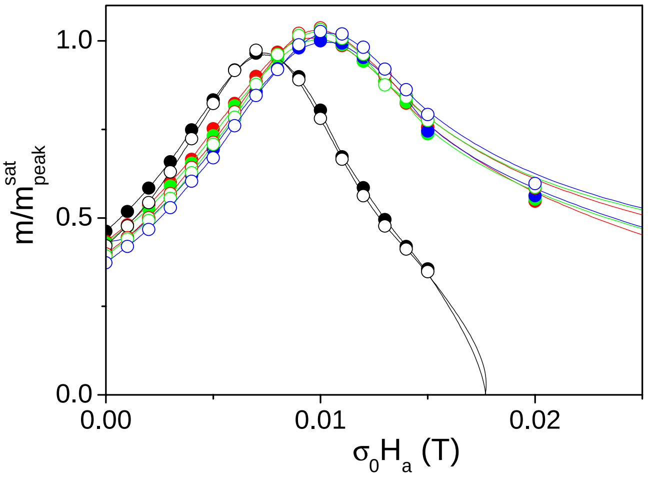

Fig. 4-28. Magnetic hysteresis loops normalized to m_{peak}^{sat}, measured at 77K, for the sample IBADt1.6b$_{Gott}$ patterned as a disk of radius R$_1$ (closed symbols) and R$_2$ (open symbols).

The evolution of the remanent magnetization as a function of the maximum applied magnetic field has been represented in Fig. 4-29. Closed symbols correspond to M^{rem}/M_{rem}^{sat} for the sample with R$_1$ and open symbols for R$_2$. Notice that both curves show the same evolution with the applied magnetic field and that the remanent magnetization saturates exactly at the same maximum applied field, $\sigma_0 H_m(M_{rem}^{sat})$. This result is a confirmation that the saturation of the magnetization is due to the remanent field associated to the grains and not due to the GB loops (see section 4.2.3). Notice that for this coated conductor the saturation of the remanent magnetization occurs after a clear decreasing of the remanent magnetization, contrary to that observed in Fig. 4-22 for the sample RABt0.34$_{ORNL-B}$. The different behaviour observed in the saturation of M^{rem} will be discussed in section 4.2.4.e.

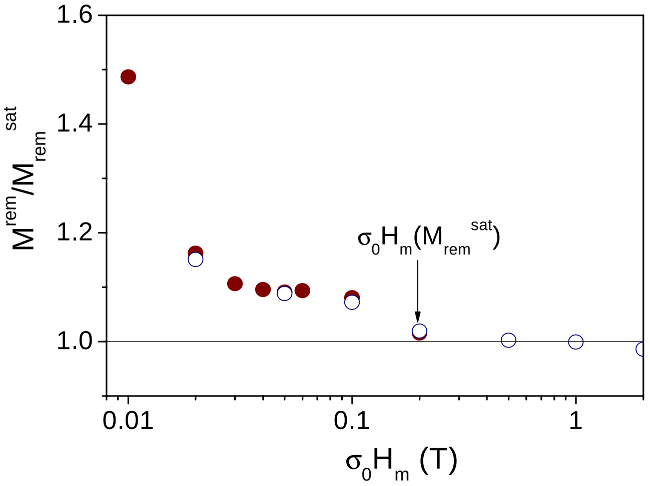

Fig. 4-29. Remanent magnetization normalized to its saturated value as a function of the maximum applied field for IBADt1.6b$_{Gott}$ with R_1 (closed symbols) and with R_2 (open symbols). Also pointed are the maximum applied field that saturates M^{rem} in both cases.

4.2.4.c HYSTERETIC BEHAVIOUR OF J_c^{GB}

The effects of the flux trapping in the grains have been observed earlier in transport measurements by means of an hysteretic behavior for J_c^{GB} [79].

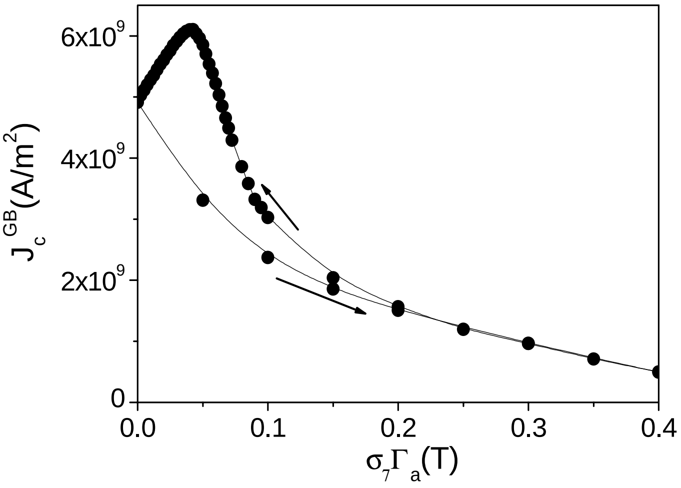

Fig. 4-30. Magnetic field dependence of J_c^{GB} for RABt1.08$_{ORNL-A}$ at 77K and $\sigma_0 H_m$=0.5T where the hysteretic behavior of J_c^{GB} is revealed.

By applying equation 3-7, to both, the initial and the reverse branches of the M(H) curve independently, as $J_c^{GB}=3M/R_s$, one can determine the magnetic field dependence of J_c^{GB} and the associated hysteresis by inductive magnetic measurements.

The hysteretic behaviour of J_c^{GB} appears due to the different magnetic flux distribution at the edge of the grains which contributes to the local field at the grain boundaries (section 3.4.1).

By increasing the applied field in the measurement of a hysteresis loop, a positive magnetic field at the edge of each grain comes appears, H_{edge}, and thus the local field at the grain boundary is higher than the applied field, $H_{local}^{GB}=H_a+H_{edge}$ (Fig. 4-31b). When decreasing the applied field, in the reverse curve of the loop, a negative return field appears at the edge of the grains (see section 4.2.2) and consequently $H_{local}^{GB}=H_a-H_{return}$ (Fig. 4-31a). So that the local field at the grain boundaries is different in the different branches of the hysteresis loop and thus, since the magnetic hysteresis loop is asymmetric, the magnetization represented as a function of the applied field shows a hysteretic behaviour.

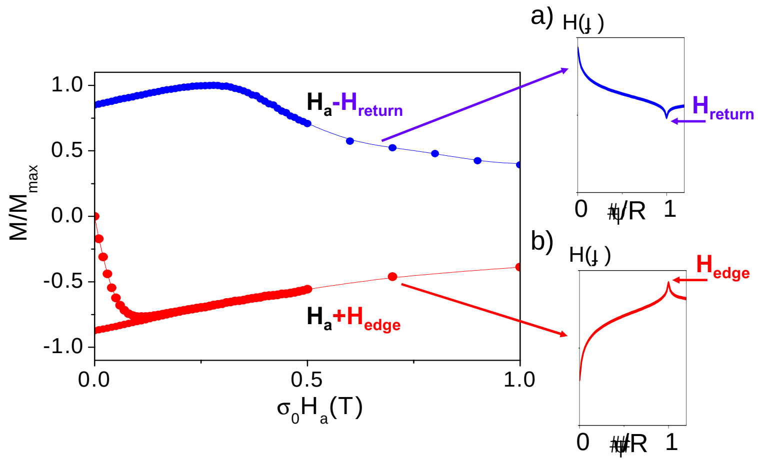

Fig. 4-31. Schematic representation of the local magnetic field at the grain boundaries, determined in the different branches of the hysteresis loop. a) shows the value of the magnetic field at the edge of a grain in the reverse curve of the loop (decreasing the applied field) and b) shows the magnetic field generated in the grain the applied field is increased.

Additionally, for a given applied field $H_a<H^*_G$, the local magnetic field, $H_{local}^{GB}=H_a+H_{edge}$, at the first magnetization curve (curve 1 in Fig. 4-32) is lower than the local magnetic field at the return curve after a complete saturated loop (curve 2 in Fig. 4-32), since H_{edge} increases when the flux trapped inside the grains increases. This difference in the local magnetic field has been observed experimentally in some of the samples analyzed by means of an anomalous crossing between the two curves as exemplified in Fig. 4-32.

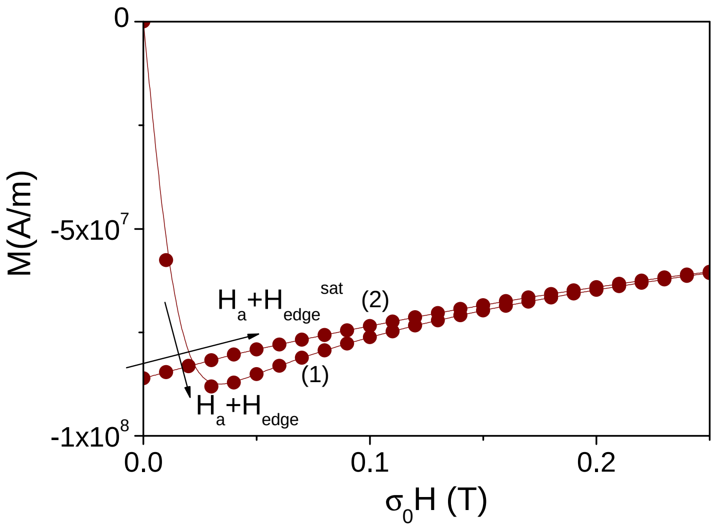

Fig. 4-32. Initial magnetization curve (1) and return curve after a complete saturated loop (2) measured for the sample IBADt0.23$_{Gott}$ at 5K and $\sigma_0 H_m$=0.5T. The anomalous crossing between the two lines is evident.

4.2.4.d FIELD COOLED MEASUREMENTS

All the analysis of the hysteresis loops have been performed by measuring in the ZFC condition, where the sample is cooled down from a temperature above T_c to the working temperature in zero applied magnetic field and then, the magnetic field is applied describing a hysteresis loop for a certain H_m.

Another possibility is to perform the measurement at FC condition. In this case, a magnetic field H_m is applied to the sample at a temperature well above T_C and the sample is cooled down in the presence of this field. The reverse magnetization from H_m to zero can be measured in these conditions.

According to the Bean critical state model, when a sample is cooled down in ZFC condition the maximum applied field necessary to saturate the remanent magnetization is H_m=2H* (Fig. 3-3). The same model determines that in FC condition the remanent magnetization is already saturated for H_m=H* (Fig. 4-33).

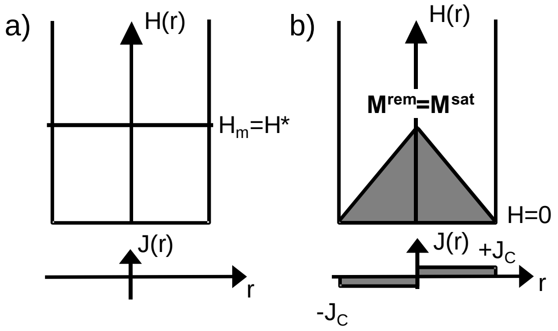

Fig. 4-33. Schematic illustration of Magnetic field in an infinite cylinder based on the Bean critical state model in a FC measurement for H_a=H (a) and in the remanent state, H=0 (b).*

Consequently, if the saturation of the remanent magnetization under ZFC condition occurs at $H_m(M_{rem}^{sat})=2H^*_G$, one expects that under FC conditions these saturation would occur at half of the $H_m(M_{rem}^{sat})$ value.

Several loops have been measured under ZFC and FC conditions for two different samples. Fig. 4-34 and Fig. 4-35 show the obtained values of M^{rem} normalized to M_{rem}^{sat} as a function of $\sigma_0 H_m$ for an IBAD coated conductor, IBADt0.23$_{Gott}$, at 5K and for a RABiTS, RABt1.08$_{ORNL-A}$, at 50K, respectively.

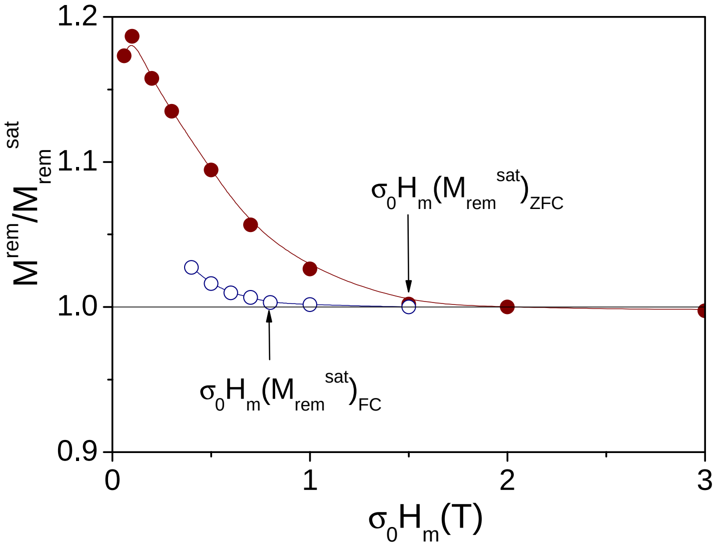

Fig. 4-34. Values of M_{rem} normalized to M_{rem}^{sat} as a function of the maximum applied field, H_m for the sample IBADt0.23$_{Gott}$ at 5K, measured at ZFC (closed symbols) and FC (open symbols).

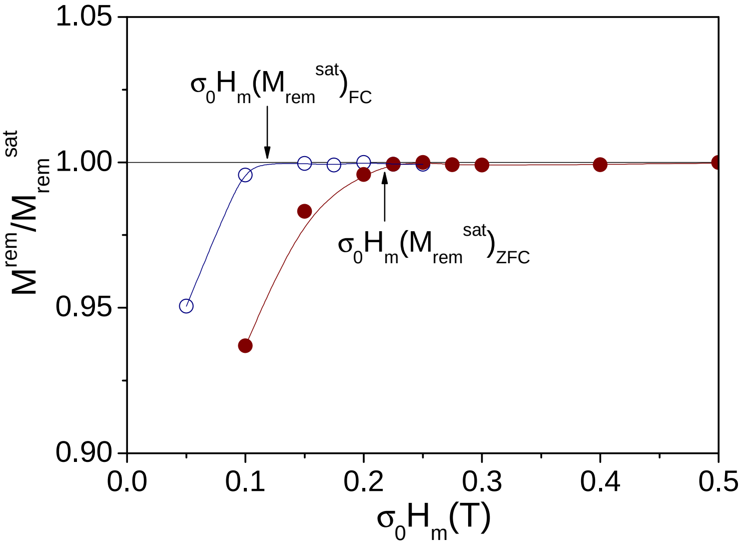

Fig. 4-35. Values of M_{rem} normalized to M_{rem}^{sat} as a function of the maximum applied field, H_m for the sample RABt1.08$_{ORNL-A}$ at 50K, measured at ZFC (closed symbols) and FC (open symbols).

Notice that, although the saturation of M_{rem} occurs in a different way for each sample, i.e. for the sample IBADt0.23$_{Gott}$ decreases until saturation while for the sample RABt1.08$_{ORNL-A}$ increases until saturation (see next section), both confirm the condition, $H_m(M_{rem}^{sat})_{FC}\Im(1/2)H_m(M_{rem}^{sat})_{ZFC}$. For IBADt0.23$_{Gott}$ we have obtained $\sigma_0H_m(M_{rem}^{sat})_{FC}\Im0.8T$ while $\sigma_0H_m(M_{rem}^{sat})_{ZFC}\Im1.5T$ and for RABt1.08$_{ORNL-A}$ $\sigma_0H_m(M_{rem}^{sat})_{FC}\Im0.11T$ and $\sigma_0H_m(M_{rem}^{sat})_{ZFC}\Im0.21T$.

4.2.4.e SIMULATION OF COATED CONDUCTOR HYSTERESIS LOOPS

The anomalous hysteresis loops of coated conductors can be simulated if one calculates the return field that a distribution of grains with a certain critical current density, J_c^G, average grain size, <2a>, and thickness, t, creates at the grain boundaries. We have developed a Labview program, *Hystloops_av*, which, considering this parameters as input variables, calculate the return field associated to the grains at each value of the applied field, and with the obtained values, determines the local magnetic field created at the grain boundaries for any value of the applied magnetic field.

For a typical RABiTS coated conductor the following parameters can be considered for the grains,

$J_c^G(77K)=3.10^{10}A/m^2$, $<2a>=30\sigma m$ and $t=1\sigma m$

In order to calculate $H_{return}(H)$ we have assumed for the grains, the same dependence of $J_c(H)$ than that obtained for a typical non-granular thin film, SCt0.27$_{ORNL-A}$. Then, the return field at each point of the hysteresis loop can be determined considering equation 4-7 ($H_{return}(H)=J_c^G(H)xt$) and 3-7 ($J_c(H)=3M(H)/R$) by means of,

$$H_{return}(H) \mid J_c^G(H)xt \mid \frac{3M^G(H)}{a}xt \qquad 4\text{-}15$$

Although equation 3-7 is strictly valid for saturated $M^G(H)$ curves, we have use it in order to estimate the return field for all the hysteresis loops since we only want to obtain the qualitative shape of the resultant loops for a coated conductor. Fig. 4-36 shows several hysteresis loops calculated for one grain at different applied fields.

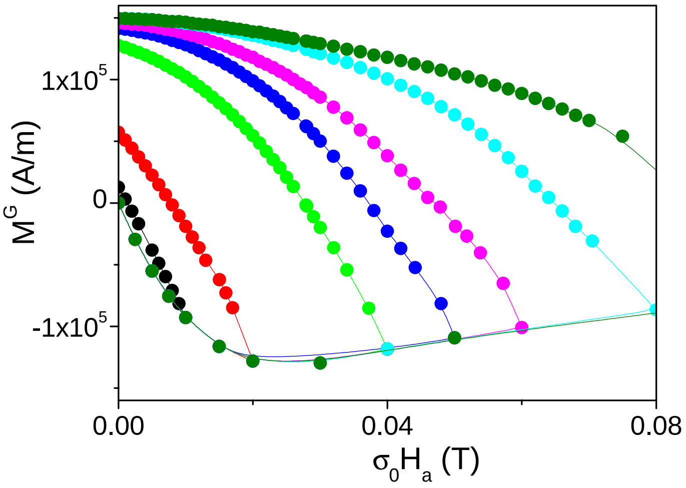

Fig. 4-36. Hysteresis loops calculated at different maximum applied fields, $σ_0H_m$= 0.01T, 0.02T, 0.04T, 0.05T, 0.06T, 0.08T and 0.1T, for a grain with J_c^G=3.10^{10}A/m^2, <2a>=30σm and t=1σm assuming the J_c(H) measured for film SCt0.27$_{ORNL-A}$.

From each $M^G(H_a)$ loop we can determine the local field at the grain boundaries using equation 4-3 (i.e. $H_{loc}^{GB}=H_a-H_{return}$) and 4-15 (Fig. 4-37).

$$H_{loc}^{GB} \mid H_a \; 4 \; H_{return}(H_a) \mid H_a \; 4 \; \frac{3M^G(H_a)}{a} xt \qquad 4\text{-}16$$

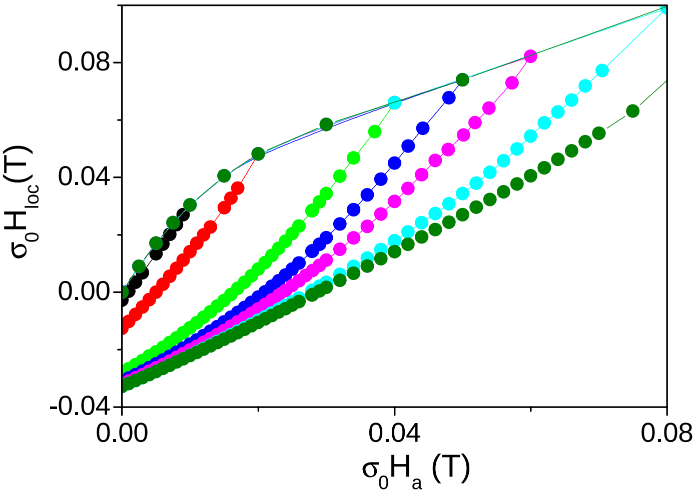

Fig. 4-37. Local magnetic field at the grain boundaries for different maximum applied fields, $σ_0H_m$= 0.01T, 0.02T, 0.04T, 0.05T, 0.06T, 0.08T and 0.1T, calculated from grain magnetic hysteresis loops shown in figure Fig. 4-36.

Once the local magnetic field is determined, one only has to suppose the parameters associated to the GB loops which we have considered as:

J_c^{GB}(77K)=1.10^{10}A/cm^2 =J_c^G/3, R_S=0.25cm

and calculate the magnetic hysteresis loops $M^{GB}(H_{loc}^{GB})$. In order to simplify the calculation we have considered the same magnetic field dependence of J_c^G and J_c^{GB}. Fig. 4-38 shows the GB magnetization curves calculated from this particular coated conductor as a function of the applied magnetic field $M^{GB}(H_a)$. Clearly the anomalous loops with a peak in the reverse branch of the magnetization at $H_a>0$, found for coated conductors, is reproduced. As in the experimental measurements the peak is shifted at higher fields as the maximum applied field increases until it reaches its saturated value, $\sigma_0 H_{peak}^{sat}=0.029T$.

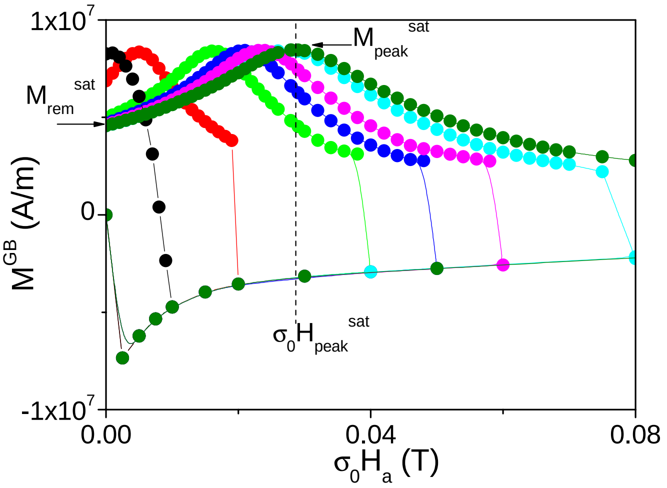

Fig. 4-38. Magnetic hysteresis loops calculated at different maximum applied fields, $\sigma_0 H_m$=0.01T, 0.02T, 0.04T, 0.05T, 0.06T, 0.08T and 0.1T, for a typical RABiTS coated conductor with <2a>=30σm at 77K. The anomalous loops with a peak in the reverse magnetization at $H_a>0$ are reproduced.

The maximum field that saturates the peak position is $\sigma_0 H_m(H_{peak}^{sat})\Im 0.08T$ and from this value $2\sigma_0 H^*_G=\sigma_0 H_m(H_{peak}^{sat})-\sigma_0 H_{peak}^{sat}=0.051T$. On the other hand, the saturation of the remanent magnetization is $\sigma_0 H_m(M_{rem}^{sat})=2\sigma_0 H^*_G \Im 0.07T$ which evidences that the determination of H^*_G by means of $\sigma_0 H_m(H_{peak}^{sat})$ gives us a lower value than the corresponding to the saturation of the return field at $H_a=0$ associated to $J_c^G(H_a=0)$ (see section 4.2.3). Furthermore, the value of the sample full penetration field that we have obtained by means of equation 3-12 ($H^*_S=1.94J_c^{GB}t/2$), $\sigma_0 H^*_S=0.012T$, assures once more that the remanent magnetization saturates due to the saturation of the return field and not owing to the saturation of the GB magnetic moment, $H^*_S<H^*_G$. The value of M_{peak}^{sat} determined from J_c^{GB} and R_S is $M_{peak}^{sat}=8.3MA/m$.

Additionally, we have performed the simulation of an IBAD coated conductor with the same parameters as the ones considered for the RABiTS sample described above

$J_c^G(77K)=3.10^{10}A/m^2$, $J_c^{GB}(77K)=1.10^{10}A/cm^2$, $R_S=0.25cm$ and t=1σm

but now with a smaller grain size, <2a>=2σm, as it has been observed for these type of coated conductors (section 2.2.3).

The obtained hysteresis loops using these parameters are shown in Fig. 4-39. As in the previous experimental loops shown in section 4.2.2, the saturation of the peak position occurs for a lower maximum applied field, $\sigma_0 H_m(M_{rem}{}^{sat})\Im 0.04T$ and at lower position, $\sigma_0 H_{peak}{}^{sat}=0.006T$ for the IBAD sample than for the RABiTS, simply by considering a small grain size. As the parameters associated to the GB critical current have not changed, the same value of $M_{peak}{}^{sat}=8.3MA/m$, have been obtained for the two samples.

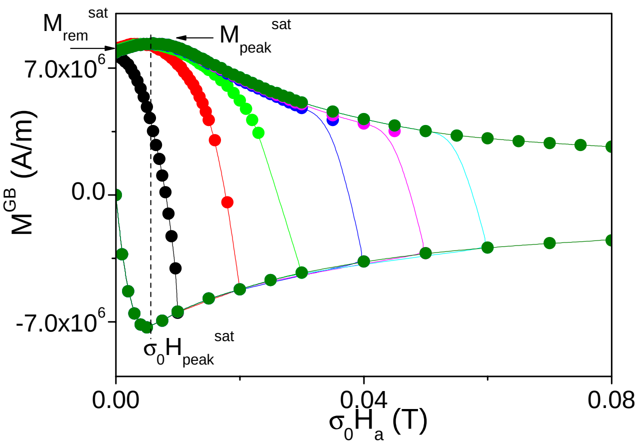

Fig. 4-39. Magnetic hysteresis loops calculated at different maximum applied fields, $\sigma_0 H_m$=0.01T, 0.02T, 0.03T, 0.04T, 0.05T, 0.06T and 0.1T, for a typical IBAD coated conductor with <2a>=2σm, at 77K.

In the calculated hysteresis loops shown above, the saturation of the remanent magnetization occurs due to the saturation of the return field, i.e. when the return field reaches its maximum value. Thus, the remanent magnetization before the saturation decreases when increasing H_m, because the local magnetic field at the grain boundary $H_{loc}=-H_{return}$, increases until it saturates (see Fig. 4-40).

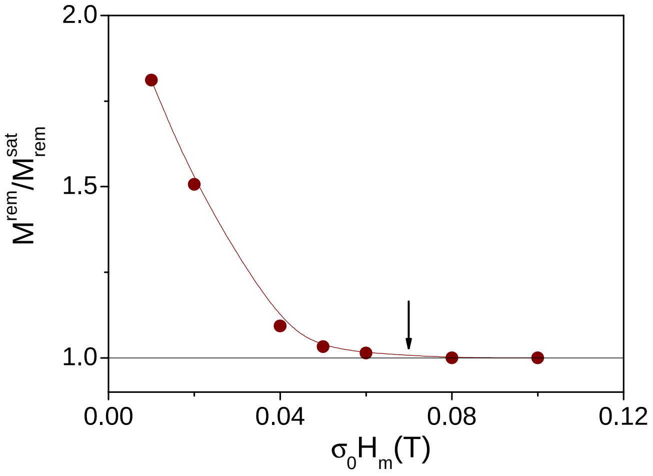

Fig. 4-40. Remanent magnetization, normalized to its saturated value, as a function of the maximum applied field, determined from the calculated hysteresis loops shown in Fig. 4-38.

Fig. 4-41 shows several experimental hysteresis loops measured for sample IBADt1.6b$_{Gott}$ where we can observe that the saturation of M_{rem} occurs as in the calculated loops. The evolution of the remanent magnetization as a function of the maximum applied field for this particular sample has been presented in Fig. 4-29. The same behaviour has been observed previously for the sample IBADt0.23$_{Gott}$ (see Fig. 4-34).

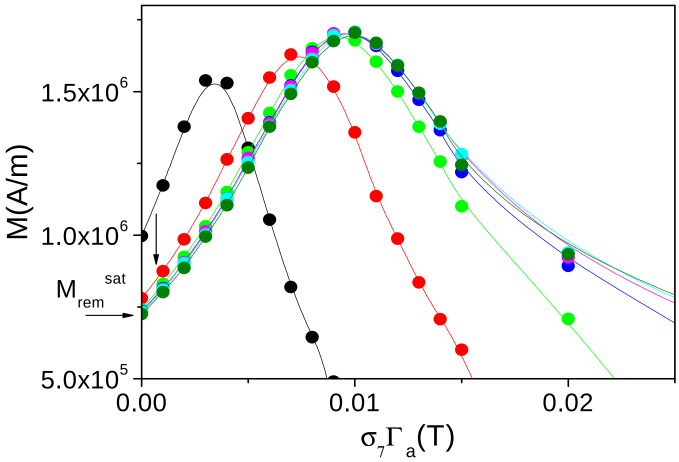

Fig. 4-41. Experimental hysteresis loops measured for the sample IBADt1.6b$_{Gott}$ at 77K for different maximum applied fields, $\sigma_0 H_m$=0.01T, 0.02T, 0.03T, 0.04T, 0.05T, 0.06T and 0.1T.

However, for some of the coated conductors analyzed, the saturation of the remanent magnetization comes out increasing the value of M^{rem} until M_{rem}^{sat} instead of decreasing it. This is the behaviour observed in Fig. 4-22 and Fig. 4-35 for the samples RABt0.34$_{ORNL-B}$, and RABt1.08$_{ORNL-A}$, respectively. We do not have a clear explanation for this effect. However, preliminary simulation with the Labview program *Hystloops_av*, show that this behaviour could be reached by imposing that not all the grains saturate at the same magnetic field. This last condition could be accomplished by assuming that the contribution of the self-magnetic field arising from the percolating GB critical currents (defined in section 4.2.3.a) is not negligible when the sample is still not saturated. It is important to remain that all our analysis and determination of J_c^G and J_c^{GB} has been performed for already saturated samples where it is proved that this self-field is negligible (see section 3.2.3) and we have assured the condition $H^*_G>H^*_S$.

4.2.4.f GRAIN SIZE DISTRIBUTION

The program developed to simulate hysteresis loops of coated conductors allows us, as well, to introduce a certain grain size distribution and analyze the effect of this distribution in the behaviour and the shape of the loops obtained. Fig. 4-43 shows the calculated results of hysteresis loops using the same parameters as in the previous IBAD sample but considering the grain size distribution, f(a), shown in Fig. 4-42.

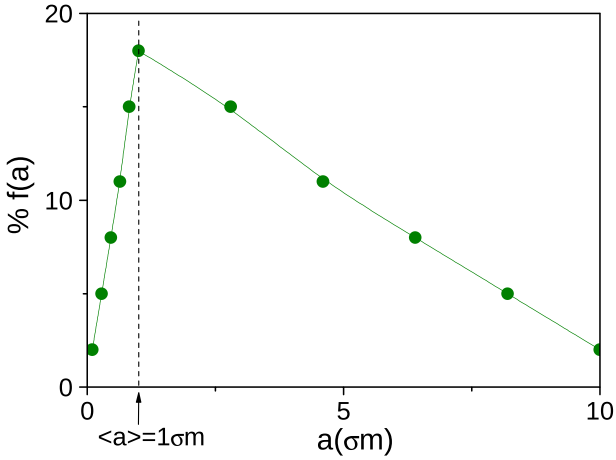

Fig. 4-42. Grain size distribution (in percentage), chosen for the simulation

This particular choice of f(a) considers an average grain size of <a>=1σm with a distribution of grains going from 0.1σm to10σm.

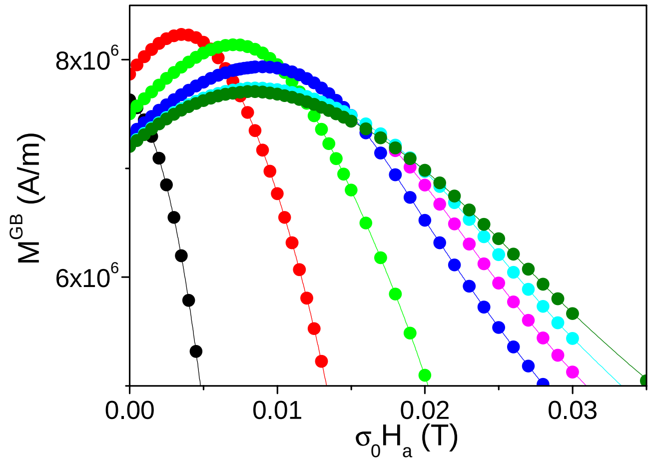

Fig. 4-43. Calculated hysteresis loops determined for an IBAD sample with a grain size distribution n(a) at 77K, for different maximal fields, σ_0H_m=0.01T, 0.02T, 0.03T, 0.04T, 0.05T, 0.06T and 0.1T.

Notice that, by considering a certain grain size distribution, the magnetization peak does not stay constant when the maximum applied field in the loops is higher than $2H^*_S$ ($2\sigma_0H^*_S$=0.024T, for this particular sample). This opposes to the case where we have considered a single grain size (see Fig. 4-38). In fact, by considering a grain size distribution we observe that the peak height decreases and broadens until we saturate all the grains. These effects have been observed in some of the samples analyzed as it is exemplified in Fig. 4-44 for the IBADt0.23$_{Gott}$ sample. Clearly there is an overall agreement in the behaviour of the hysteresis loops for the experimental data (Fig. 4-44) and for the calculated data (Fig. 4-43). However, the hysteresis loops measured for most of the samples analyzed do not show this behaviour which indicates that in general, the coated conductors that we have studied do not present an important grain size distribution.

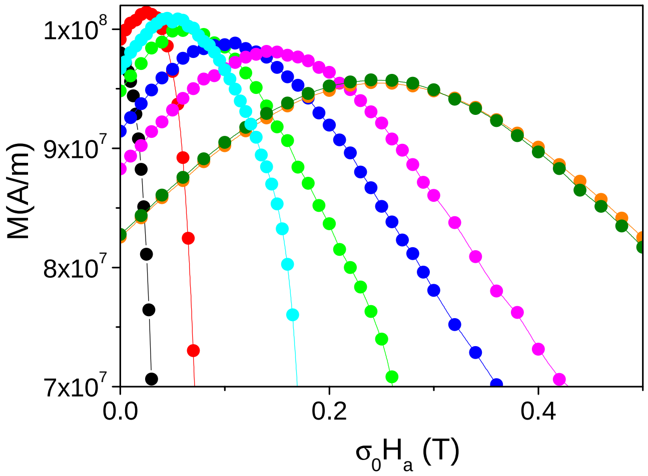

Fig. 4-44. Experimental hysteresis loops measured for the sample IBADt0.23$_{Gott}$ at 5K for different maximal fields, H_m.

4.2.4.g MAGNETIZATION HYSTERESIS CURVE AS A FUNCTION OF THE LOCAL FIELD

We have seen that it is possible to generate the anomalous loops found for coated conductors if the GB magnetization is represented as a function the applied field instead of the local field at the grain boundaries. The inverse process is also possible so that, one can obtain a symmetrical hysteresis loop from an anomalous measured one if the magnetization is represented as a function of the local magnetic field. This further confirms that the main contribution to the anomalous hysteresis loops is the return field from the grains.

In general, from the saturated value of H_{peak}, H_{peak}^{sat}, and assuming a certain dependence of $J_c^G(H)$, we would be able to determine the local magnetic field at each point of the hysteresis loop, in the same way as presented above. Then, representing the magnetization as a function of the local magnetic field we would obtain a symmetrical hysteresis loop like the one expected for a non-granular thin film (see section 4.1.1). However, in general, this process is very difficult since we don't know a prori the exact dependence of $J_c^G(H)$.

The saturated reverse branch of the magnetization measured for the sample IBADt1.6b$_{Gott}$ at 50K is shown in Fig. 4-45 (closed symbols). It is clearly seen a peak at σ_0H_a=0.055T when the magnetization is represented as a function of the applied magnetic field. A symmetrical loop with a peak of magnetization at σ_0H_{loc}=0 has been obtained when the magnetization is represented as a function of the local field calculated considering the dependence, $J_c^G(H)=J_{c0}H^{40.7}$.

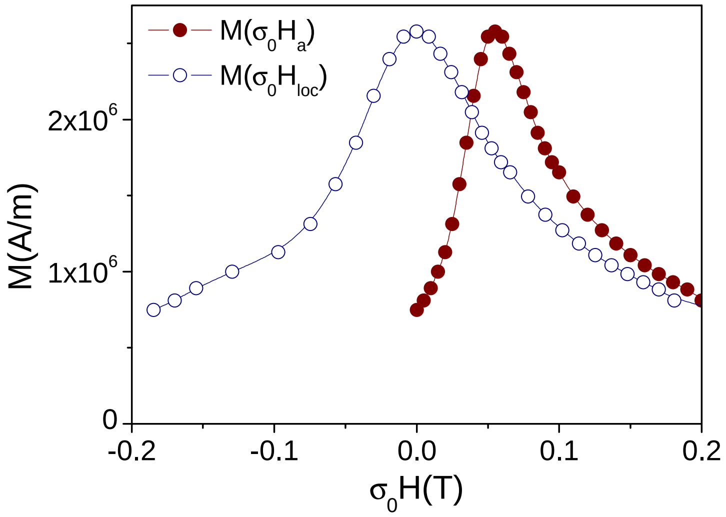

Fig. 4-45. Measured magnetization for the sample IBADt1.6b$_{Gott}$ at 50K as a function of the applied magnetic field, $\sigma_0 H_a$ (closed symbols) and as a function of the calculated local magnetic field at the grain boundaries, $\sigma_0 H_{loc}$ (open symbols).

4.2.4.h COMPLEMENTARY EXPERIMENTAL TECHNIQUES CONFIRMING THIS EFFECT

MAGNETO OPTICAL MEASUREMENTS

The effect of the return field, created for the grains at the grain boundaries, in YBCO coated conductors, has also been observed by magneto optical imaging. These measurements were performed during my stay in the “Zentrum für FunktionWekstoffe” of Göttingen (Germany) and consisted on the following. We measured the magnetic flux distribution in an IBAD coated conductor, IBADt1.6a$_{Gott}$, when, after field cooling the sample at σ_0H_a=260mT, we reduce the magnetic field (following the return curve of the hysteresis loop) until a certain value. Fig. 4-46 and Fig. 4-47 show the magnetic flux distribution measured for the sample IBADt1.6a$_{Gott}$ at 9K, when the applied magnetic field has been decreased until σ_0H_a=0 (remanent state), and σ_0H_a=39.6mT, respectively. In a non-granular film, due to the field dependence of J_c, one would obtain a higher trapped field at σ_0H_a=0 than at σ_0H_a=39.6mT but we observe that this is not what we get for a coated conductor. At σ_0H_a=0mT the maximum trapped field in the centre of the sample is, $B_z \Im 0.06$T while at σ_0H_a=39.6mT we have obtained a higher value, $B_z \Im 0.1$T. This behaviour can be understood considering that the local magnetic field at the grain boundaries have the contribution of the return field coming from the grains, i.e. $\sigma_0H_{loc}^{GB}=\sigma_0H_a-\sigma_0H_{return}$. Then, as we have observed in the magnetic hysteresis loops, the local magnetic field is higher at σ_0H_a=0mT than at σ_0H_a=39.6mT and consequently the trapped field is higher in the last situation.

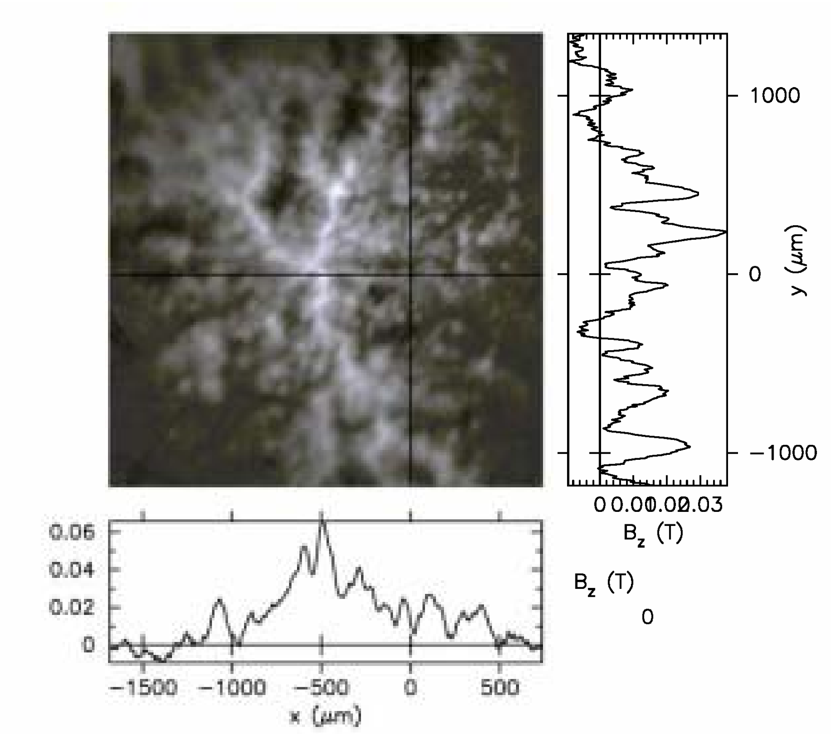

Fig. 4-46. Flux distribution measured for the coated conductor IBADt1.6a$_{Gott}$ at 9K, after FC the sample at σ_0H_a=260mT and reduce the magnetic field until σ_0H_a=0T. Magnetic flux profiles are given at the positions of the lines.

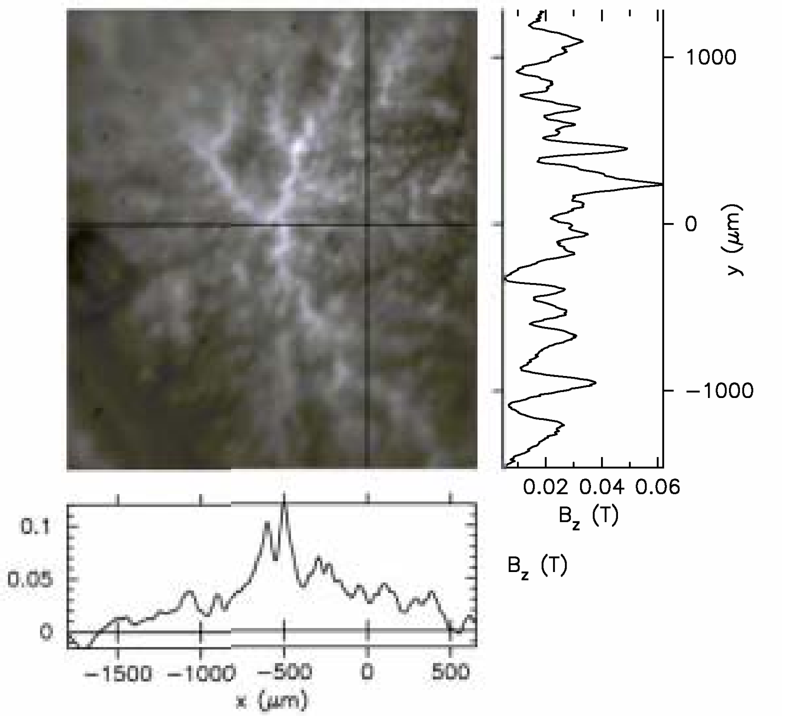

Fig. 4-47. Flux distribution measured for the coated conductor IBADt1.6a$_{Gott}$ at 9K, after FC the sample at σ_0H_a=260mT and reduce the magnetic field until σ_0H_a=39.6mT. Magnetic flux profiles are given at the positions of the lines.

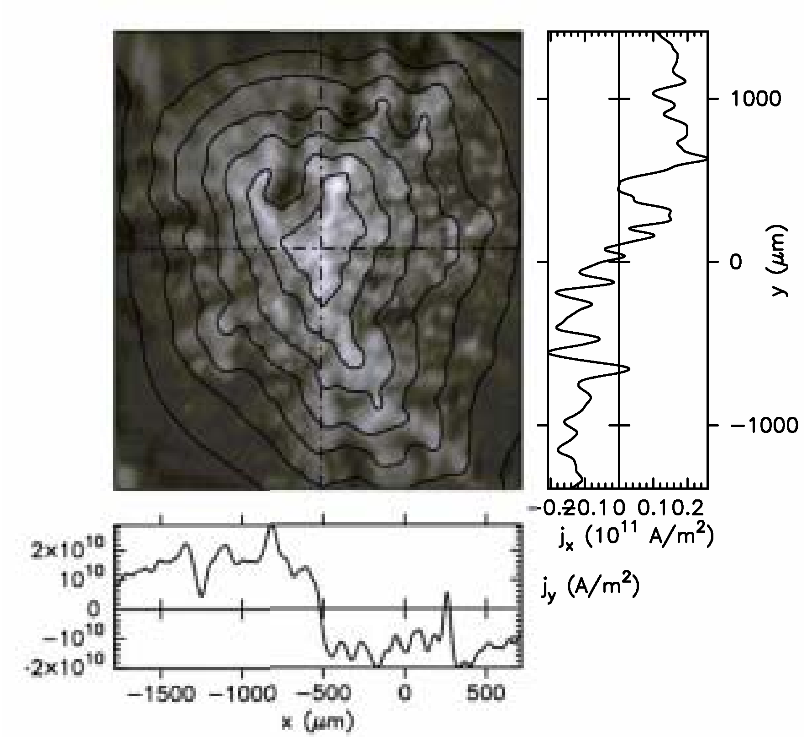

Fig. 4-48. Current density distribution determined for the coated conductor IBADt1.6a$_{Gott}$ at 9K, after FC the sample at σ_0H_a=260mT and reduce the magnetic field until σ_0H_a=0mT. Current density profiles are given at the positions of the broken lines.

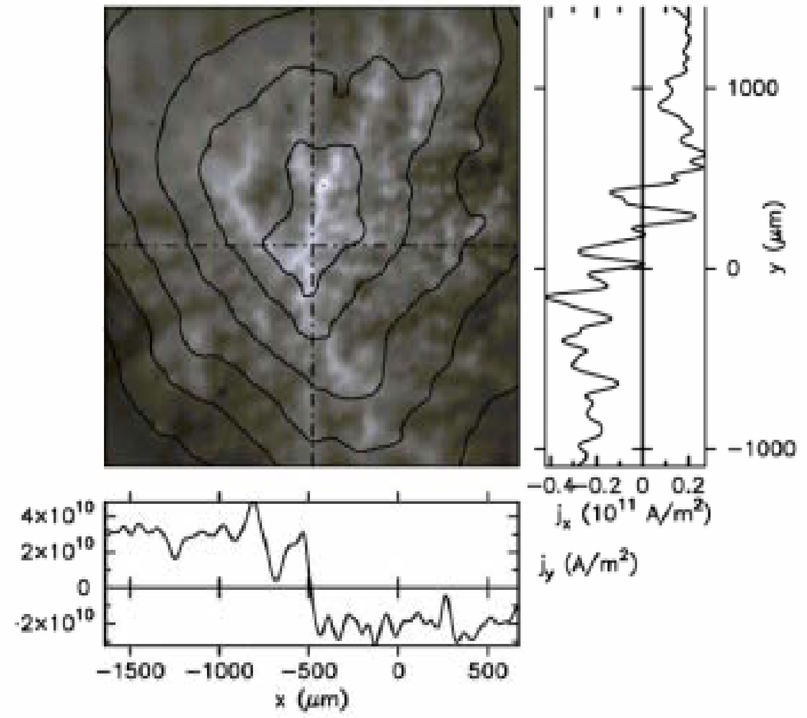

Fig. 4-49. Current density distribution determined for the coated conductor IBADt1.6a$_{Gott}$ at 9K, after FC the sample at σ_0H_a=260mT and reduce the magnetic field until σ_0H_a=39.6mT. Current density profiles are given at the positions of the broken lines.

From Fig. 4-46 and Fig. 4-47, we have determined the critical current density by means of the Biot Savart's law (which gives the integral relation between the current density and the magnetic field) using the formalism described in ref [56]. Fig. 4-48 and Fig. 4-49 shows the critical current density distribution superimposed at the MO images and the current density profiles determined at the position of the broken lines.

From the MO images we observe that, although a general critical state is formed in the whole sample, a large inhomogeneity in the GB network is detected (according to that observed in the ac-susceptibility measurements shown in section 6.2.2). Notice that in general, for an IBAD coated conductor, since the grain size is smaller that the MO resolution, we would obtain a flux profile similar to that observed for a non-granular thin film (see section 6.2.1). Due to the GB inhomogeneities the critical current profiles obtained are very irregular and the determination of an average J_c^{GB} value is difficult, nevertheless we clearly see that the average value of critical current density obtained in the remanent state, J_c^{GB}ℑ$1.5.10^{10}$A/m^2, (Fig. 4-48) is smaller than the one obtained for $\sigma_0 H_a$=39.6mT, J_c^{GB}ℑ$2.5.10^{10}$A/m^2, (Fig. 4-49). In order to determine a qualitative curve of the evolution of J_c^{GB} with the magnetic field, we have taken images of the sample for different applied magnetic fields in the return branch of the hysteresis loop and we have determined the correspondent average J_c^{GB} in each case. Fig. 4-50 shows the values of the critical current density as a function of the applied magnetic field, determined from the MO images (open symbols) and from the saturated reverse branch of the magnetic hysteresis loop (closed symbols). Notice that although there is a shift between the two curves, qualitatively, we have obtained the same tendency. For the curve obtained from MO measurements it was not possible to obtain more points at large fields since the calibration of the magnetic flux for applied magnetic fields larger than 0,1T was not feasible.

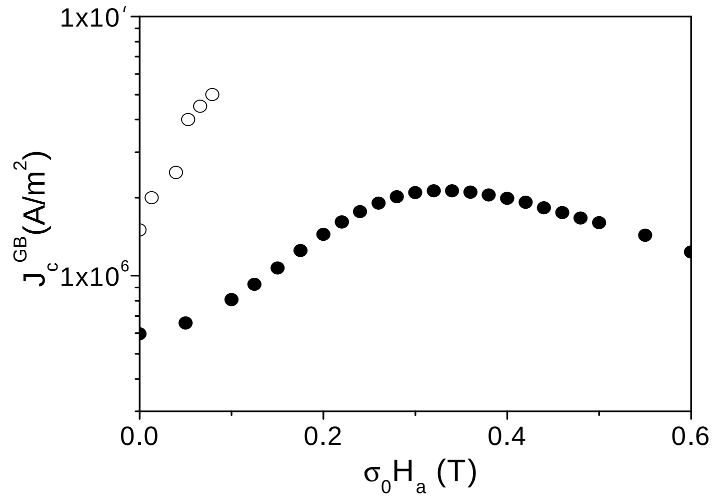

Fig. 4-50. GB critical current density as a function of the applied magnetic field, determined from MO measurements (open symbols) and from the saturate reverse branch of the hysteresis loop (closed symbols).

TRANSPORT MEASUREMENTS

We have identified the hysteretic behaviour observed in the GB critical current density of a coated conductor (see section 4.2.4.c) by means of transport measurements. Fig. 4-51 shows field dependence of the transport critical current density measured for the sample IBADt1.2$_{Gott}$ at 25K increasing the applied field until $\sigma_0 H_m$=9T and then decreasing the field until zero. These measurements have been performed for members of the group in the ICMAB. Notice that we clearly obtain a hysterical curve $J_c(H_a)$ with a maximum in the decreasing branch at $\sigma_0 H_{peak}$=0.6T, which can be explain in the same way as we did for the magnetization hysteresis loops (see section 4.2.2).

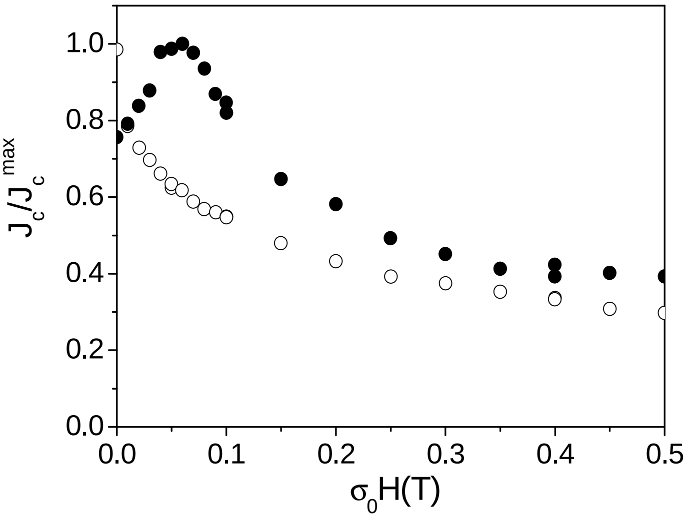

Fig. 4-51. Magnetic field dependence the transport critical current density , normalized to its maximum value, measured for the sample IBADt1.2$_{Gott}$ at 25K, by increasing (open symbols) and decreasing (closed symbols) the magnetic field untill $\sigma_0 H_m$=9T, where the hysteretic behavior of J_c is revealed.

4.3 CONCLUSIONS

In this chapter we have analysed the magnetic behaviour of YBCO non-granular thin films and coated conductors by means of dc-magnetization measurements of hysteresis loops. The contribution of the metallic substrate in the measurements for coated conductors has been studied and separated from the signal coming from the superconducting layer. The obtained hysteresis loops have been widely analysed and compared with the ones measured for non-granular YBCO thin films. We have observed that for YBCO thin films a peak in the magnetization appears at zero applied magnetic field as it is expected due to their large demagnetizing effects. However, for the coated conductors we have found that the magnetization peaks at a positive applied field in the reverse magnetization curve. This shift in the position of the magnetization peak have been ascribed to granularity effects and explained by means of the magnetic flux trapped inside the grains which return through the grain boundaries.

Based on the peculiar features observed in the hysteresis loops of coated conductors and measuring several minor loops at different maximum applied fields, we have developed a formalism by which the grain and grain boundary critical current densities of coated conductors, J_c^G and J_c^{GB}, can be determined in the framework of the critical state model. The simplicity of the method paves the way to a full investigation of the relationship existing between these two critical current densities.

In order to verify the formalism developed and check its consistency we have validated its assumptions and simulated some experimental results. The main assumption of the model, a negative return field at the low angle grain boundaries coming from the grains, has been measured in a bicrystal by means of magneto optical imaging. Additionally, from the anomalous hysteresis loops measured in coated conductors we have been able to determine the hysteretic behaviour of J_c^{GB} with the applied magnetic field, which has been confirmed by transport measurements of coated conductors.

Field cooled measurements of the return curve for several hysteresis loops proved that in that case the saturation of the grains occurs faster than in zero field cooled measurements as it is expected.

Additionally, we have developed different Labview programs which reproduce the measured hysteresis loops for coated conductors by calculating the local magnetic field at the grain boundary. With these programs we can introduce a certain grain size distribution which modifies the hysteresis loops as has also been experimentally observed. Finally, we have also determined the local magnetic field as a function of the applied field for measured hysteresis loops of an IBAD coated conductor and we have obtained a symmetrical loop with the peak appearing at zero field when representing the magnetization as a function of the local magnetic field.